



Faculteit Wetenschappen

Departement Fysica

In Situ TEM Study on the Manipulation of
Ferroelectrics

In situ TEM-studie over de manipulatie van ferro-elektriciteit

Proefschrift voorgelegd tot het behalen van de graad van Doctor in de
Wetenschappen aan de Universiteit Antwerpen, te verdedigen door

Kai Du

Promotor

Prof. Dr. Gustaaf Van Tendeloo

Prof. Dr. He Tian

Antwerp

Prof. Dr. Sara Bals

2021

Doctoral Committee

Chairman

Promoter

Prof. Dr. Gustaaf Van Tendeloo, University of Antwerp, Belgium

Prof. Dr. He Tian, Zhejiang University, China

Prof. Dr. Sara Bals, University of Antwerp, Belgium

Contact information

Kai Du

University of Antwerp – Department of Physics

EMAT – Electron Microscopy for Materials Science

Groenenborgerlaan 171 B-2020 Antwerp

Belgium

&

Center of Electron Microscopy

State Key Laboratory of Silicon Materials, and School of Materials Science

Zhejiang University

310027 Hangzhou

China

kaidu@zju.edu.cn

Abstract

The strong correlated oxide systems attract a lot of attentions of scientists recently, the coexistence and interplay between various degrees of freedom, such as charge, spin and orbital, has been demonstrated to induce some fancy physical properties and phenomenon, including metal-insulator transition, high temperature superconductivity, colossal magnetoresistance. As a part of the strong correlated oxide systems, the ferroelectrics is abundant in both physical properties and application. First, if the electric dipole continuously rotating around a stable core then a topological structure is produced. If people could manipulate the topological structure and simultaneously observe the structure evolution, with external field applied on the topological structure, then it is very likely for such kind of ferroelectrics to be the next generation of storage, for it is reported to need low power input and produce high density of storage. In the other hand, in solids, charge polarity can one-to-one correspond to spin polarity phenomenologically, such as ferroelectricity and ferromagnetism, antiferroelectricity and antiferromagnetism, but ferrielectricity and ferrimagnetism kept telling a disparate story in microscopic level. The claimed “ferrielectrics” in existing research is equivalent to ferroelectric ones, thus the findings of such a real irreducible solids would complete the last piece of the ferroelectrics family.

While solving the above two questions remain challengeable: the size of topological structure is small (typically below 10 nm), general characterization methods are insufficient for such high demand on space resolution, not to mention manipulating and observing its dynamic behavior at an atomic level. Here, employing the spherical aberration corrected electron microscope, we applied external field (heating and bias) on ferroelectrics. Combined with high-end characterization methods including the high-angle annular dark field (HAADF-STEM) image, Electron Energy Loss Spectroscopy (EELS) and integrated differential phase contrast

(iDPC), the dynamic evolution of ferroelectrics are observed and analyzed.

The main findings of this paper could be concluded as listed here:

(1) $\text{PbTiO}_3(001)//\text{SrTiO}_3(001)$ is grown on DyScO_3 and SrRuO_3 by pulsed laser deposition, the atomical EDS mapping results reveal that the interface between PTO and STO is atomically sharp. Increasing the thickness of PTO from 1 μc to 21 μc , the topological structure within PTO layer would transform from a/c domain to wave, vortex and finally flux closure domain. The geometric phase analysis results (GPA) reveal that above topological structures are corresponding to various strain.

(2) Combined with in-situ biasing holder, the electric bias was applied on polar vortex, and it evolved from vortex (0 V) to polar wave (2 V) and finally polar down (5 V). EELS analysis was performed and we find that negative charge is gathered at vortex core, which turns the Ti^{4+} to Ti^{3+} there. The oxygen vacancy at negative polarization surface and the negative charge at the positive polarization surface realized the polarization screening of polar down domain.

(3) Through the atomic inspection and analysis on lattice structure of BaFe_2Se_3 , the near ladders within single unit are found to be different in degree of tetramerization, thus leading to a residual polarization along the a -axis. The further in-situ heating and biasing experiment was conducted on BaFe_2Se_3 , and the strong and weak ladders are proved to be independent for their behavior under external field. This findings distinguishes ferrielectrics from ferroelectrics in solids.

Key words: perovskite ferroelectric oxides, topological ferroelectrics, irreducible ferrielectric

Abstract

Sterk gecorreleerde oxidesystemen trekken de laatste tijd veel aandacht van wetenschappers, het is aangetoond dat het samenspel tussen verschillende vrijheidsgraden, zoals lading, spin en orbitaal, een aantal mooie fysische eigenschappen en fenomenen induceert, waaronder de overgang van metaal naar isolator, supergeleiding op hoge temperatuur al kolossale magnetoweerstand. Als onderdeel van de sterk gecorreleerde oxidesystemen is de ferro-elektrische stof overvloedig aanwezig in zowel fysische eigenschappen als toepassing. Ten eerste, als de elektrische dipool continu rond een stabiele kern roteert, wordt een topologische structuur geproduceerd. Als mensen de topologische structuur zouden kunnen manipuleren en tegelijkertijd de evolutie van de structuur zouden kunnen observeren, met extern veld toegepast op de topologische structuur, dan is het zeer waarschijnlijk dat dit soort ferro-elektrische systemen de volgende generatie van opslag zullen zijn, want naar verluidt is er een laag stroomverbruik nodig produceren een hoge opslagdichtheid. Aan de andere kant, in vaste stoffen, kan ladingspolariteit één-op-één overeenkomen met fenomenologische spinpolariteit, zoals ferro-elektrische en ferromagnetisme, antiferro-elektrische en antiferromagnetisme, maar ferri-elektrische en ferrimagnetisme bleven een ongelijk verhaal vertellen op microscopisch niveau. De geclaimde "ferro-elektrische stoffen" in bestaand onderzoek zijn gelijk aan ferro-elektrische, dus de bevindingen van zo'n echte onherleidbare vaste stof zouden het laatste stukje van de puzzel van de ferro-elektrische familie voltooien.

Hoewel het oplossen van de bovenstaande twee vragen een uitdaging blijft: de grootte van de topologische structuur is klein (meestal minder dan 10 nm), algemene karakterisatiemethoden zijn onvoldoende voor zo'n hoge vraag naar ruimteresolutie, om nog maar te zwijgen van het manipuleren en observeren van het dynamische gedrag op atomair niveau. Hier, gebruikmakend van de sferische aberratie gecorrigeerde elektronenmicroscopie, hebben we externe velden (verwarming en bias) toegepast op ferro-elektrische systemen. Gecombineerd met hoogwaardige karakterisatiemethoden, waaronder het ringvormige

donkerveldbeeld (HAADF-STEM) met hoge hoek, elektronenergieverliesspectroscopie (EELS) en geïntegreerd differentieel fasecontrast (iDPC), wordt de dynamische evolutie van ferro-elektrische systemen geobserveerd en geanalyseerd.

De belangrijkste bevindingen van dit artikel kunnen worden geconcludeerd zoals hier vermeld:

(1) $\text{PbTiO}_{3(001)} // \text{SrTiO}_{3(001)}$ wordt gekweekt op DyScO_3 en SrRuO_3 door middel van pulsed laser deposition, de atomische EDS mapping resultaten laten zien dat het grensvlak tussen PTO en STO aomisch scherp is. Door de dikte van de PTO te vergroten van 1 uc naar 21 uc, zou de topologische structuur met de PTO-laag transformeren van a/c-domein naar golf-, vortex- en uiteindelijk fluxafsluitingsdomein. De resultaten van de geometrische fase-analyse (GPA) laten zien dat bovenstaande topologische structuren overeenkomen met verschillende rek.

(2) Gecombineerd met in-situ voorspanhouder, werd de elektrische voorspanning toegepast op polaire vortex, en deze evolueerde van vortex (0 V) naar polaire golf (2 V) en uiteindelijk polair naar beneden (5 V). EELS-analyse werd uitgevoerd en we vinden dat negatieve lading wordt verzameld bij de vortexkern, die de Ti^{4+} daar verandert in Ti^{3+} . De zuurstofvacature op het negatieve polarisatieoppervlak en de negatieve lading op het positieve polarisatieoppervlak realiseerden de polarisatiescreening van het polaire benedenliggende domein.

(3) Door de atomaire inspectie en analyse van de roosterstructuur van BaFe_2Se_3 , blijkt dat de nabije ladders binnen een enkele eenheid verschillend zijn in mate van tetramerisatie, wat leidt tot een resterende polarisatie langs de a-as. Het verdere in-situ verwarming- en voorspanningsexperiment werd uitgevoerd op BaFe_2Se_3 en het is bewezen dat de sterke en zwakke ladders onafhankelijk zijn voor hun gedrag onder extern veld. Deze bevindingen onderscheiden ferri-elektrische verbindingen van ferro-elektrische verbindingen in vaste stoffen.

Sleutelwoorden: perovskiet ferro-elektrische oxiden, topologische ferro-elektrische, onherleidbare ferro-elektrische

CONTENTS

Abstract.....	I
Abstract.....	III
CONTENTS.....	V
Chapter 1 An introduction to the ferroelectrics	1
1.1 A brief introduction to the properties and applications of ferroelectrics	1
1.2 Fundamental structure and properties of ferroelectrics	2
1.2.1 The crystal structure and basic properties of perovskite oxide.....	2
1.2.2 Screening mechanism of polarization in perovskite ferroelectric materials.....	4
1.2.3 Ferroelectric hysteresis curve and Curie temperature.....	5
1.3 Topological structure in ferroelectrics	6
1.3.1 The structure and characterization of Ferroelectric topological materials	6
1.3.2 The manipulation of ferroelectric topological structures.....	10
1.4 A brief introduction to irreducible ferroelectrics	13
1.5 Content and Research ideas of this thesis	14
Chapter 2 Experimental methodologies.....	17
2.1 Transmission electron microscopy.....	17
2.1.1 Basic imaging principles of transmission electron microscope	17
2.1.2 The imaging mode and structure of transmission electron microscope..	19
2.1.3 Causes and elimination of aberrations in electron microscopy	23
2.2 Electron energy loss spectrum (EELS)	26
2.2.1 The principle of electron energy loss spectrum	26
2.2.2 Compare EELS with traditional element analysis techniques	27
Chapter 3 The manipulation of topological structure on ferroelectrics	30

3.1 Introduction.....	30
3.2 Technique detail	31
3.2.1 Sample preparation	31
3.2.2 Parameter chosen for electron microscopy	32
3.2.3 Phase-field simulations	33
3.2.4 Determination of the atomic displacements.....	34
3.3 The characterization of PTO/STO at initial state.....	35
3.4 The in-situ study on structural evolution of PTO/STO under external bias	40
3.5 Exploring the electronic structure of topological configurations	43
3.6 Conclusions.....	49
Chapter 4 The exploration on irreducible ferrielectric materials	51
4.1 Introduction.....	51
4.2 Technique detail	53
4.2.1 Sample preparation	53
4.2.2 Macroscopic properties measurements	54
4.2.3 In-situ study and specimen transferred to chips.....	54
4.2.4 DFT calculation	56
4.3 The Structural characterization and research of charge distribution on BaFe ₂ Se ₃	56
4.4 The in-situ study on structural evolution of BaFe ₂ Se ₃ with rising temperature	62
4.5 The in-situ study on structural evolution of BaFe ₂ Se ₃ under external bias.....	67
4.6 Conclusions.....	69
Summary.....	71
Samenvatting	75
References.....	79
List of publications.....	89
Acknowledgements	91

Chapter 1 An introduction to the ferroelectrics

1.1 A brief introduction to the properties and applications of ferroelectrics

Strongly correlated electronic systems have been a hot topic in the field of condensed matter physics in recent years. The mutual coupling and interaction among many degrees of freedom, such as charge, spin, orbit, have produced a series of novel physical phenomena, such as the giant magnetoresistance effect^[1], metal-insulator transition^[2], high temperature superconductivity^[3], and multiferroics^[4-7]. These physical properties have been confirmed by some studies in recent years that they have important practical application value in many fields such as solid oxide fuel cells, spintronic devices, light-emitting diodes, and solar perovskite cells^[8-13]. As an important part of the system, ferroelectric materials have attracted widespread attention due to their rich physical properties and broad application prospects, especially in the field of storage devices. The Si-based elements used in today's mainstream storage devices are facing the limitation of Moore's Law. If ferroelectric devices can replace them, they will become the basis of next-generation memory devices^[14-18]. Among the many branches of strongly correlated electronic systems, perovskite materials have received the most widespread attention due to their simple structure, rich properties, and diverse preparation methods^[19-22]. On the other hand, with the development of modern semiconductor technology, various thin-film growth technologies have also been developed rapidly. These methods have allowed the preparation of samples with flat atomic-level interfaces. Based on these factors, many novel phenomena were discovered in perovskite oxide interfaces^[23-31]. At the same time, various characterization methods with atomic resolution have also ushered in a rapid development period. Spherical aberration correction electron microscope, electron energy loss spectroscopy, and high-resolution energy spectroscopy provide various tools for studying the structure of perovskite materials^[10, 32-37].

For the application of ferroelectric materials in the memory field, the modulated ferroelectric polarization is generally used. Under the conditions of an external electric field or stress field, the charge can be released or absorbed during the ferroelectric flipping

process. The gains and losses of this charge are read equivalent to the binary 0 and 1 in the computer field, so it can be used for computer storage^[4, 38]. The current commercial ferroelectric memory has the advantages of fast writing speed and low energy consumption; but due to the problem of depolarization field in ferroelectric polarization, there is possibility of data storage failure or loss^[39]. The concept of ferroelectric field effect transistors proposed in recent years is expected to solve these problems^[40, 41]. In addition, the ferroelectric tunnel junction also provides new ideas. The ferroelectric tunnel junction is generally composed of two layers of metal or semiconductor sandwiched by a very thin ferroelectric film. The ferroelectric tunnel junction has a large switching ratio (10^4) and a higher number of cycles (>10000)^[42], and a higher storage density (10 T bits per square inch)^[43, 44].

In summary, with its rich physical properties, ferroelectric materials have broad application prospects in the field of microelectronic devices, especially for memory devices. The precise control of the microstructure of ferroelectric materials is of great significance for the research and commercial use of next-generation memory devices.

1.2 Fundamental structure and properties of ferroelectrics

1.2.1 The crystal structure and basic properties of perovskite oxide

The ferroelectricity was first discovered by J. Valasek et al.^[45], and then various ferroelectric materials have sprung up. In ferroelectrics, the displacement of atomic configuration of the unit cell makes the centers of positive and negative charges do not coincide to each other and thus an electric dipole moment will form, which results in spontaneous polarization. Spontaneous polarization can have multiple possible orientations, and under the action of an external field (especially an external electric field), the direction and extent of the ferroelectric shift may change. From a crystallographic point of view, ferroelectric materials can only occur in 10 polar point groups. Among them, perovskite materials have become one of the focuses of the research of ferroelectric materials because of their simple structure and rich candidate elements.

Perovskite materials originally specifically referred to some compounds in perovskite ore, such as CaTiO_3 . The basic structure is usually represented by ABO_3 , as shown in the diagram. The most common ABO_3 perovskite structures are SrTiO_3 (STO), PbTiO_3 (PTO), BiFeO_3 (BFO) and so on. The A site is generally alkaline earth elements or rare earth elements (such as Ba, Pb, Bi) with a large ionic radius, and the B site is generally a transition metal element with a small ionic radius (such as Fe, Zr, Ti). Both A and B are cations, and the oxygen ion as an anion occupies the face center position, forming an oxygen octahedral structure, and forms a BO_6 structure with the B ion at the core.

The structure undergoes a phase change at high temperatures and becomes a cubic crystal system. At room temperature, the material changes from a cubic structure with high symmetry to a low symmetry structure. This temperature point is called the Curie temperature (T_C). The result of the change may be a tetragonal system (the structural distortion is along a uniaxial direction), an orthorhombic system (the structural distortion is along two axes at this time), or a trigonal crystal system (the structural distortion occurs along the $[111]$ direction).

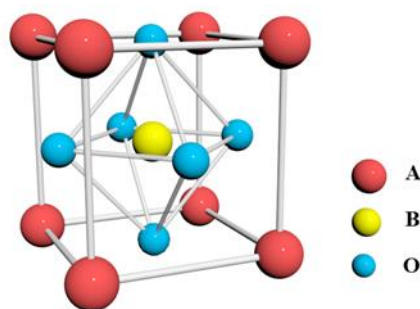


Figure 1.1 Schematic illustration of the crystal structure of ABO_3 perovskite.

Like other ferroelectric materials, the positive and negative charge centers of the perovskite structure do not coincide, resulting in iron polarization. The spontaneous polarization will cause bound charges to be generated on the surface of the material, and bound charges will be shielded by a variety of mechanisms, which ultimately makes the polarization stable. If an external electric field is applied along the perovskite crystal, the spontaneous polarization of the material will change, which is the theoretical basis of ferroelectric memory.

Similarly, if an external stress field is applied to a ferroelectric crystal, the polarization inside the crystal will increase or disappear, which is the so-called piezoelectric effect or inverse piezoelectric effect; and when the crystal itself has ferroelectric polarization, When the temperature changes, the polarization intensity changes accordingly, and voltage or current is generated on the positive and negative polarized surfaces of the material, which is called the pyroelectric effect. Because ferroelectric materials have many of the above-mentioned excellent physical properties, they are widely used in optoelectronic devices, such as MEMS devices, sensors, non-volatile memories, etc.

1.2.2 Screening mechanism of polarization in perovskite ferroelectric materials

Due to the spontaneous polarization inside the crystal, the perovskite ferroelectric oxide therefore exhibits ferroelectricity macroscopically. This ferroelectricity is discontinuous at the interface, and bound charges are generated on the surface due to Maxwell's electrostatic energy. Among them, the positively polarized surface is positively bound charge, and the negatively polarized surface is negatively bound charge. An electric field from positive charge to negative charge is generated between these two kinds of charges, which is called a depolarization field. The direction of ferroelectric polarization is from the negative polarization surface to the positive polarization surface. Due to the depolarization field, the entire ferroelectric has a higher electrostatic energy, which makes this state unstable; in order to make the ferroelectricity stable. There must be other factors that make the depolarization field shielded^[46].

The currently recognized screening mechanism is the generation of reverse domain structures within ferroelectric materials^[47]. In this case, the surface of the material will generate a corresponding charge to compensate for the depolarization field^[48]. This adsorbed external charge either comes from an external metal electrode or from a polar solution, and there have been a large number of experiments reported that such surface-adsorbed charged ions are an effective mechanism for screening the depolarization field^[49-52]. In some systems without a bottom electrode or ferroelectrics that have not

experienced a polar solution environment during the growth process, the system itself will also provide charges to screen the depolarization field.

1.2.3 Ferroelectric hysteresis curve and Curie temperature

The electric hysteresis loop is one of the most typical characteristics of ferroelectric materials, and it is also a direct manifestation of the nonlinear response characteristics of ferroelectrics to the external electric field. As shown in the figure is the basic schematic diagram of the hysteresis loop of multi-domain ferroelectrics^[53]. It can be seen that as the voltage rises, the domains inside the ferroelectric tend to be uniform in direction, so the ferroelectric polarization increases and reaches a saturated state. When the external electric field is reduced to 0, the ferroelectric polarization intensity of the ferroelectric does not decrease to 0, but maintains a higher value, which is called residual polarization. Continue to apply the reverse electric field, the polarization intensity will gradually decrease to 0, and a completely symmetrical reverse result will be obtained.

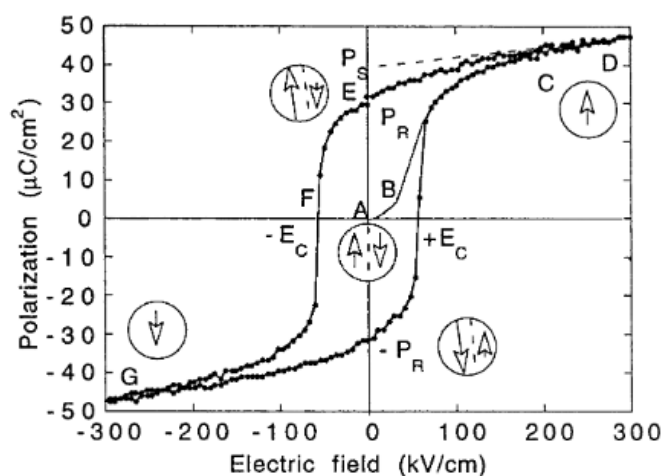


Figure 1.2 Typical ferroelectric hysteresis loop^[53].

As mentioned above, ferroelectrics respond to ambient temperature and maintain ferroelectricity within a certain range. But as the temperature rises, the ferroelectric phase will transform into the paraelectric phase at a certain temperature. The temperature point of this structural transformation is called the Curie temperature. For BaTiO₃, the Curie temperature is 393 K. Above this temperature, BTO will become a cubic paraelectric phase,

while below this temperature BTO maintains a tetragonal ferroelectric phase. Of course, in addition to the transformation of ferroelectrics to the paraelectric phase, the transformation between ferroelectric phases of different structures at a certain temperature will also occur. For example, when the BTO is at 273 K, the BTO will change from the tetragonal phase to the quadrature phase, but both the tetragonal phase and the quadrature phase are ferroelectric phases.

1.3 Topological structure in ferroelectrics

1.3.1 The structure and characterization of Ferroelectric topological materials

In ferroelectric materials, ferroelectric polarization is often not the same in direction and size. In other words, ferroelectric materials are often accompanied by various defects. Such as point defects, dislocations, domain walls, etc. Defects usually have a negative impact on the properties of the material, such as destroying the ferroelectric hysteresis loop^[54], weakening the dielectric response^[55], changing the transition temperature^[56], and so on. However, topological defects are generally regarded as excellent basic materials for memory devices that can be driven at low currents, and their application prospects are very broad.

The theory of topological defects was put forward by researchers in 1979, that is, non-continuous changes in order parameters in space are not always point defects, dislocations or domain walls, topological structure is also an important member^[57]. The first to be discovered is the topological structure existing in magnetic materials, such as magnetic vortex domains^[58], magnetic skyrmions^[59, 60], magnetic flux closure structures^[61, 62] and so on. These institutions are protected by the topological structure and are very stable, and at the same time they can be driven with low current, and at the same time meet the structural characteristics of high-density storage, so they have become a research hotspot.

The one-to-one correspondence between charge and spin makes the existence of ferroelectric topology inevitable. Naumov et al. speculated that there is a ferroelectric vortex domain structure in PTO nanorods by the method of first-principles calculations^[63, 64].

Pilania et al. predicted the existence of vortex domains in PTO nanowires through theoretical calculations^[65], and gave a theoretical scheme for the regulation of vortex domains^[66]. However, compared with the abundant theoretical results, the experimental result to demonstrate the existence of topological ferroelectric domain structure did not come out until 2009. They designed an experiment combined with stress modulation and found a ferroelectric closed domain structure in BaTiO₃^[67]. Then, Rodriguez et al. discovered that the vortex domain structure can exist in Pb(Zr_{0.4}Ti_{0.6})O₃^[68]. In 2011, Jia Chunlin et al. also observed the vortex domain structure^[69].

The flux closure structure discovered by Ma Xiuliang et al. in PTO/STO in 2015^[70] was the first to realize the design and acquisition of specific topology by adjusting the substrate stress, which paved the way for the acquisition of ferroelectric topology through stress modulation. Combined with the high-resolution spherical aberration corrected scanning transmission electron microscope, Ma Xiuliang's research group modulated the ferroelectric polarization in the PTO layer to continuously rotate and form a closed-loop flux by 90° domains. They also proposed that the size of the acquired domains can be controlled by adjusting the thickness of the PTO layer.

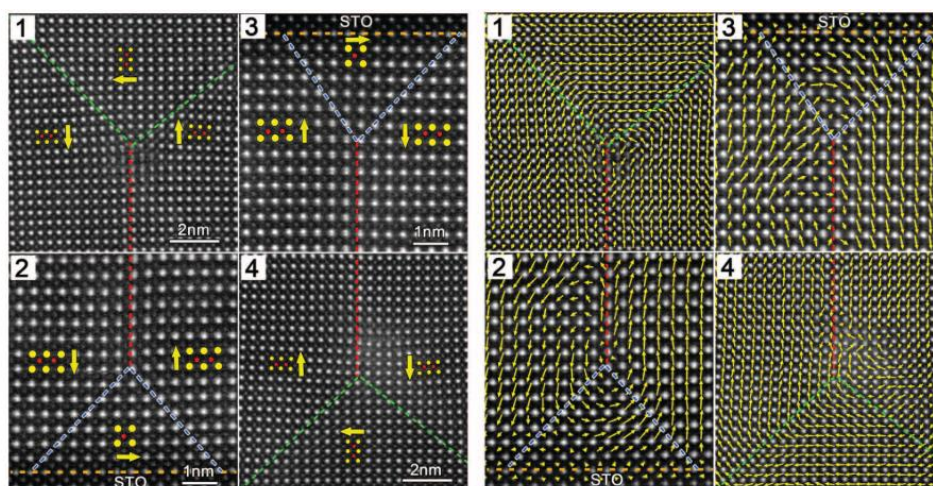


Figure 1.3 Superposition of HAADF-STEM images and Ti⁴⁺ displacement vector maps showing the closure quadrants^[70]. The red and yellow circles denote the positions of Ti⁴⁺ and Pb²⁺ columns, respectively. Arrows denote reversed Ti⁴⁺ displacement directions. The green and blue dashed lines indicate the 90° domain walls in areas 1 and 4, as well as 2 and

3, respectively. The red dashed lines indicate the 180° domain walls.

In 2017, on the basis of the above-mentioned one-dimensional periodic closed-loop flux domain, Ma Xiuliang's group prepared a two-dimensional periodic flux closure by regulating the stress and strain^[71]. It is also found that when the thickness ratio of adjacent PTO layers is 0.5, H-type domains and V-type domains will appear in the two layers respectively. Furthermore, the phase diagrams of the gradient energy, system elastic energy, electrostatic energy and other system energy varying with thickness are obtained through the method of phase field simulation.

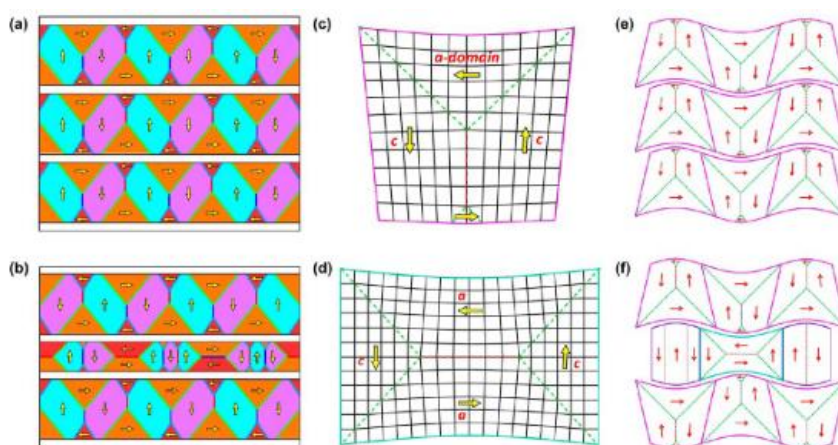
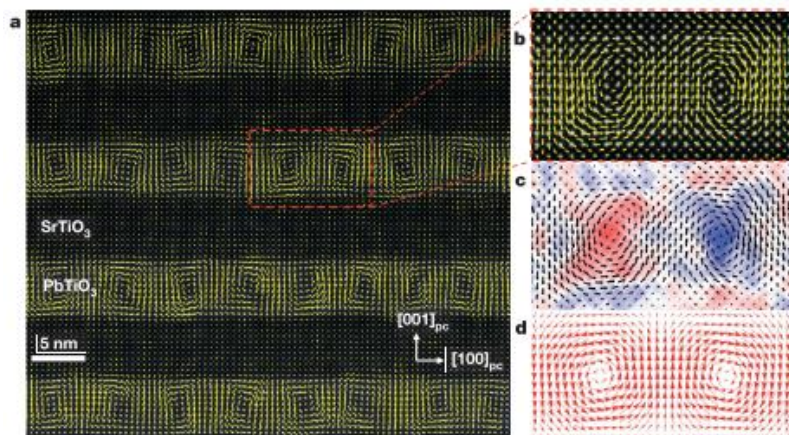


Figure 1.4 Schematics and strain analyses of flux-closure domain patterns in PTO/STO multilayers^[71]. (a) Two dimensional distributions of V domains in PTO layers when the thickness ratio of adjacent PTO layers is 1. (b) Besides V domains, H domains were found in thin PTO layers when the thickness ratio of adjacent PTO layers is about 0.5. Yellow arrows indicate Ps directions. Navy blue and red lines denote 180° domain walls. Green and light blue lines indicate 90° domain walls. (c,d) Schematics of lattice strain in vertical (c) and horizontal (d) flux-closure domain patterns, where black grids denote PTO lattices. (e) A schematic shows that when the thickness of each PTO layer is the same, the formation of the neatly arranged vertical flux-closure quadrants could prefer to accommodate the strain in each layer properly. (f) A schematic shows the case that the difference of thicknesses of adjacent PTO layers is relatively large.

In 2016 and 2019, Ramesh et al. from the University of California at Berkeley successfully prepared and discovered ferroelectric vortex domains^[72] and ferroelectric

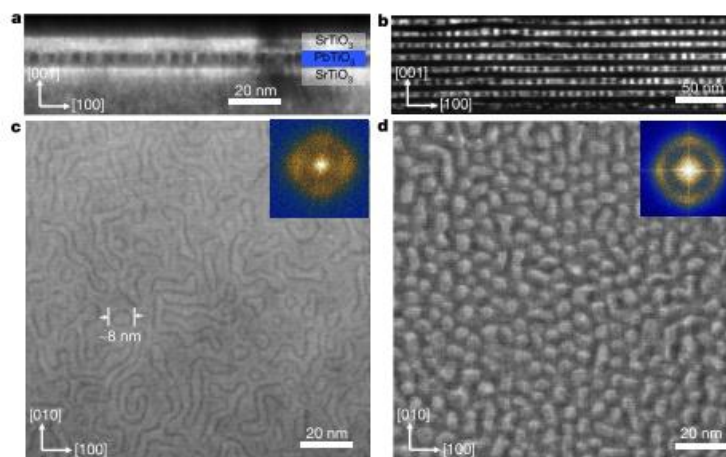
skyrmions^[73] in PTO/STO multilayer films, respectively. Their research points out that perfect ferroelectric vortex domains can be prepared in PTO/STO multilayer films through stress engineering. These vortex domains are arranged periodically in the PTO in the form



of left-handed and right-handed, and the period length is about 4 nm. Because it has been previously reported that the core of the vortex domain of BFO is very likely to be a conductive channel^[74], if the vortex domain of the PTO layer is also a conductive channel, then these channels with an interval of less than 4 nm will be important in the field of microelectronic devices. They also prepared the ferroelectric skyrmions structure with similar research methods, and found that this skyrmions at room temperature is modulated by the PTO/STO cycle. When there are more periods, the structure tends to be bubble-shaped; in a sandwich structure with only three layers, elongated strip-like domains are the main ones.

Figure 1.5 Observation of vortex–antivortex structures^[73].

In addition, Jia Chunlin's group discovered a stable wave domain structure^[75], Chen Longqing's group used phase field simulation to predict the spatial structure of the vortex domain^[76, 77], Gao Peng's group analyzed the fine structure of vortex using iDPC technology to determine the distribution of polarization in-plane and out-of-plane. These studies have



led to the discovery of various ferroelectric topologies one by one in ferroelectrics, and also developed a set of stress-control methods to prepare specific topological structures.

Figure 1.6 Observation of ordered skyrmions structure^[74].

1.3.2 The manipulation of ferroelectric topological structures

The research of the above ferroelectric topology structure shows that in the ferroelectric topology structure, the strain stress generated by the lattice mismatch between the substrate DSO and the PTO/STO causes the PTO layer to generate topological vortex and other topological structures. By adjusting the PTO layer thickness, the electrostatic energy, elastic energy, and gradient energy of the system can compete with various energies. When the energy of the system reaches a critical value, the topological vortex structure will be transformed into other forms of structure^[77, 78]. However, this method of acquire the topological structure by adjusting the thickness of the lattice layer cannot be applied to actual memory devices. Therefore, for a multilayer film structure with fixed lattice parameters, how to apply external field conditions to achieve the topological structure phase change is more realistic.

Zijian Hong et al. used the method of phase field simulation to explore the response process of the vortex domain structure under the condition of an external electric field^[76]. The study found that when an external electric field is applied in the out-of-plane direction through the probe, the topological structure would evolve. When the voltage is relatively low (5.2 V), the vortex domains will tend to move closer to each other to form a close pair to reduce the electrostatic energy of the system. Then as the voltage further increases, the two vortex lines close to each other will fuse together and form a bubble domain similar to the skyrmion structure. The bubble domain structure will tend to shrink at a higher voltage (10.4 V) and finally ruptured to form a domain wall composed of 90° domains. And this process also has a similar phenomenon under reverse voltage.

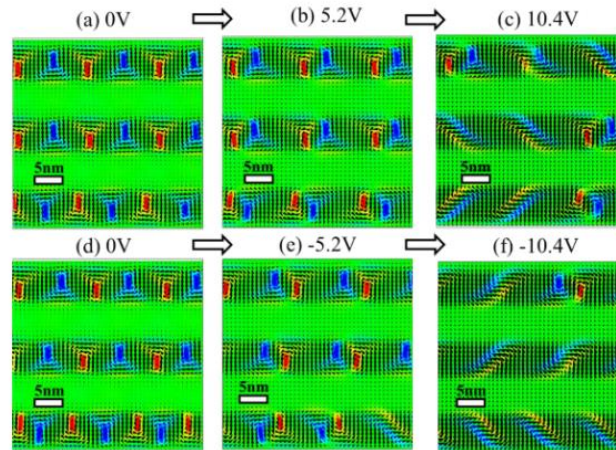


Figure 1.7 Cross-section view of the polarization pattern evolution under a small to large applied bias^[76]. (a)-(c), under applied bias of 0, 5.2 and 10.4 V, respectively. (d)-(f), under applied bias of 0, -5.2 and -10.4V, respectively. The reversible transition of vortex pairs to the a/c twin structure is demonstrated. Red and blue illustrate the positive (counter-clockwise) and negative vorticities (clockwise), respectively.

A. R. Damodaran et al. studied the topological phase transition of the topological vortex structure under heating conditions^[79]. Experimental results have found that when the temperature rises to 200°C, the mixed phase of vortex and a1/a2 will transform into a pure a1/a2 phase. When the temperature is further increased to 325°C, the ferroelectric phase will further transform into the paraelectric phase. This study reveals that the temperature field could be used to study ferroelectric phase transitions.

Pan Chen et al. used the in-situ TEM method to observe the transformation of the topological vortex structure under the applied stress field in real time^[80]. Their research found that vortex domain can be transformed into in-plane a-domain under relatively small stress. Further high-resolution results show that the vortex domain transition starts from the periphery and finally extends to the inner core, and the spatial position of a single vortex domain does not change significantly.

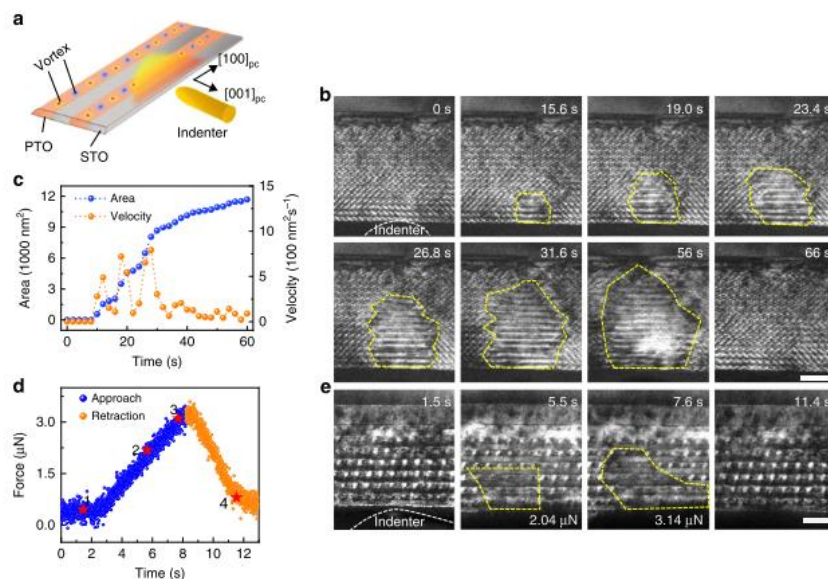


Figure 1.8 Mechanical manipulation of vortices by in situ transmission electron microscopy (TEM)^[80]. a, Schematic image of the experimental setup, with a mobile tungsten tip acting as an indenter for the mechanical manipulation of vortices. b, Chronological TEM dark-field image series formed by reflection with $g = (200)$ pc. Under the mechanical loads, vortex contrast gradually disappears. Scale bar, 40 nm. c, Corresponding transition area (blue line) and switching velocity (orange line) plotted as functions of time. d, Mechanical loads as a function of time, with the blue points representing the approach branch and orange points corresponding to the retraction branch. The highlighted red stars along with labels 1–4 correspond to images in e. e, Dark-field images showing the vortex evolution under certain measured mechanical stress. Scale bar, 20 nm.

In addition, Xiaomei Li et al. applied external electric field and force field to realize the transformation of topological flux-closure structure and ordinary ferroelectric phase^[81]. They found that flux-closure domain can be transformed into a/c domains and eventually c domain under the condition of an applied electric field. Flux-closure domain can be transformed into a/c domains and eventually become a domains under the condition of an applied force field. Shuai Yuan et al. used the method of theoretical calculation to explore the phase transition of the vortex domain under the applied force field^[82]. The above work has enriched the theoretical and experimental basis for the transformation of topological

vortex structure, and provided us with ideas for real-time observation of topological structure transformation at the atomic level.

1.4 A brief introduction to irreducible ferrielectrics

In ferroelectric materials, the generation of ferroelectricity means that the centers of positive and negative charges do not coincide, that is, the symmetry of spatial inversion is broken. Correspondingly, the appearance of ferromagnetism means that the symmetry of time inversion is broken. For a long time, the concept and behavior of the ferromagnetic system can always be found in the ferroelectric system: for example, if two sets of sub-lattices are anti-parallel, they are called antiferroelectrics, and they do not show macroscopic ferroelectricity; If the ferromagnetic sub-lattices are anti-parallel, it is called antiferromagnet, and it does not show ferromagnetism to the outside; similarly, paraelectricity corresponds to paramagnetism, and ferrielectricity corresponds to ferrimagnetism. However, there is always a deficiency in the above correspondence, that is, although ferrimagnetic materials are common, it is difficult to find a true ferroelectric material corresponding to it.

The first proposed ferroelectric materials were NaVO_3 and NaNbO_3 ^[83], but subsequent experiments did not support this claim^[84]. In the years of exploration, it was discovered that except for a few liquid crystal materials, ferrielectrics are very rare in solids^[85]. The main reason is that people have been controversial about how to define ferroelectricity for a long time. For example, CuInP_2S_6 has two sets of sub-lattices. The two pairs of sub-lattices have opposite ferroelectric polarization, which can be regarded as ferrielectrics; but if the two sets of sub-lattice are regarded as one unit, then it is no different from a normal ferroelectric^[86, 87]. Similar phenomena also occur in perovskite materials such as $\text{Ca}_3\text{Ti}_2\text{O}_7$ ^[88, 89], or other so-called ferrielectric materials^[90]. These materials can only be defined as reducible ferrielectric materials, because the characteristics of their two sublattices are accompanied by each other. Looking for a truly irreducible ferroelectric material is not only a supplement to the ferroelectric-ferromagnetic correspondence, but the discussion of its

physical origin is also of great significance to the development of condensed matter physics.

BaFe₂Se₃ is a member of the iron-based superconducting family^[91, 92]. The study by Shuai Dong et al. pointed out that BaFe₂Se₃ has two relatively independent sub-lattices^[93]. The two sets of sub-lattices each contain an iron ladder, and the iron atoms of the iron ladder will undergo tetramerization, so they will produce iron polarization in the opposite direction. The relatively long distance between the two sets of sublattices facilitates their independent behavior characteristics. Previous studies have also found the possibility of phase transition in BaFe₂Se₃ under external field conditions^[94]. Therefore, the study of the microstructure of BaFe₂Se₃ under external field conditions will help to explore the independence of its sublattice behavior, and has the potential to become a truly irreducible ferroelectric material.

1.5 Content and Research ideas of this thesis

The mutual coupling and interaction among some orders, such as the charge, spin, orbit of the strongly correlated electronic system, has produced a series of novel physical phenomena. As an important part of the system, ferroelectric materials have attracted widespread attention. If the ferroelectric polarization continuously rotates around the same center, it can form a so called topological structure, which has many advantages such as low-energy drive and high-density storage. There are a lot of theoretical and experimental work trying to explore ways to control the topological structure, but atomic manipulation and observation still has a series of technical challenges, and there are few real-time observations revealing the topological phase transition process. The understanding of the chirality of ferroelectric topology is also missing. On the other hand, there is no real irreducible ferroelectric material in the ferroelectric family. All these hinder the understanding and application of ferroelectric system. Therefore, in-situ manipulation and real-time observation at atomic-level on phase change, capturing the three-dimensional structure of the ferroelectric topological phase, finding the irreducible ferroelectric system are all very important scientific issues. This paper will introduce the following aspects:

(1) $\text{PbTiO}_3(001)/\text{SrTiO}_3(001)$ with DyScO_3 as the substrate is selected as the research object, and it is characterized through the atomic-level HAADF-STEM and EDS techniques. The PTO layer thickness is gradually controlled from 1 μc to about 21 μc by adjusting the PLD parameters. We explored the transformation of the topological structure of the PTO layer with different layer thickness, and analyzed the conditions of different topological structures from the point of view of stress analysis. Combined with the self-developed in-situ electrical method, real-time detection of the vortex topology in the 10 μc PTO layer under applied electric field was carried out at the atomic level, and the gradual transformation of the topology was explored. The further electron energy loss spectrum test characterizes the charge distribution of each state, and proposes the screening mechanism of the ferroelectric polarization in the single domain.

(2) Using the emerging electron tomography technology of transmission electron microscopy, we characterized the three-dimensional structure of ferroelectric vortex domains, combined with atomic-level image analysis and fitting methods, we analyzed the structural characteristics of topological vortex domains; Combined with the three-dimensional scale ferroelectric polarization calibration, we have proved the chirality of ferroelectric vortex domains.

(3) The atomic level characterization of BaFe_2Se_3 reveals the irreducible behavior of the two iron chains inside the unit cell. Combined with further in-situ thermoelectric tests, the independent behavior characteristics of BaFe_2Se_3 sub-lattices under external field are studied, which distinguishes BaFe_2Se_3 from the so-called ferroelectric materials whose sub-lattice behavior can be reduced.

Chapter 2 Experimental methodologies

Transmission electron microscopy is a technology used to characterize the microstructure of materials. After the electron beam penetrates the sample, the electron beam carrying the structural information of the sample is converged in various ways to image. In 1931, Ruska et al. built the world's first transmission electron microscope. In the 90 years so far, the transmission electron microscope has developed into an indispensable tool in the fields of material science and life science. It has played an important role in the fields of nanotechnology, semiconductor technology, and material science. And it has become a tool for characterizing sample morphology, structure, elements, valence, composition and other important information for multi-dimensional physical properties.

2.1 Transmission electron microscopy

2.1.1 Basic imaging principles of transmission electron microscope

In 1924, the German scientist De Broglie proposed for the first time that any object moving at a speed close to the speed of light has wave-particle duality. And it is proposed that the material wave wavelength satisfies the following formula :

$$\lambda = h/p = h/mv$$

In the formula, p is momentum, m is mass, v is velocity, and λ is wavelength. It is also known that the relationship between the kinetic energy of accelerating electrons and the accelerating voltage of the electric field is:

$$eU = mv^2/2$$

In the formula, e is the electron charge and U is the accelerating voltage. If considering the relativity correction of the fast electron mass m , there are:

$$m = \frac{m_0}{\sqrt{1 - (v/c)^2}}$$

Sorting out the above formulas:

$$\lambda = \frac{h}{\sqrt{2em_0U \left(1 + \frac{eU}{2m_0c^2}\right)}}$$

It can be known from the formula that the greater the acceleration voltage of the electron, the shorter the wavelength.

Abbe proved that the wavelength of the particle determines the resolution of the microscope. When the wavelength is fixed, the magnification that exceeds the resolving power is meaningless, because the obtained image will be blurred, and the minimum distance that the lens can resolve satisfies the formula:

$$d=0.61\lambda/n\sin\alpha$$

In the formula, λ is the wavelength of light, n is the refractive index, and α is half angle of the aperture. Combining Abbe and De Broglie, it can be concluded that the resolving power of the lens depends on the wavelength of the incident particle, and the wavelength of the incident particle depends on the acceleration voltage. Therefore, the incident particle can be increased by increasing the acceleration voltage, so that the resolving power of the lens can be greatly improved. In 1926, Davisson et al. verified that electrons also have wave-particle dualism through the method of electron diffraction, and their wavelength is extremely short. Based on this electron beam can replace light as a tool to observe the microstructure of matter, because the wavelength of electrons is much longer than that of light. Therefore, the resolution will be greatly improved, which is the theoretical basis of electron microscopy. For a general optical microscope, since the wavelength of visible light is about 4000 Å-8000 Å, according to the above formula, the resolution of the optical microscope is generally 1300 Å. Because moving electrons have wave-particle duality, their wavelength can reach 0.037 Å at an acceleration voltage of 100 kV, and the theoretical resolution calculated based on this can reach 0.02 Å, which makes it possible to observe the microstructure of most substances.

In 1926, Busch et al. proposed that an axisymmetrically distributed magnetic field is similar to a lens, which can focus the electron beam for imaging. This theory proposed a solution for how to manipulate electrons and provided a path for the actual manufacturing of electron microscopes. In the long years that followed, electron microscopy developed rapidly. In 1931, Knoll and Ruska obtained the aperture image of the electron optical system

with a magnification of 12-17 times. In 1931, Ruska modified the above device to prepare the world's first transmission electron microscope with a resolution of 500 Å. After that various commercial electron microscopes have also sprung up.

2.1.2 The imaging mode and structure of transmission electron microscope

After the electron beam is emitted from the cathode, it is first accelerated in the accelerating tube, then passes through the sample through the illumination system, and finally the electron beam passing through the sample is amplified and converged again and imaged by the imaging system. The final image is displayed through the observation window or electronic imaging mode. According to the above process, the basic structure of a transmission electron microscope can be divided into: illumination system, imaging system, observation and photographing system, sample stage and sample holder, vacuum system. As shown in the figure is a sectional view of the basic structure of a transmission electron microscope. The basic structure of transmission electron microscope will be introduced from these systems.

The illumination system can provide an illumination spot for the imaging system, the intensity of electron emission will determine the brightness of the spot. The electron gun is located at the uppermost part of the lighting system and mainly includes two types: field emission type and thermionic emission type. Thermionic lanthanum hexaboride single crystal is usually used as the filament, and the advantage of the field emission type is that the electron beam has high coherence and high brightness. For thermionic emission type, the electron beam density is affected by the fluctuation of the cathode. Therefore, the electron beam current and voltage must be stabilized. When the field emission type lighting system is working, an external electric field will be applied to the metal surface, so that the metal surface barrier becomes shallower. Internal electrons will be emitted from the surface through the barrier due to the tunnel effect. In addition, the lighting system also includes a condenser system and a deflection system.

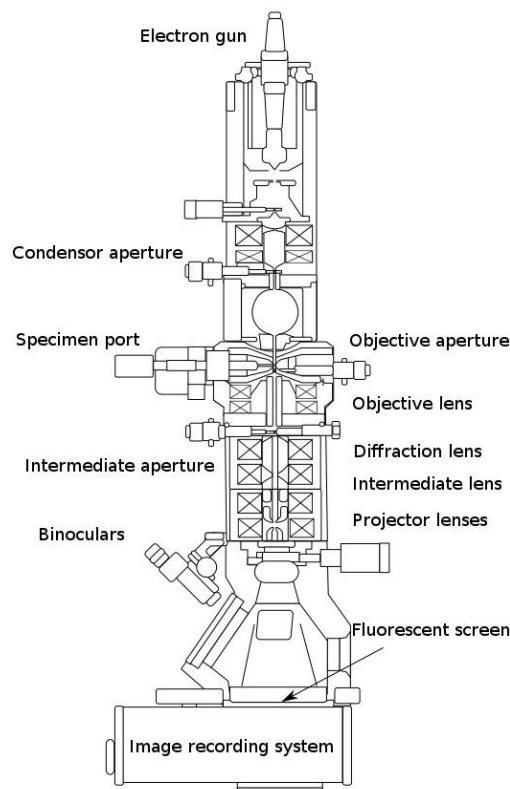


Figure 2.1 Schematic layout of the internal components in a basic transmission electron microscope ^[95].

The imaging system usually includes an objective lens, an intermediate lens, a projection lens, an objective aperture, and a selective diffraction aperture. In a transmission electron microscope, image is magnified once on the image plane of the objective lens, and then the image will be magnified twice by the intermediate mirror and the projection lens, and finally be imaged on the fluorescent screen through three magnifications. If the current of the intermediate mirror is changed, the object plane of the intermediate mirror becomes the back focal plane of the objective lens. In this case, the diffraction spectrum can be obtained; if it is moved to the object mirror plane, the real-space image can be obtained. The function of the objective lens is to form the primary magnified image and diffraction spectrum of the sample. Since the objective lens is the first-stage lens of the imaging system, various aberrations produced by the objective lens will be gradually enlarged by the post-stage lens. Therefore, it is necessary to ensure that the objective image aberration is as small as possible. Imaging in objective lens is mainly achieved by the magnetic field behind

the sample.

The function of the intermediate mirror is to project a magnified image formed by the objective lens onto the object plane of the projection lens. The intermediate mirror can control the imaging to form an image mode or diffraction mode: when the intermediate mirror current is changed so that the image plane of the objective lens is transferred and enlarged, it is the image mode; if the back focal plane of the objective lens is transferred and enlarged, it is the diffraction mode. The projection mirror is responsible for receiving the image transmitted by the intermediate mirror and further magnifying and projecting it on the phosphor screen.

The observation and recording system includes phosphor screens, cameras, imaging boards, etc. The phosphor screen generally uses zinc sulfide doped with impurities, so that the phosphor screen can emit green light with a wavelength of 550 nm. The size of zinc sulfide determines the resolution of the phosphor screen. Usually zinc sulfide grain size is 10 μm , and the screen resolution is 10-50 μm . Since X-rays are generated inside the transmission electron microscope, in order to shield the X-rays inside the electron microscope, a glass observation window is usually made of lead glass. At the same time, images can also be obtained through a video camera or camera. The camera is another component of the image observation and recording system. The imaging plate is used to record images by coating light visualization phosphors on a plastic substrate.

The sample holder includes in-situ heating holder, in-situ electrical holder, and in-situ freezing holder, etc.

The vacuum system uses multi-stage vacuum systems such as molecular pumps and ion pump diffusion pumps to maintain the highest possible vacuum inside the electron microscope, thereby reducing electron scattering and ensuring image contrast.

The transmission electron microscope can acquire images in two modes: Transmission Electron Microscopy (TEM) and Scanning Transmission Electron Microscopy (STEM). In the TEM mode, the electron beam passes through the sample to reflect diffraction contrast and phase contrast; while in STEM mode, the incident electrons scan line by line on the

sample surface area with a convergent electron beam with a diameter of less than 1 Å. In this mode, probes with different acceptance angles can be used to receive signals. According to the different acceptance angles, the image can be divided into annular dark field (ADF) and high angle annular dark field (HAADF). Among them, the HAADF image is also called Z-contrast image. Its image contrast is positively correlated with the square of the atomic number, and its image contrast will not be greatly reversed by underfocus and different sample thickness^[96-98], so this model has great advantages in characterizing different elements. In addition, this mode is also used to collect inelastic scattered electrons by using the electron energy loss spectrum detection to perform element valence analysis.

When an electron beam enters a specimen, there are a variety of possible interactions between the electrons and the atoms of the specimen. Figure 2.2 shows a brief diagram of these possible interactions. For a very thin specimen, many electrons can pass through the specimen without any interaction: these are referred to as unscattered electrons. The remaining electrons are scattered and can be divided into elastically scattered electrons and inelastically scattered electrons. These signals are used in the microscope to give detailed information about the specimen.

The elastically scattered electrons are those electrons that passed through the specimen and interacted with the atoms yielding only a momentum transfer. These electrons carry only structural information about the specimen and they mostly contribute to conventional TEM including bright field (BF), dark field (DF) imaging and high resolution TEM (HRTEM) imaging. The inelastically scattered electrons have interacted with atoms yielding also energy transfer. The electrons transfer energy to the specimen in different ways such as phonon excitation, valance (energy band) excitation and inner shell ionization. Thereafter, the electrons exit the specimen carrying chemical information, meanwhile when an excited electron returns to its stable state, it generates secondary signals such as Auger electrons or X-rays. All these signals can be used for analytical microscopy such as energy dispersive X-ray spectroscopy (EDX) and electron energy loss spectroscopy (EELS).

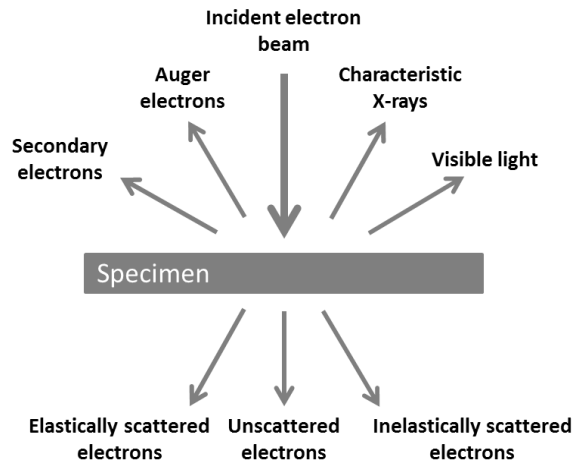


Figure 2.2 Simplified illustration of electron beam-sample interactions.

2.1.3 Causes and elimination of aberrations in electron microscopy

For current electron microscopes, the actual resolution is often much smaller than the theoretical resolution. The fundamental reason is that the magnetic lens will produce a variety of aberrations. These aberrations make the resolution of general electron microscope limited to only 2 Å (theoretical resolution is 0.02 Å). The origination and elimination methods of several aberrations are briefly described below.

For optical microscopes, the refractive surface that can form an ideal image is not a standard spherical surface, but a complex-shaped surface that is manufactured using complex processing methods. However, due to manufacturing cost and technology, spherical refractive surfaces are generally used. For spherical surfaces, the edge of the lens has a stronger refractive power for rays, so the beam after passing through the lens is not focused on the same point. The same problem exists in the electron microscope. The electron beam will no longer focus on the same point after passing through the magnetic lens. The schematic diagram is shown in the figure. The original with the smallest diameter is the smallest diffuse circle, and this position is the best focus point of the image. The smaller the minimum diffuse circle, the smaller the spherical aberration of the image. The mathematical expression of the spherical aberration is

$$\delta_s = C_s \alpha^3$$

Among them, δ_s is the radius of the smallest diffuse circle, C_s is the spherical aberration coefficient, and α is the half of the minimum aperture angle (rad). Usually the C_s of the objective lens is equivalent to its focal length, and C_s in most lenses are 3 mm; the C_s of modern objective lenses is about 0.3 mm. To further eliminate spherical aberration, a special lens is required, which will be described in detail below.

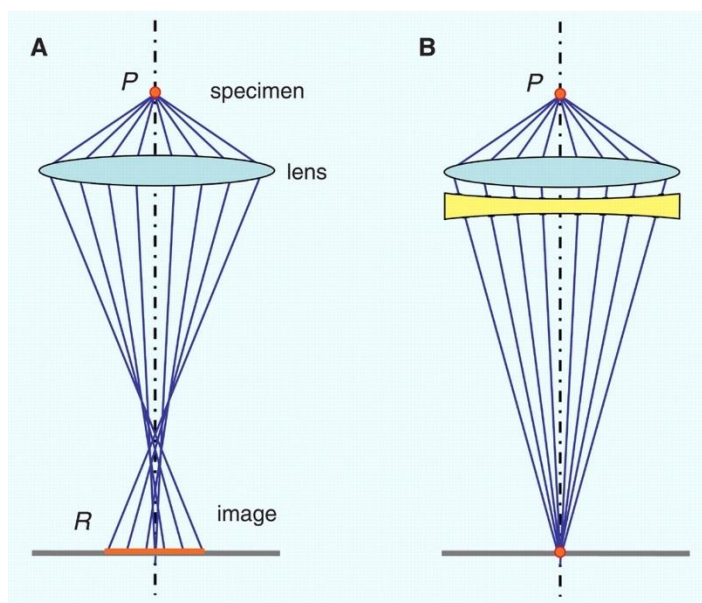


Figure 2.3 Schematic illustration of spherical aberration (A) and after correction (B)^[99].

The above introduction mentioned that the wavelength of the electron beam is related to the acceleration voltage, and the shorter the wavelength, the higher the resolution, so increasing the acceleration voltage of the transmission electron microscope is a feasible way. The current general 200 kV electron microscope has a resolution of 0.19 nm, a 300 kV electron microscope has a resolution of 0.169 nm, and 400 kV increases the resolution to 0.163 nm. However, the method of increasing the voltage of the transmission electron microscope to reduce the resolution is limited. High-voltage piezoelectric mirrors are expensive. On the other hand, the accelerating voltage is too high and the electron energy is high, which cannot be performed on the samples that are sensitive to electron beams.

In order to improve the resolution of the fixed voltage transmission electron microscope, people have adopted a new method of multi-level corrector to achieve this. Heider et al. successfully manufactured a spherical aberration corrector in 1998^[100-102]. The

spherical aberration correction of the objective lens is realized by two sets of extra electromagnetic lenses.

Taking the 200 kV Philips CM200 FEG ST as an example, the point resolution will increase from 0.24 nm to 0.13 nm after installing the spherical aberration corrector. In addition, the different installation positions of the spherical aberration corrector determine the difference in the corrected image mode. The spherical aberration corrector installed under the objective lens will improve the resolution of the TEM mode; the spherical aberration corrector installed under the condenser lens will improve the resolution of the STEM mode.

Astigmatism is another aberrations. It is due to the destruction of the rotational symmetry of the magnetic field, which causes the magnetic lens to have different focusing capabilities in different directions. The causes of astigmatism include internal pollution of the pole shoe, uneven structure of the pole shoe material, and asymmetrical position of the pole shoe. Among the factors that cause electron microscope image aberration, astigmatism is often the most obvious. Therefore, astigmatism can be eliminated by introducing a correction magnetic field whose intensity and orientation can be adjusted.

Chromatic aberration is also an important factor that causes aberration in electron microscope images. Since the energy of incident electrons cannot be exactly the same, and the greater the energy, the longer the focal length, so electrons with different incident energies will have different focal lengths. The reasons include: the energy loss when penetrating the sample is different, the initial velocity of the cathode emission is different, and the acceleration voltage fluctuation. In order to make the chromatic aberration as small as possible, the voltage and current stability should be as close as possible to about 2×10^{-6} . In addition, modern electron microscopes reduce it as much as possible by increasing the acceleration voltage, adding a monochromator, and adjusting the polarity of the lens chromatic aberration.

2.2 Electron energy loss spectrum (EELS)

2.2.1 The principle of electron energy loss spectrum

The electron energy loss spectroscopy (Electron Energy Loss Spectroscopy, EELS) technology can characterize the valence state of elements. The basic principle is that the electron beam with the same initial energy passes through the sample and then undergoes inelastic scattering, which results in different energy and energy loss. Most of the electrons continue to scatter forward (usually the scattering angle is less than 10 mrad)^[103]. The EELS detection equipment deflects these electrons through a magnetic prism. Since electrons of different energy will be deflected at different angles, they can be deflected at different angles. The deflected electrons are collected, and the electron energy loss is the abscissa, and the electron intensity (the number of electrons with the same energy collected) is the ordinate. These energies are plotted on the same spectrum to obtain the electron energy loss spectrum. Compared with EDS technology, which can only characterize element types, electron energy loss spectroscopy technology can characterize the same elements in different valence states, which is of great significance for understanding the valence state, electronic structure, and energy band width of materials.

The zero loss peak (ZLP) indicates that the electrons that have not been inelastically scattered. Since most of the electrons passing through the sample are not scattered, the peak height of the zero loss peak is relatively strong. The peak width of ZLP is an important parameter showing the energy resolution.

The low energy loss peak (mainly the plasma peak) corresponds to the collective oscillation of valence electrons, and its width represents the attenuation effect of the single-electron transition, so it can be used to estimate the sample composition and thickness.

The high-energy loss peak is mainly composed of extensive fine structure, energy loss near-edge structure, and ionization loss peak. Since the energy of the shell electrons around the nucleus is different, when the incident electron collides with the sample atom, the

energy of the different shell atoms being collided and getting rid of the nucleus is different, so the different energy lost by this part of the incident electron can be used to characterize different shells electronic. Among them, the energy-loss near-edge structure (ELNES) represents that the inner electrons get energy but not enough to get rid of the bond of the nucleus, so they only jump to a higher energy level. Therefore, ELNES can be used to characterize information such as the electronic energy level distribution of the sample. The extended energy-loss fine structure (EXELFS) can be used to determine the position of ionized atoms and the information of neighboring atoms.

2.2.2 Compare EELS with traditional element analysis techniques

In transmission electron microscopy, the more traditional method used to characterize elements is energy dispersive X-ray spectroscopy, referred to as EDX or EDS. The basic principle of energy spectroscopy is to measure the characteristic X-rays excited by the incident electron beam after passing through the sample to determine the type and content of elements. Comparing the electron energy loss spectrum with the EDS, the electron energy loss spectrum could provide accurate information of the electronic structure, but it also has the disadvantages of high requirements of sample thickness, and the experiment operation is difficult. In general, the main advantages and disadvantages are compared and listed in the following two points.

One is that for the incident electron beam of the same intensity, the electron count of EELS is more obvious. The reason is that on the one hand, the X-ray fluorescence yield is very low for elements with atomic number less than 11, so the energy spectrum is not suitable for light elements; in addition, the angular range of the transmitted electron beam is small when collecting the electron energy loss spectrum, so the information that the receiver can collect accounts for 20% to 50% of all electrons, and the EDX probe only receives the signal in one direction, while X-rays is transmitted to each direction. Therefore, the acceptance rate of the EDX collected signal is relatively low, probably only 1%. In this regard, a research group conducted research and found that EELS is indeed more sensitive

to low-content elements than EDX^[104]. In addition, for some samples with lower atomic numbers, EELS also has a unique advantage, with a higher probability that the inner shell will be excited. At the same time EELS also has better spatial resolution. Since the electron energy loss spectrum is equipped with a limited-angle diaphragm, the electron beam broadening and the electron beam expansion caused by elastic scattering are smaller.

Second, for the sample thickness, EELS usually requires a relatively low sample thickness. When the sample is too thick, the incident electron beam will undergo severe multiple scattering. Therefore, EELS will inevitably avoid backgrounds. When the background is too large, the signal-to-noise ratio will be severely affected, so EELS usually requires a thinner sample (preferably below 50 nm). EDX usually does not have such strict requirements on sample thickness.

Chapter 3 The manipulation of topological structure on ferroelectrics

Topological structures based on controllable ferroelectric or ferromagnetic domain configurations offer the opportunity to develop microelectronic devices such as high-density memories. Despite the increasing experimental and theoretical insights into various domain structures (*e.g. polar spirals, polar wave, polar vortex*) over the past decade, manipulating the topological transformations of polar structures and comprehensively understanding its underlying mechanism remains lacking. By conducting an *in-situ* non-contact bias technique, here we systematically investigate the real-time topological transformations of polar structures in $\text{PbTiO}_3/\text{SrTiO}_3$ (PTO/STO) multilayers at an atomic level. The procedure of vortex pair splitting and the transformation from polar vortex to polar wave and out-of-plane polarization are observed step by step. Furthermore, the redistribution of charge in various topological structures has been demonstrated under an external bias. This provides new insights for the symbiosis of polar and charge and offers an opportunity for a new generation of microelectronic devices.

3.1 Introduction

Domain structures in materials are of great significance considering their relationship with ferroelectricity, conductivity, magnetism and other abundant materials properties. A variety of topological polar structures have been discovered and evaluated, such as flux-closure and vortex domain structures^[68-70, 72, 75, 77, 105, 106]. It has been theoretically predicated that an electric field or a mechanical loading has the ability to switch domain configurations between vortex and other ferroelectric domains in ferroelectric systems^[107, 108]. Exploring a practical pathway to engineer these topological defects and associative states of matter (*e.g. polar spirals and skyrmions*^[109-111]) is highly desired from both academic importance and promising technological applications. Particularly, the electric-field control

of topological structures is of great interest because it offers the potential for new cross-coupled functions^[112, 113]. More importantly, considering the extremely short periodicity of the vortex domains, with various switchable domain patterns which can be modulated by an external factor, PTO/STO multilayers may pave the way for the implementation and design of a new generation of high-density microelectronic devices based on domain engineering.

However, existing reports focus on macro scale and ex-situ manifestation, direct observation of the dynamic evolution of a phase transition at an atomic level remains a great challenge. Using a combination of scanning transmission electron microscopy (STEM) and in-situ non-contact bias technique, a real time mapping of the ferroelectric polarization under an electric bias was carried out on an atomic scale. The electron energy loss spectroscopy (EELS) results provide hints on the variation of the electronic structure during the topological transformations. Our methods allow us to realize a controllable transformation, and the connection of various topological structures is experimentally presented.

3.2 Technique detail

3.2.1 Sample preparation

The $(\text{PbTiO}_3)_n/(\text{SrTiO}_3)_{10}$ multilayers were epitaxially grown on orthorhombic $\text{DyScO}_3(110)$ substrates with a ~ 5 nm SrRuO_3 buffer layer using pulsed laser deposition. To obtain well-defined ScO_2 -terminated substrates, the DyScO_3 substrates were treated before deposition as follows. They were first annealed at 1000°C for 2 hours in air, and then wet etched using 12 and 1 M NaOH-DI water solution in an ultrasonic bath for 1 hour^[114]. While SrTiO_3 and SrRuO_3 targets were stoichiometric, a $\text{Pb}_{1.2}\text{TiO}_3$ target was used to ensure layer-by-layer growth. All depositions were performed at 600°C with an oxygen pressure of 0.1 mbar. A KrF laser (248 nm) was used with a repetition rate of 2 Hz. The laser fluence was 2.1 J/cm^2 for depositing the SrRuO_3 buffer layer, and 1.5 J/cm^2 for depositing the $\text{SrTiO}_3/\text{PbTiO}_3$ multilayer. After that, the thickness of the SrTiO_3 films was fixed at 10 uc and PbTiO_3 films varied gradually from 1 uc to 21 uc and from 5 uc to 11 uc. The

layer-by-layer mode was maintained throughout the entire synthetic process. The thickness of each film was monitored by Reflection High Energy Electron Diffraction (RHEED). After deposition, the samples were cooled down to room temperature under an oxygen partial pressure of 200 mbar to promote full oxidization.

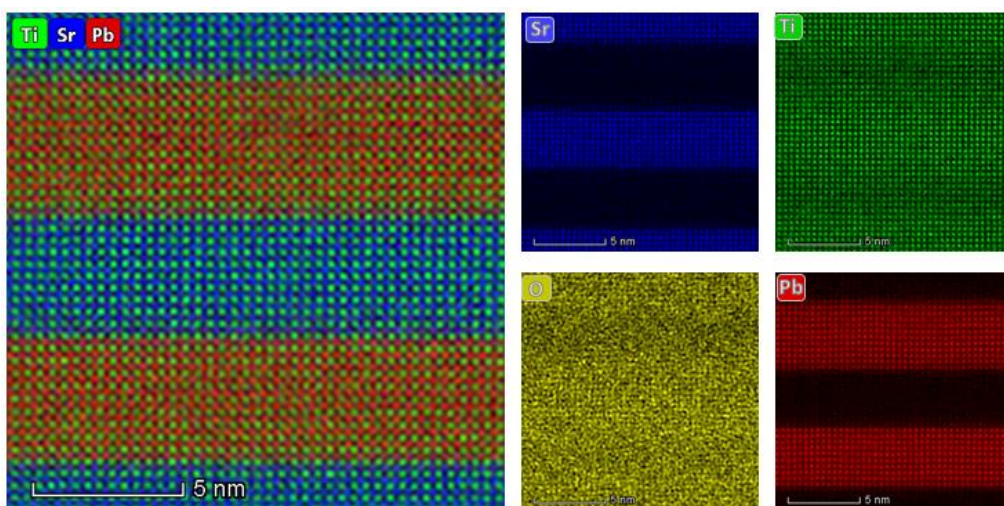


Figure 3.1 EDS-mapping of Pb, O, Sr, Ti. Those images show that the interface of PTO/STO is atomically sharp. Due to the distortion of the oxygen octahedra, the column effect of the oxygen atoms is reduced in STEM mode; thus a slightly darker contrast in the O map at the position of the PTO layer is to be expected.

3.2.2 Parameter chosen for electron microscopy

Samples were cut into lamellas with the widest faces perpendicular to the [010] direction using Focused Ion Beam (FEI Quanta 3D FEG) for observation by transmission electron microscopy. We used spherical aberration corrected electron microscopy (FEI Titan G2 80-200 ChemiSTEM, 30 mrad convergence angle, 0.8 Å spatial resolution) to acquire atomic resolution HAADF-STEM images; the image noise was corrected using Digital Micrograph. All STEM images in this work are filtered in Fourier space using a grid mask to select for the lattice frequencies and by low and high pass annular filters to remove the zero frequency and high frequency noise above the information transfer limit. Electron Energy Loss Spectroscopy (EELS) was also performed to verify whether there are changes in the valence state by using a Themis G2 60-300 at 120 kV (with EELS energy

resolution ≤ 0.3 eV). We determine the center of the atom column by a mathematical method involving Gaussian Fitting based on Matlab. Polarization mapping is then performed by calculating ion displacements in the HAADF-STEM images. As the local atom displacements are extremely tiny, most HAADF images are overlaid based on 12 or more images to obtain more accurate atom positions and to correct the small sample drift ($< 0.5 \text{ \AA min}^{-1}$). In order to minimize the potential damage caused by the ion beam in FIB, we adjusted the voltage down to 2 kV and the electric current of ion beam down to 27 pA.

3.2.3 Phase-field simulations

In the phase-field modeling of the $\text{PbTiO}_3/\text{SrTiO}_3$ superlattice, the polarization (\mathbf{P}) evolution is governed by the time-dependent Ginzburg-Landau (TDGL) equation:

$$\frac{\partial P_i(\vec{r}, t)}{\partial t} = -L \frac{\delta F}{\delta P_i(\vec{r}, t)} \quad (i = 1, 2, 3)$$

Where L , r , and t represent the kinetic coefficient, spatial position vectors and time, respectively. The free energy F contains the contributions of the Landau, elastic, electrostatic and gradient energy, *i.e.*,

$$F = \int (f_{\text{Landau}} + f_{\text{Elastic}} + f_{\text{Electric}} + f_{\text{Gradient}}) dV$$

The Landau energy density is expanded by ‘‘Landau polynomial’’.

$$f_{\text{Landau}} = \alpha_{ij} P_i P_j + \beta_{ijkl} P_i P_j P_k P_l + \gamma_{ijklmn} P_i P_j P_k P_l P_m P_n$$

The elastic energy density can be expressed by the following equations:

$$f_{\text{Elastic}} = \frac{1}{2} C_{ijkl} e_{ij} e_{kl} = \frac{1}{2} C_{ijkl} (\varepsilon_{ij} - \varepsilon_{ij}^0) (\varepsilon_{kl} - \varepsilon_{kl}^0)$$

Where C_{ijkl} , e_{ij} , ε_{ij} and ε_{ij}^0 are elastic stiffness tensor, elastic strain, total strain and eigen strain, respectively. The eigen strain is the phase transformation strain given by electromechanical coupling with the expression: $\varepsilon_{ij}^0 = Q_{ijkl} P_k P_l$. Q_{ijkl} is the electrostrictive coefficient tensor.

The electric energy density is calculated as

$$f_{\text{Electric}} = -\frac{1}{2} K_{ij} \varepsilon_0 E_i E_j - E_i P_i$$

Where K_{ij} is the background dielectric tensor constant, ϵ_0 is the dielectric permittivity of the vacuum and E_i is the local electric field defined by poisson equation:

$$E_i = -\nabla_i \phi.$$

With the assumption of pseudocubic, the gradient energy density is given by:

$$f_{Gradient} = \frac{1}{2} G_{ijkl} P_{i,j} P_{k,l}$$

Where G_{ijkl} is the gradient coefficient tensor, $P_{i,j}$ is for the spatial differential of the polarization vector:

$$P_{i,j} = \frac{\partial P_i}{\partial X_j}$$

More details of each energy density have been reported previously^[115-120]. A three-dimensional system is set up, using a size of $(200\Delta x) \times (200\Delta y) \times (250\Delta z)$ with $\Delta x = \Delta y = \Delta z = 0.4$ nm. The thickness of the substrate, film and air are $30\Delta z$, $141\Delta z$ and $79\Delta z$, respectively. In the film area, 9 unit cells of PbTiO_3 layers and 9 unit cells of SrTiO_3 ones as well as one transition layer between PbTiO_3 and SrTiO_3 are used to simulate the superlattice system. The pseudo-cubic lattice constants for PbTiO_3 and SrTiO_3 are 3.9547 \AA and 3.905 \AA , respectively. The DyScO_3 substrate lattice constants along the x- and y-direction are taken as 3.952 \AA and 3.947 \AA , respectively^[121]. Periodic boundary conditions are applied along the x- and y-directions, and a superposition method is used along the out-of-plane direction^[122]. The short-circuit electric condition is applied, where on the top and bottom, electrical potentials are the applied bias and 0, respectively. A mixed elastic boundary condition is assumed where the displacement is zero far away from the substrate, and out-of-plane stress is free at the top of the film^[115-120, 123]. Random noise is used to simulate the annealing process as the initial nuclei.

3.2.4 Determination of the atomic displacements

The polar vector determination was performed on the Cs-corrected HAADF-STEM images using local A- and B-site sublattice offset measurements. In a tetragonal PTO structure at room temperature, Ti^{4+} shifts relative to the Pb sublattice, while oxygen octahedra shift in the same direction but with a larger displacement, as shown in Fig. 3.4; δ_{O}

and δ_{Ti} are the displacements along the *c*-axis. The shift breaks the cubic symmetry, resulting in an internal dipole with a direction pointing from the center of negative charge to the center of positive charge, hence the polarization direction of PTO is opposite to the shift direction of Ti^{4+} and this offset can be used to infer the full polarization (*P*). Thus, for traditional HAADF images, we use the Ti to infer the offset of the Ti-‘centered’ oxygen octahedra for defining the electric dipole. Displacement vectors corresponding to local offsets between the A- and B-site sublattices were calculated by determining atomic positions by fitting each atom site by a spherical Gaussian using an algorithm in Matlab^[124, 125]. For the iDPC-STEM images, the oxygen atoms can also be acquired, so we calculated the spontaneous polarization according to the position of both Ti and O atoms.

3.3 The characterization of PTO/STO at initial state

We designed and grew $\text{PbTiO}_3/\text{SrTiO}_3$ (PTO/STO) multilayer films on a $\text{SrRuO}_3/\text{DyScO}_3$ substrate. $\text{PTO}_{(n)}/\text{STO}_{(10)}$ multilayers with $n=1-21$ (the gradient of thickness is around 2 unit cells) were grown by pulsed laser deposition (PLD) and characterized by Cs-corrected STEM. A typical low-magnification high-angle annular dark-field STEM (HAADF-STEM) image of the cross-section reveals the layer uniformity (Fig. 3.2). Atomic resolution EDS-mapping confirms sharp and coherent interfaces (Fig. 3.1 and 3.2b). Implementing a displacement algorithm, the vector map of the polar displacements within the $n=1-21$ multilayer (Fig. 3.2) shows the domain evolution process. With the thickness of the PTO layer continuously increasing from 2 unit cells (uc) to over 20 uc, the corresponding domain configuration evolves from a/c domain (in which the polarization direction is along the *a* or *c* axis) to an unexpected stable wave state and vortex state, and finally to a flux closure state. The variation process within the $\text{PTO}_{(n)}/\text{STO}_{(10)}$ film is somewhat different from that in the previously reported $\text{PTO}_{(n)}/\text{STO}_{(n)}$ superlattices^[77]. Phase-field modeling of the $\text{PTO}_{(n)}/\text{STO}_{(10)}$ multilayer was performed to ascertain the evolution process of the domain patterns as a function of the PTO thickness (see Fig. 3.3).

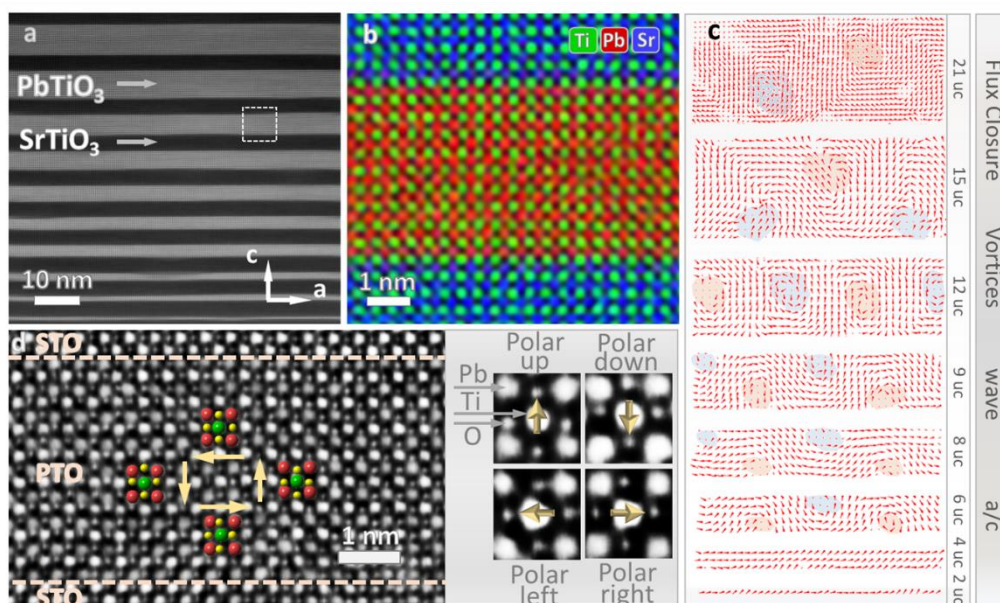


Figure 3.2 Structural characterization of the $(\text{PbTiO}_3)_n/(\text{SrTiO}_3)_{10}$ multilayer. a, HAADF-STEM image of the film, recorded with the incident electron beam parallel to the $[010]_{\text{pc}}$ direction. b, EDS-mapping of Pb, Sr and Ti shows that the interface of PTO/STO is atomically sharp. This region is extracted from the white box in a. c, Ti atom displacement vector maps based on experiment, showing the domain evolution with changing PTO thickness. Red and blue regions indicate the clockwise and counterclockwise vortex pairs^[126, 127]. d, Superposition of the iDPC-STEM image and a structure model of PTO, showing the atom displacements around the vortex structure. The red, green and yellow dots denote the positions of Pb^{2+} , Ti^{4+} and O^{2-} columns, respectively. Arrows denote the polarization direction. The dashed lines indicate the interface between PTO and STO. The zoom-in images attached to this iDPC-STEM image exhibit the unit cell of PTO along $[010]_{\text{pc}}$ in which positions of Ti, O and Pb are clearly shown.

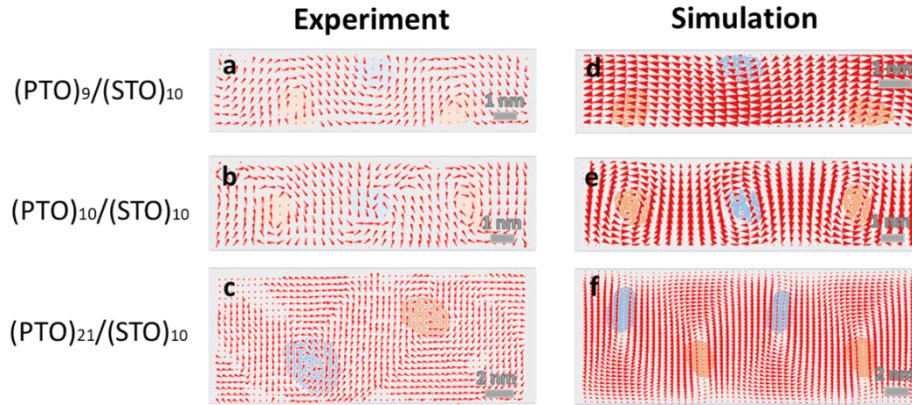


Figure 3.3 Experiment (a-c) and simulation (d-f) results of the domain pattern as function of the PTO thickness. a and d for a wave structure at a PTO layer of 9 uc; b and e for a vortex structure in a PTO layer of 10 uc; c and f for a flux closure structure for a PTO layer of 21 uc.

In order to accurately verify the position of all atoms, including oxygen, and to evaluate the spontaneous polarization (P_s) unit cell by unit cell, the Integrated Differential Phase Contrast (iDPC) STEM imaging technique^[128] is employed (Fig. 3.2d and Fig. 3.4). Compared with annular bright-field (ABF) STEM, iDPC provides better visualization ability on the sample with the same thickness for measuring the atomic column positions^[36].

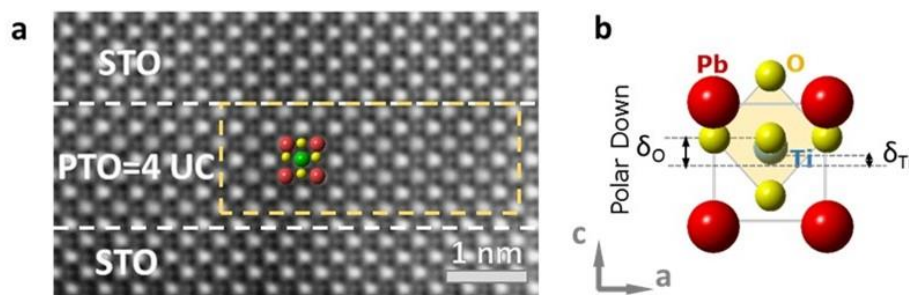


Figure 3.4 a, Atomic-level cross-section iDPC image of a 4 uc PTO layer superimposed with the structure model of PbTiO_3 . In the room temperature tetragonal PTO structure, Ti^{4+} shifts relative to the Pb sublattice, while the oxygen octahedra shift in the same direction but with a larger displacement. According to the position of Ti and O atoms, we calculated the spontaneous polarization (P_s) of some unit cells (yellow rectangle). The P_s value of the PTO (4 uc) is $63.63 \pm 3 \mu\text{C}/\text{cm}^2$, close

to that of bulk PTO ($\approx 75 \mu\text{C}/\text{cm}^2$). b, Unit-cell projection of tetragonal PTO along the crystallographic b-axis. The displacement of Ti and O atoms with respect to the center of the Pb atoms along the c-axis are denoted as δ_{Ti} and δ_{O} .

Such domain evolution is usually accompanied by a complicated interaction of multi-factors^[77, 79, 107] and therefore the strain evolution needs to be clarified first. The corresponding strain evolution across multilayers from 1 uc to 21 uc is confirmed via the geometric phase analysis (GPA) (see Fig. 3.5 and 3.6). These facts point towards a close relationship between the evolution process of the polar structure and the strain evolution, which has been observed earlier^[70, 129]. To explore the physical origin underlying this transformation, we calculated the evolution of the energy components of the ferroelectric domain, as shown in Fig. 3.7; the decrease of the energy density of the PTO layer is accompanied with an increase of the electric and gradient energy density and a drop of the average elastic and Landau energy density. This confirms the phase transition sequence with increasing PTO thickness from the energy aspect, which supports our following experimental observations and gives a theoretical clarification on the domain evolution.

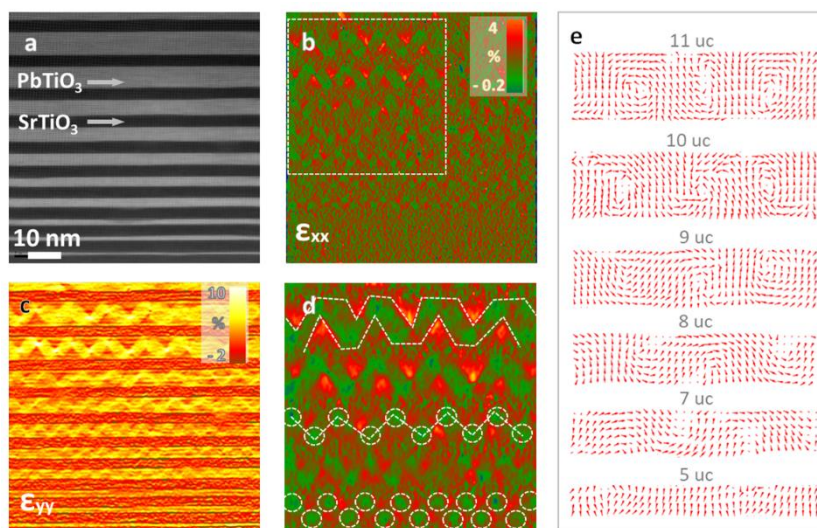


Figure 3.5 In plane (ϵ_{xx}) and out-of-plane strain (ϵ_{yy}) maps. a is low-magnification STEM images of the cross-section of a $(\text{PbTiO}_3)_n/(\text{SrTiO}_3)_{10}$ multilayer, with $n=1-21$. b-c are

extracted via the geometric phase analysis (GPA). The strain shown displays a clear spatial arrangement related to the domain patterns. d, GPA analysis of the STEM data extracted from white box in (b) showing that ϵ_{xx} also exhibits a periodicity characteristic, which is added with some marker lines to make the characteristic more visible. e, As to acquire a better understanding of the transition state between vortex and wave, a more detailed polar map was performed on the $n=5-11$. The Ti atom displacement vector maps show the domain evolution with changing PTO thickness. At a PTO thickness layer of 5 uc, the domain configuration reveals the polar down state. As the layer thickness increases, the domain configuration reveals a wave state around 7 uc of PTO and a vortex state around 10 uc.

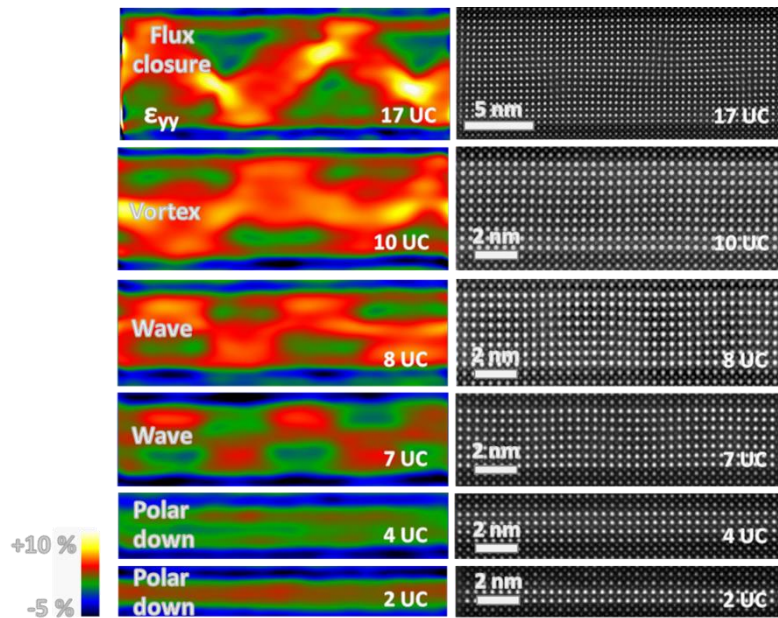


Figure 3.6 Out-of-plane strain (ϵ_{yy}) maps together with the corresponding HAADF images. Pictures on the left are the GPA results extracted from different thicknesses of PTO layers. It is obvious that the different thicknesses of the PTO layers reveals a different intensity and pattern of the out-of-plane strain (color here represents the strength as labeled).

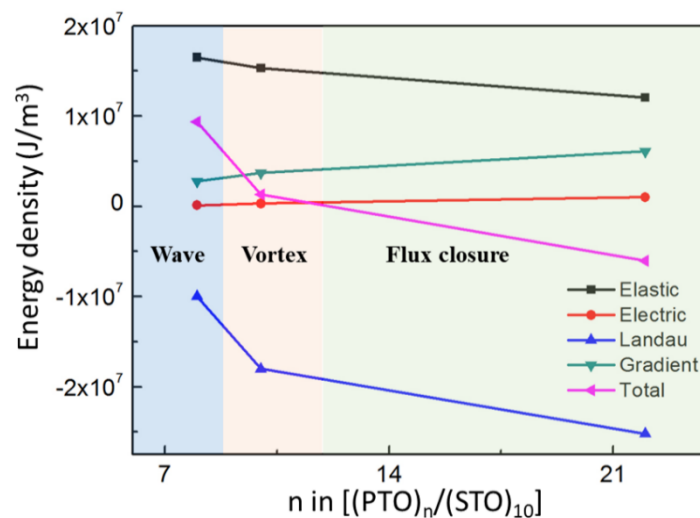


Figure 3.7 The energies for PTO layers as a function of PTO thickness. The evolution of energy components of ferroelectric domain reveal the phase transition sequence with increasing PTO thickness. The decrease of the energy density of system is attributed by the drop of the average elastic and Landau energy density, which is reasonable since the flux-closure has the highest ratio of out-of-plane polarization, followed by the vortex state. Meanwhile, electric and gradient energy density increase owing to the phase transition from the wave-like state, to rotational vortex state smoothly, and to flux-closure state gradually with more distinct domain wall. Furthermore, the relatively analytical mode by Z.H et al.^[77] reveals a similar tendency as experimental results.

3.4 The in-situ study on structural evolution of PTO/STO under external bias

Although the domain evolution can be experimentally realized by changing the layer thickness, modulating the domain pattern in such a way is obviously unpractical toward application. A more practical way of modulating the domain pattern is needed. Therefore, we developed an approach through the application of an external electric field. The electric field driven evolution of the vortex was realized under an applied out-of-plane voltage. A 10-uc-thick PTO layer with a vortex structure is selected to perform the in-situ experiment. A bias of 0 ~5 V was applied and real-time observation under atomic resolution was realized by taking an in-situ non-contact bias technique. As the applied voltage is increased, the arrangement of the vortex cores first reveals a zig-zag state, then transforms into a wave state upon reaching the interface of PTO/STO, and eventually evolves into a polarization down state. Phase-field modeling was performed and the results match well with our in-situ bias experiments (see Fig. 3.8).

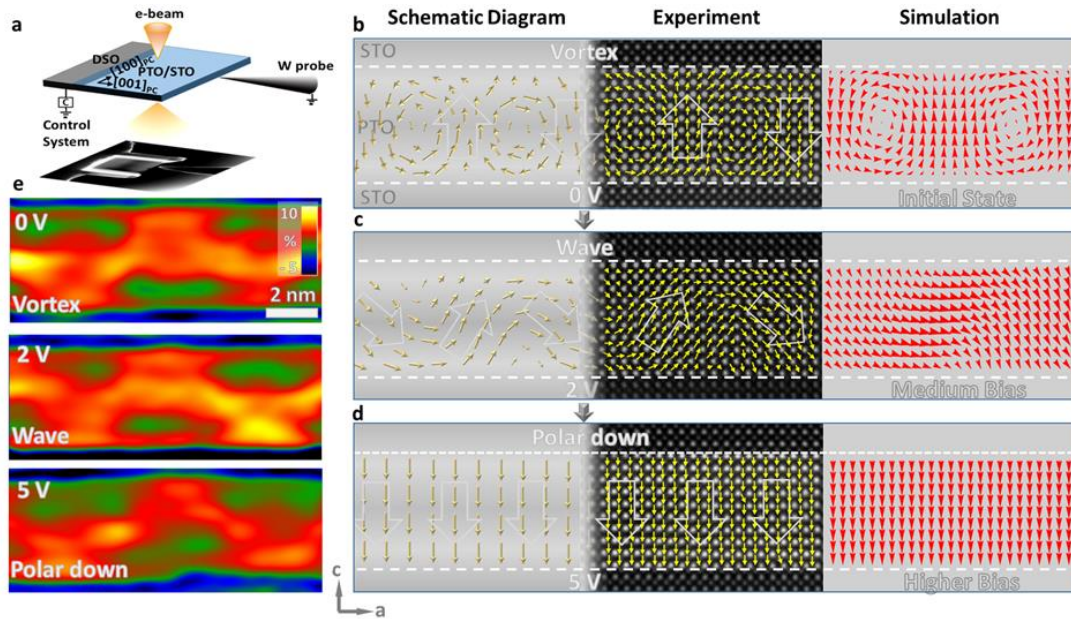


Figure 3.8 Manipulation of the ferroelectric domain in a PTO/STO multilayer under external electric field. a, Schematic diagram of the in-situ electric field experiment. The input voltage is applied along the c -axis. To capture the structural changes, a real-time analysis is performed in STEM mode. b-d, Mapping of the real-time dynamic evolution of the polarization based on HAADF images under an external electric field and the corresponding simulation results. An evolution process of the polar structure from vortex to wave and finally polar down state was recorded. The three columnar sub-panels are schematic diagrams, experimental mappings of polar vector and phase field simulations, respectively. e, The out-of-plane strain (ϵ_{yy}) map of the PTO layer under different external bias, which remain almost unchanged.

An analysis on the time-dependent evolution of the energy components of a ferroelectric domain under different bias was performed (see Fig. 3.9). With applying a mediate electric field, the system prefers a wave-like structure with less out-of-plane polarization, rather than forming a uniformly poled state. Based on phase field calculations, this is driven by a competition among electric, Landau, gradient and elastic energies as it attempts to reach a new equilibrium. With a higher electric field, the evolution driving force is mainly from the large decrease of electric energy, which overcomes the barrier of Landau and elastic energy (see Fig. 3.9).

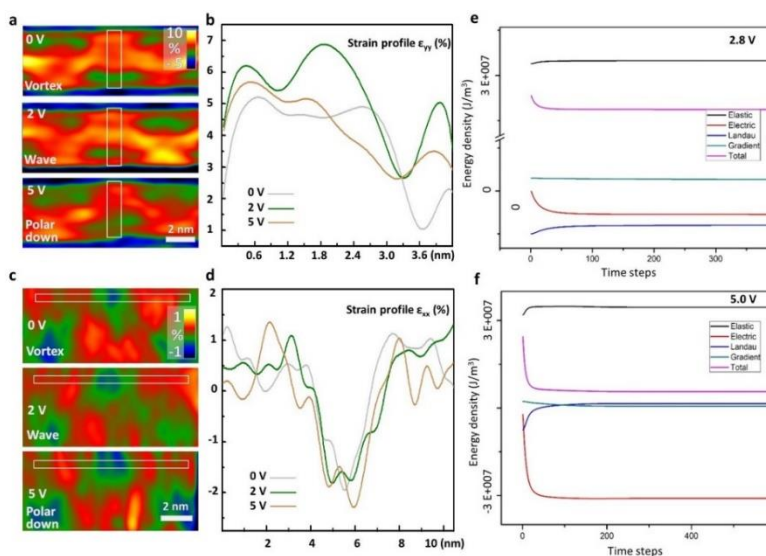


Figure 3.9 Line profiles of strain in a PTO layer and time-dependent evolution of energy components of a ferroelectric domain under different bias. a and c, The out-of-plane (a) and in-plane (c) strain maps of a PTO layer under an external bias of 0, 2 and 5 V. b and d, Corresponding line profiles, extracted from the white boxes in (a) and (c). e, Under a bias of 2.8 V, the reduction of electric energy compensates the increase of Landau and elastic energy, which enhances the polarization toward the external electrical field direction and reduces the polarization opposite to the field. f, Under bias of 5 V, the large external field drives the polarization parallel to the field direction.

The domain evolution in the thickness-changed layer could be attributed to strain as discussed above. While for the topological transformations manipulated by an external electric field, the strain under a bias of 2 V and 5 V remains almost unchanged compared with that in the vortex structure at 0 V (see Fig. 3.8 and details in Fig. 3.9): the out-of-plane strain in the wave structure at 2 V is slightly larger than that in the vortex structure at 0 V (an average 5.1% out-of-plane strain at 2 V, compared with an average 4.0% out-of-plane strain at 0 V), with their pattern unchanged. For the in-plane strain, both the strain pattern and strength remain almost unchanged. These results imply that other factors, besides the strain, such as charge might play a more important role during the transformations under electric bias. Exploring the electronic structure is therefore meaningful.

3.5 Exploring the electronic structure of topological configurations

To explore the electronic structure within these domain configurations, atomic scale STEM-EELS mapping was performed (see Fig. 3.10). This is based on a common method, using the valence change of the cations to evaluate the type and relative density of the charge^[130, 131] or reveal the electron accumulation^[132]. We acquired 2D core loss spectral images from a PTO layer with vortex structure. Using model-based quantification of the EELS spectra^[133], the relative concentrations of Ti^{4+} and Ti^{3+} were estimated and a clear hint of electron concentration at the core of vortex was found (the concentrated areas of Ti^{3+} are shown in Fig. 3.10c). According to the model-based quantification, the average Ti^{3+} fraction in a typical core-region is calculated to be ~ 0.19 . As a cross-check of the model based quantification of the Ti valence, we further measured the t_{2g} - e_g splitting of Ti-L_{2,3} (Fig.3.10b and 3.10d). According to literatures^[134-137], the splitting between t_{2g} and e_g can be used to measure the proportion of the Ti^{4+} and Ti^{3+} components. A typical Ti^{3+} EELS spectrum of Ti_2O_3 has two peaks of L₃ and L₂ edges^[23] while there are four peaks for the Ti^{4+} spectrum^[138]; correspondingly a narrow split stands for a larger proportion of the Ti^{3+} component^[23, 138, 139]. On the basis of our measurements, the energy splitting of the L₃ and L₂ edge at the vortex core is found to be lower than that in other regions of the PTO layer, as shown in Fig. 3.10d. Moreover, when comparing the octahedral deformations (*e.g.* octahedral elongation/tilt) in the vortex core and in non-core regions, no significant difference was observed (Fig. 3.11), indicating that octahedral deformation is not the main reason of such huge t_{2g} - e_g splitting change at the core of the vortex. Based on these experimental evidences, the possibility of a vortex core containing a higher Ti^{3+} concentration is reasonably proposed.

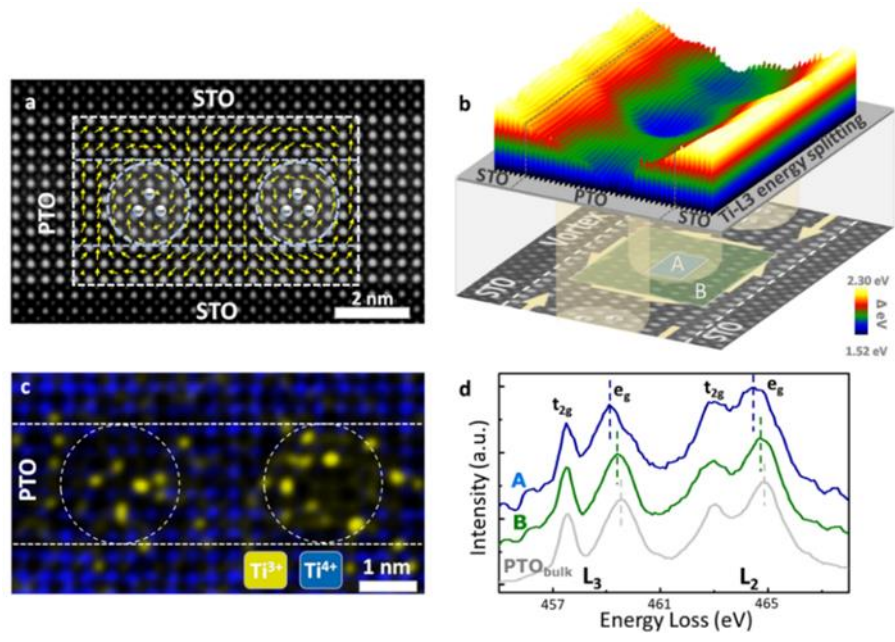
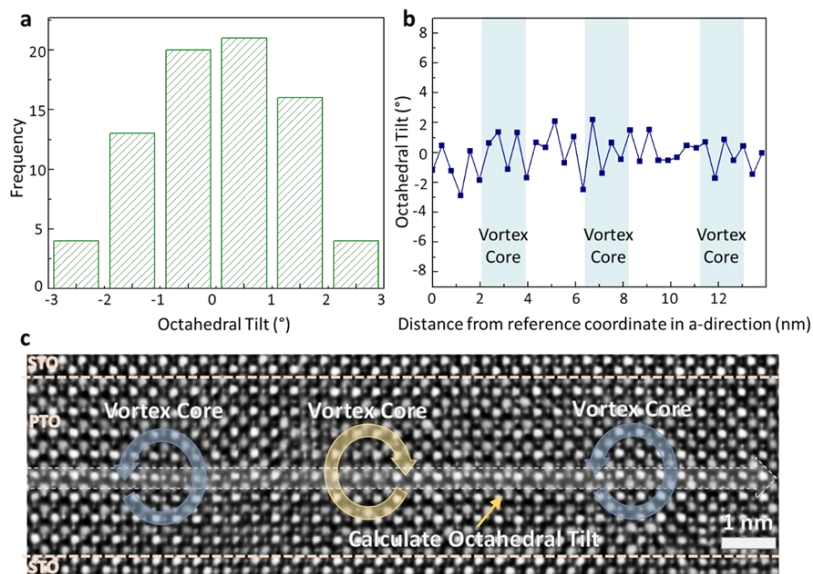
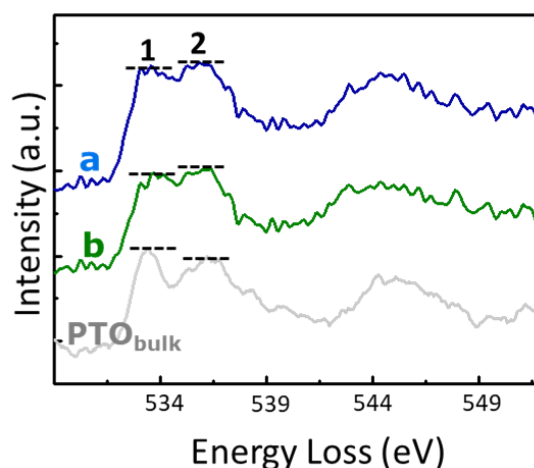


Figure 3.10 EELS-mapping results in $\text{PTO}_{(11)}/\text{STO}_{(10)}$ where vortex domains exist. a,

HAADF image of a PTO layer of 11 uc with vortex domains, together with its polar map. Dashed circles represent the concentrated areas of negative charge. b, The upper colored surface plot shows the Ti-L_3 energy splitting in the PTO layer where a vortex exists, the lower HAADF image shows the location of the corresponding vortex structure in the PTO layer. c, Superposition of the Ti^{4+} and Ti^{3+} signal based on EELS analysis; the investigated area is extracted from the dashed box area in a. d, $\text{Ti-L}_{2,3}$ spectra corresponding to three areas: the blue-A curve is from the vortex core, the green-B curve is from the PTO layer but away from the vortex cores, and the grey curve is the reference $\text{Ti-L}_{2,3}$ spectrum acquired in the bulk-PTO.

Figure 3.11 Analysis of the oxygen octahedral tilt based on iDPC images. a, Statistical results of the oxygen octahedral tilt angle. b, Distribution of the octahedral tilt across the vortex core region. c, the iDPC-STEM image used to calculate the octahedral tilt. From the statistical results, tilt angles were found to be below 1.5° in most unit cells of the PTO layer,



which is significantly lower than the angle which is assumed to induce significant changes in electronic structure^[74].

Figure 3.12 EELS results of O-K edges in the vortex layer. The grey curve: reference O-K spectra acquired in the bulk-PTO; the blue a-curve was acquired in the vortex core as shown in Fig. 3.10; the green-b curve was acquired around the vortex cores. The peak located at ~537 eV (marked as peak 2) in the O K edge is closely related to the bonding state between oxygen and the surrounding cations^[140]. The grey spectrum exhibits a slightly lower peak 2 compared with the peak located at ~533 eV (marked as peak 1), in agreement with the calculated results of PTO without oxygen vacancies^[141]. Differently, the blue and green spectrum exhibits an obviously enhanced peak 2, comparable to peak 1, providing evidence for the appearance of oxygen vacancies at the core-region and nearby.

An indication of oxygen vacancies at the core of vortex and nearby region was also observed (Fig. 3.12). The presence of oxygen vacancies can provide electrons, which supports our findings of Ti^{3+} . A charge accumulation leading to valence changing has been found in many ferroelectric system. For example, the head to head charged domain wall in BFO, where electrons accumulate, is n-type conductive and associated with the presence of Fe valence dropping. Similar features were found in our case, the concentration of electrons may partially occupy Ti 3d states leading to a valence change from Ti^{4+} to Ti^{3+} at the ferroelectric vortex cores. We therefore reasonably expected a concentration of electrons leading to an enhanced electric conductivity at the ferroelectric vortex cores; a similar phenomenon was reported in BiFeO_3 ^[74].

To unambiguously demonstrate the correspondence between vortex core and Ti^{3+} component distribution, we analyzed those PTO layers in which the core of the vortex reveals a zig-zag state. The 2D core loss spectra shows that the distribution of Ti^{3+} also reveals a zig-zag pattern (see Fig. 3.13). This correspondence between core and Ti^{3+} can also be found in the polar wave structure: the Ti^{3+} concentrated regions are found to locate

at the opening of the wave domain. As a result, the e_g and t_{2g} energy splitting of $Ti-L_3$ shows a clear decrease at these regions (see Fig. 3.14a and 3.14b).

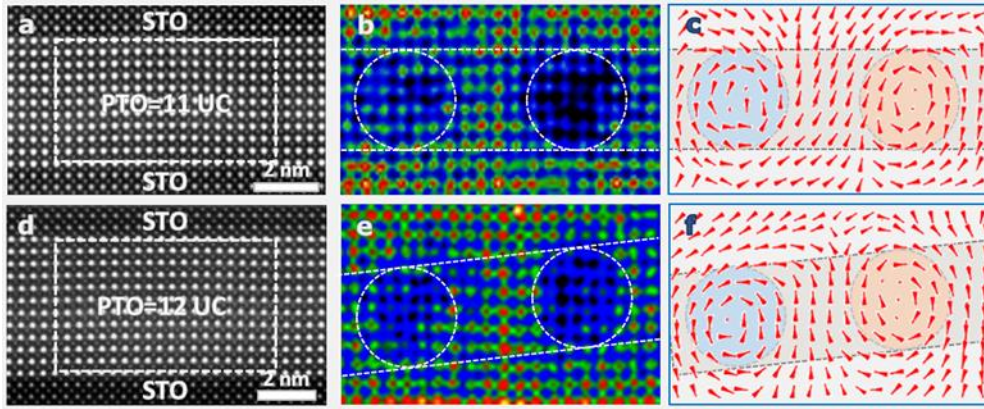
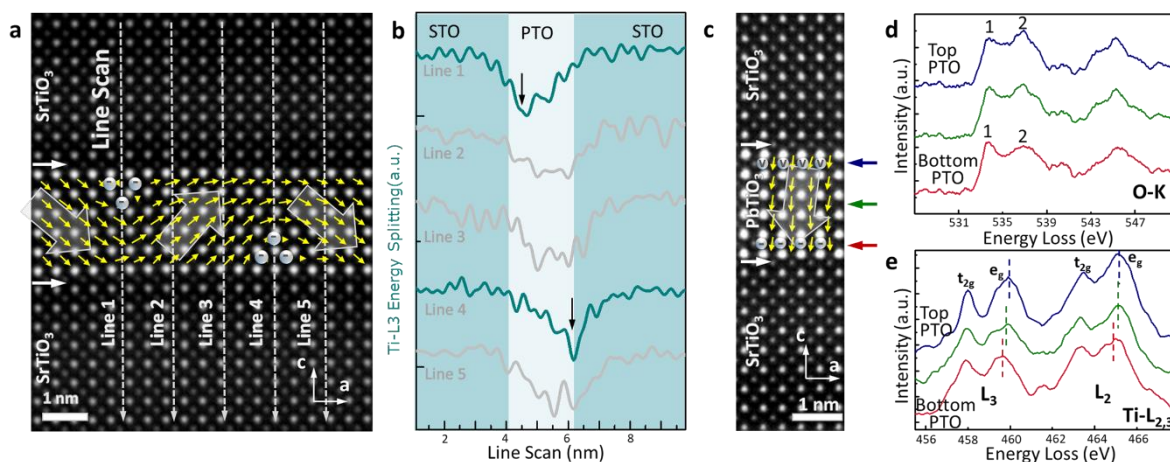


Figure 3.13 EELS-mapping results in $PTO_{(11/12)}/STO_{(10)}$ where vortex domains exist. a and d, HAADF images with the investigated areas indicated. b-c and e-f are extracted from the dashed box area in (a) and (d). b and e, Ti^{4+} signal extracted from the EELS spectrum. Dashed circles represent the concentrated areas of electrons. c and f, The corresponding polar vector map. It's obvious that the location of the vortex core atomically matches with the polar map.

The close relationship between domain and Ti^{3+} component distribution was also found in the out-of-plane polarization region. There are some out-of-plane polarization regions which usually exist in a/c domains and some wave structures (for example, the wave domain shown in Fig. 3.5e). According to a previous study, for a single-domain ferroelectric perovskite oxide, a high concentration of electrons (with bulk density of the order of $\sim 10^{20} \text{ cm}^{-3}$)^[142] or oxygen vacancies accumulated near the polar surface is needed for screening. EELS investigations show that oxygen vacancies are accumulated at the negative polar interface^[141] as shown in Fig.3.14c-d. Moreover, a closer $Ti t_{2g}-e_g$ split was found as shown in Fig. 3.14e, indicating the existence of Ti^{3+} near the positive polar interface, and a continuous increase of the Ti^{3+}/Ti^{4+} ratio across the out-of-plane polarization region, obtained by model-based quantification of the EELS spectra, also shows good agreement with energy splitting analysis (see Fig. 3.15). These experimental evidences above point toward the idea that the polarization screening within the

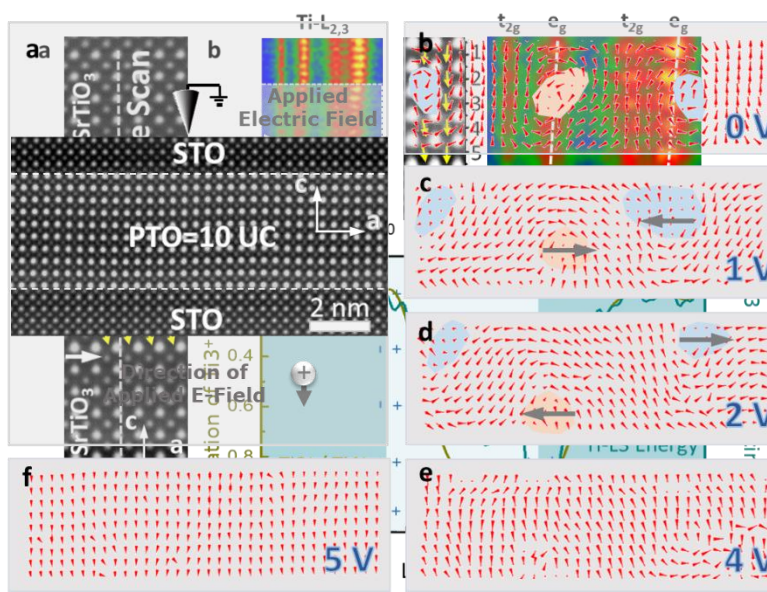
out-of-plane polarization regions is realized by the existence of oxygen vacancies on the negative polar interface and the accumulation of electrons on the positive polar interface.



This is consistent with the screening mechanism which has been well established in similar ferroelectric materials^[143, 144].

Figure 3.14 HAADF-STEM images and EELS characterization across the multilayer. a, HAADF-STEM image of PTO₍₆₎/STO₍₁₀₎. The yellow arrows indicate the polarization direction. Line scan EELS were performed across different regions of the wave domain. b, Energy splitting value in the PTO and STO layers across the corresponding regions in (a), showing that the Ti³⁺ component is constrained in the wave opening. c-e, HAADF-STEM image of the polar down region and corresponding EELS results of Ti-L_{2,3} and O-K edges across the PTO layer. The blue, green and red curve are acquired at the regions indicated by arrows in (c).

Figure 3.15 EELS results in out-of-plane polarization region. a, HAADF-STEM image of PTO₍₈₎/STO₍₁₀₎. A line scan EELS was performed across a polar down region. b,



Atomic-scale resolution Ti-L_{2,3} spectra across the PTO/STO multilayer. The HAADF image is extracted from the polar down region in (a). Connecting the centers of the Ti-e_g peak, a distinct tilt line is observed, which means a narrowing of the energy splitting. c, Energy splitting value as well as Ti³⁺/Ti⁴⁺ ratio in the PTO and STO layers across the multilayer, which is obtained by model-based quantification of the EELS spectra and shows good agreement with the results of the Ti-L₃ energy splitting, these results indicate that the electrons is rich at the positive polar interface. The light grey area indicates the PTO layer.

Figure 3.16 Complete evolution process with applied in-situ bias. a and b, Schematic diagrams of the in-situ bias experiment and the initial state. c, Upon applying an increased voltage, the position of the vortex core reveals a zig-zag state, and then the vortex core starts to move toward the interface and they become close to each other. d, With higher bias, the vortex cores move away from each other. e and f, Finally it becomes a polarization down state.

3.6 Conclusions

Previous researches have studied various topological structures, and their corresponding strain mappings differ from one another in terms of magnitude and pattern. However, in our in-situ real-time atomic observation on topological transformation under external electric field, a dynamic rotational switching process is observed, which is very similar to theoretical predictions^[145] but with no distinct variation on the strain. Also, note that the motion process of the vortex cores under electric field (see Fig. 3.16) generally matches previous theoretical results^[76]. Specifically, the two vortex lines first move toward each other to reduce the area with opposite polarization directions. However, instead of “melting”^[76], the vortex lines move away from each other again under a higher bias.

We analyzed a series of atomic EELS mappings on different polar structures; the presence of Ti³⁺ and oxygen vacancies provides a cross-check that shows a high correlation with the various topological structures. These experimental evidences allow us to propose the possibility of an one-to-one correlation between the charge and various domain

configurations in this oxide multilayer. Our findings support that in the out-of-plane polarization layer, the electrons concentrated at the positive polar interface may be attributed to the polar screening. While in the vortex, zig-zag vortex state, and the polar wave structure, where polar screening is not needed, other factors such as the gradient of the electric field or the local pressure may make a contribution. An analogous phenomenon was found and explained in the field of optical vortices^[146, 147]: optical tweezers are able to trap and manipulate small particles, typically of micron size. Another possible origination is that the formation of oxygen vacancies at the vortex cores would attract electrons. The local pressure at the vortex cores is negative, thus oxygen vacancies are favored to distribute near the core-region, because oxygen vacancies have larger atomic volume than oxygen atoms. However, a full and in-depth understanding of the underlying mechanism still requires further research.,

In summary, we successfully developed an in-situ non-contact bias technique approach to modulate topological polar structures, and for the first time, we demonstrate a straightforward view of a real-time atomistic evolution process in topological transformations. The EELS analyses explored the accompanying changes in electronic structure. Our experimental data clearly suggest a meaningful method to induce transformations among various ferroelectric domains, providing new insights into the formation and stability of various domain structures.

Chapter 4 The exploration on irreducible ferrielectric materials

In solids, charge polarity can one-to-one correspond to spin polarity phenomenologically, e.g. ferroelectricity and ferromagnetism, antiferroelectricity and antiferromagnetism, even dipole-vortex and magnetic-vortex, but ferrielectricity and ferrimagnetism kept telling a disparate story in microscopic level. Since the definition of a charge dipole involves more than one ion, there may be multiple choices for a dipole unit, which makes most ferrielectric orders equivalent to ferroelectric ones, i.e. this ferrielectricity is not necessary to be a real independent branch of polarity. In this chapter, by using the spherical aberration-corrected scanning transmission electron microscope, we visualize a nontrivial ferrielectric structural evolution in BaFe_2Se_3 , in which the development of two polar sub-lattices is out-of-sync, for which we term it as irreducible ferrielectricity. Such irreducible ferrielectricity leads to a non-monotonic behavior for the temperature-dependent polarization, and even a compensation point in the ordered state. Our finding unambiguously distinguishes ferrielectrics from ferroelectrics in solids.

4.1 Introduction

Ferrielectricity, the equivalent of ferrimagnetism, can be termed as antiferroelectric order but with a switchable polarization, as sketched in Fig. 4.1a. The first proposed ferrielectric system was a composition of two antiferroelectric compounds NaVO_3 and NaNbO_3 ^[83, 84], but subsequent experiments did not support this claim^[84]. Despite a long history, the existence of ferrielectricity in solid crystals remains rare, except in liquid crystals^[85]. Recently, some solids were claimed to be ferrielectric. For example, in the layered-structure CuInP_2S_6 , the positions of Cu and In are always opposite within each unit cell (u.c.), which can be recognized as two uncompensated polar sub-lattices with antiparallel alignment^[86, 87]. In geometric ferroelectrics, such as $\text{Ca}_3\text{Ti}_2\text{O}_7$ and some perovskite superlattices, the displacements of ions are opposite between layers, which can also be recognized as two uncompensated dipole moments^[88, 148]. Despite the macroscopic and phenomenological analogy as shown in Fig. 4.1a, it should be noted that there is a key difference between the ferrimagnetic and ferrielectric systems in the

microscopic level. Different from the spin moment which can be defined on a single ion, the definition of a charge dipole involves more than one ion and thus may have multiple choices in ionic crystals. By choosing different ions as a dipole unit, multiple dipole values for a sub-lattice can be obtained^[149]. In this sense, the Cu-In pair in CuInP_2S_6 or bilayer in $\text{Ca}_3\text{Ti}_2\text{O}_7$ can be treated as a dipole unit, which are indeed entangled simultaneously^[86, 88]. Therefore, these systems are indistinguishable from ferroelectrics, i.e. “reducible” ferrielectrics, as qualitatively sketched in Fig. 4.1a. Indeed, CuInP_2S_6 only shows one paraelectric-ferroelectric transition temperature, and in most cases those geometric ferroelectrics are coined as “ferroelectrics” rather than “ferrielectrics”^[87, 150]. Similar situations also exist for other ferrielectrics like Pb_2MnWO_6 ^[90]. Conceptually different to these “reducible” ferrielectrics, in this chapter, we provide proof of an “irreducible” ferrielectricity (see Fig. 4.1 for its conceptual definition of “irreducible” ferrielectricity) in BaFe_2Se_3 . We will show unique ferri-characteristics clearly distinguishable from ferroelectricity.

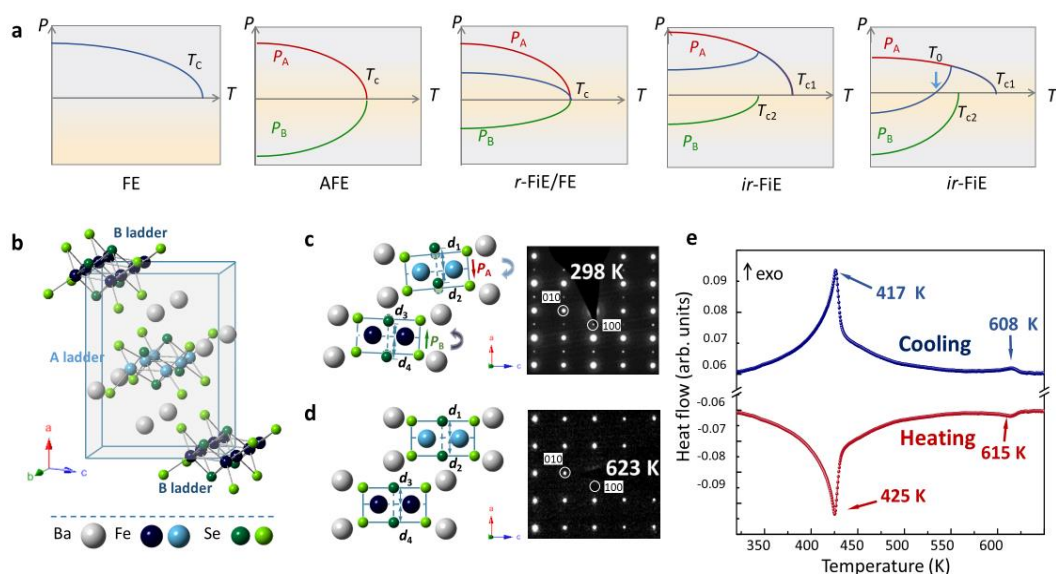


Figure 4.1 Concept of ferrielectricity and candidate material BaFe_2Se_3 . a, Polarization (P) vs temperature (T) of ferroelectricity (FE), antiferroelectricity (AFE), reducible-ferrielectricity (r -FiE) and irreducible-ferrielectricity (ir -FiE), respectively. In r -FiE, two polar sub-lattices (A & B) develop synchronously, with one unique critical temperature. This type of ferrielectricity is macroscopically equivalent to ferroelectricity. In ir -FiE, the evolution of sub-lattices A & B is out-of-sync, with two critical temperatures (a higher T_{C1} & a lower T_{C2}). A compensation point (T_0) may appear in some ir -FiE systems. Note that any information on

the order of the phase transition is not represented in these qualitative cartoons. b, Crystal structure of BaFe_2Se_3 . Each unit is composed of two iron-ladders. c, Room temperature structure with a tiny tilting angle between the ladders A and B. d, High temperature structure without tilting. The in-situ selected area electron diffraction patterns are shown. The lattice periodicity along the $[100]$ direction changes from 11.90 \AA to 5.96 \AA as the temperature rises from 298 K to 623 K . e, DSC curves indicate two transitions at $\sim 610 \text{ K}$ and $\sim 420 \text{ K}$. The $\sim 610 \text{ K}$ transition is a second-order one with a step-like behavior, while the $\sim 420 \text{ K}$ transition is a first-order one with a peak.

4.2 Technique detail

4.2.1 Sample preparation

High-quality BaFe_2Se_3 single crystals were grown by the self-flux technique starting from an intimate mixture of Ba pieces, Fe granules, and Se powders with an atomic ratio of 1 : 2 : 3. Then the starting materials were put in a carbon crucible and sealed in the quartz tube with partial pressure of argon. The quartz tube was first heated to 420°C at a rate of $1^\circ\text{C}/\text{min}$, held for 12 h, and then annealed at 1150°C for another 24 h. After that, the quartz tube was slowly cooled down to 750°C at a rate of $3^\circ\text{C}/\text{h}$. Finally, the quartz tube was cooled down to room temperature naturally and the strip-like BaFe_2Se_3 single crystals with a typical size of $3.0 \times 1.0 \times 0.5 \text{ mm}^3$ and shiny surfaces can be obtained.

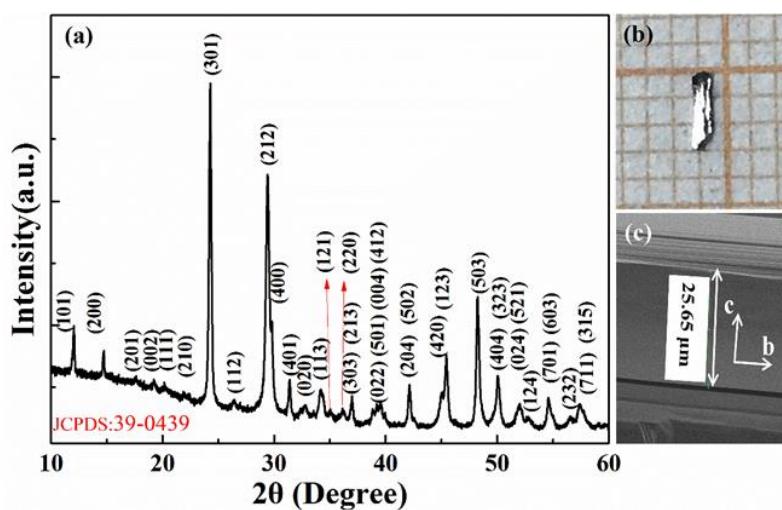


Figure 4.2 a, X-ray Powder diffraction of BaFe_2Se_3 . Optical (b) and SEM (c) microscopy on BaFe_2Se_3 fiber show that the extension direction is actually along b -axis, thus the direction of

Fe chains. Each piece of our sample (of mm size) is consisted of many loosely-contacted tiny needle-like crystals. For these crystals, the needle direction is along the *b*-axis, while the typical scale of crystals along *a*- or *c*-axis is only of μm size. Only relative large (still very small) *bc* cleavage surface is available, and it does not imply a whole single crystalline below the surface. Twin crystals are very possible below the cleavage surface, considering the edge with chipped steps besides the very small cleavage surface.

4.2.2 Macroscopic properties measurements

Differential scanning calorimetry (DSC) experiments were performed with Maia DSC 200 F3. Measurements were performed on heating and cooling with a rate of $10 \text{ K}\cdot\text{min}^{-1}$. The sample is encapsulated in a standard Al crucible using argon stream as the protecting gas. XRD measurements were performed on Rigaku Smartlab3 with Cu K_{α} radiation. In the SHG measurements, the incident laser with a wave length of 800 nm is perpendicular to the cleavage (100) plane and the reflected light at 400 nm is collected. The polarization of the incident laser is controlled by a half wavelength plate. Then the canting polarization along the *c*-axis can be monitored, which is in proportional to the main component of polarization along the *a*-axis. The SHG signal was measured with the polarization of the incident laser (i.e. the electric field component E) in the *bc* cleavage surface of the BaFe_2Se_3 crystal, while the angular-dependent results with rotating E is also provided. Magnetic measurements were carried out in a vibrating sample magnetometer (VSM) integrated in a Physical Property Measurement System (PPMS-9, Quantum Design) up to 600 K. Neutron Powder Diffraction (NPD) data were collected on a High-intensity Powder Diffractometer Wombat at Australian Nuclear Science and Technology Organization (ANSTO) with $\lambda=2.41 \text{ \AA}$, between 10 K and 500 K. Resistivity was measured using Keithley 4200A-5CS.

4.2.3 In-situ study and specimen transferred to chips

The in-situ heating experiment was done on DENS solutions SH30 system in order to carry out the experiment in a wide temperature range. The Nano-Chip we used could control the temperature environment locally on the device via the 4-point-probe. Its highest temperature accuracy and stability is $0.001 \text{ }^{\circ}\text{C}$. The experimental data at low temperature was

obtained by a demo low-temperature sample holder made by DENS. The in-situ biasing was done on Hysitron PI-95 TEM PicoIndenter, the input voltage $V_{DC}=5$ V was applied between the sharp conductive tip and the sample using a function generator. To capture the changing of atoms positions, the real-time crystal structure is characterized in STEM. The atomic-scale spatial resolution of STEM and the access to structural information provide a clear picture of the evolution under external electric field.

To measure the performance of $BaFe_2Se_3$, as shown in Fig. 4.3. After conventional FIB process of welding the lamella onto needle and transfer it near the surface of chips, additional confined Pt pad was deposited to contact the lamella onto the chip surface. The lamella thickness was to about 2 μm . Low current down to 10 pA was used to polish the surface of chips after detaching the needle to reduce the amount of redeposited material resulting from the previous contacting process.

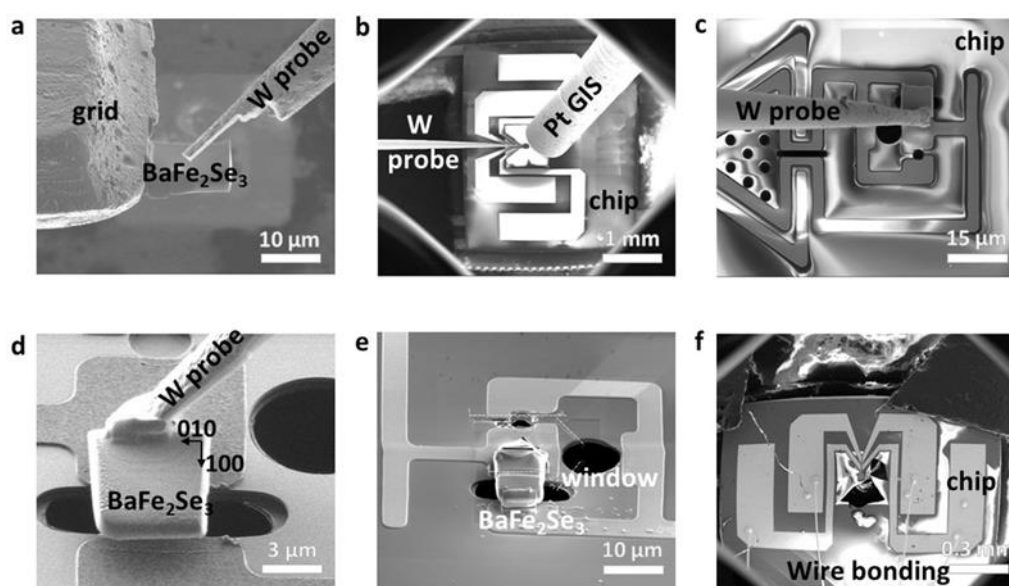


Figure 4.3 The SEM images showing the technique using a probe in order to put the sample onto a chip for testing the macroscopic properties tests. Some tests including the ferroelectric measurements along the a -axis and its behavior with temperature are done on these micro devices. (a) Welding the sample to tungsten probe (marked as W probe) and cutting the sample from the grid. (b) Transfer of the sample to the four-probe electricity chip and welding it onto the chip by Pt GIS. (c) Enlarged view of the end region of the chip. We place

the chip on the window between electrodes which act as heat conductor or electric conductor. (d) Magnified image of the end region. (e) Polishing the surrounding area of the lamella by a Ga ions beam. (f) Connecting useful electrodes to external equipment by wire-bonding.

4.2.4 DFT calculation

The DFT calculation was performed based on the projector augmented-wave (PAW) potentials and Perdew-Burke-Ernzerhof exchange function as implemented in Vienna *ab initio* simulation package (VASP) ^[151]. The plane-wave energy was 500 eV. The experimental structures at different temperatures were used and the Cx-type antiferromagnetism is adopted for simplify (since here the polarization is not driven by magnetism). Brillouin zone integration was obtained using a $6 \times 3 \times 4$ k -point mesh. The standard Berry phase method is adopted to estimate the ferroelectric polarization ^[152], while the intuitive point-charge-model provides similar results.

About Landau-Ginzburg-Devonshire model: To fit the experimental phase transitions, $T_A=610$ K & $T_B=420$ K, are used. Noting $T_{C1}=T_A$ for the second order phase transition, and T_{C2} is close but slightly higher than T_B for the first order transition. To simulate Fig. 4.10e, $\alpha_1=1$ as the unit, and $\beta_1=5$, $\alpha_2=4.5$, $\beta_2=-5$, $\gamma_1=\gamma_2=40$. The negative β_2 is essential for the first-order transition around T_{C2} and the differences between α_1/α_2 , β_1/β_2 originate from the charge disproportion. α_{12} can be a small quantity, e.g. 0.001.

4.3 The Structural characterization and research of charge distribution on BaFe_2Se_3

BaFe_2Se_3 belongs to the iron-based superconductor family ^[91, 92, 153] but predicted to be multiferroic under ambient conditions ^[93]. As shown in Fig. 4.1, a BaFe_2Se_3 u.c. contains two iron ladders (labelled as A and B). Long-range block-type antiferromagnetism (block-AFM) appears below the Néel temperature $T_N \sim 240\text{-}256$ K ^[154-158]. The structural tetramerization due to the block-AFM leads to charge dipoles along the a -axis and the alignment of dipoles is almost antiparallel but with a tiny canting angle ($\sim 5.78^\circ$ at room temperature) between ladders A and B (schematic displacements are shown in Fig. 4.1c) ^[93]. It should be noted that all other

members of the 123-series iron selenides (e.g. BaFe_2S_3) also own a similar (quasi-) one-dimensional (1D) ladder structure, but only BaFe_2Se_3 has the canting ladder characteristic. According to theory^[93], a residual polarization along the c -axis (P_c) is expected in BaFe_2Se_3 , as a characteristic of a “reducible” ferrielectric material.

The tilting of the iron ladders gradually disappears with increasing temperature up to ~ 600 K, leading to a high symmetric $Bbmm$ phase, according to X-ray diffraction^[155]. Our in-situ selected area electron diffraction (SAED) results give distinctive patterns (Fig. 4.1c vs Fig. 4.1d), confirming the disappearance of the ladder canting at high temperature. Differential Scanning Calorimetry (DSC) measurements (Fig. 4.1e) confirm the phase transition occurring at ~ 610 K as a second-order one. Besides, there is a first-order phase transition at ~ 420 K, which was also evidenced in previous report but its real origin remains a puzzle. In addition, the resistivity behavior also supports this first-order transition (Fig.4.4). Since our neutron powder diffraction (NPD) data confirm that only one block-AFM transition appears at 250 K, obviously, the transition at ~ 420 K can be excluded as a magnetic-ordering behavior (Fig. 4.5).

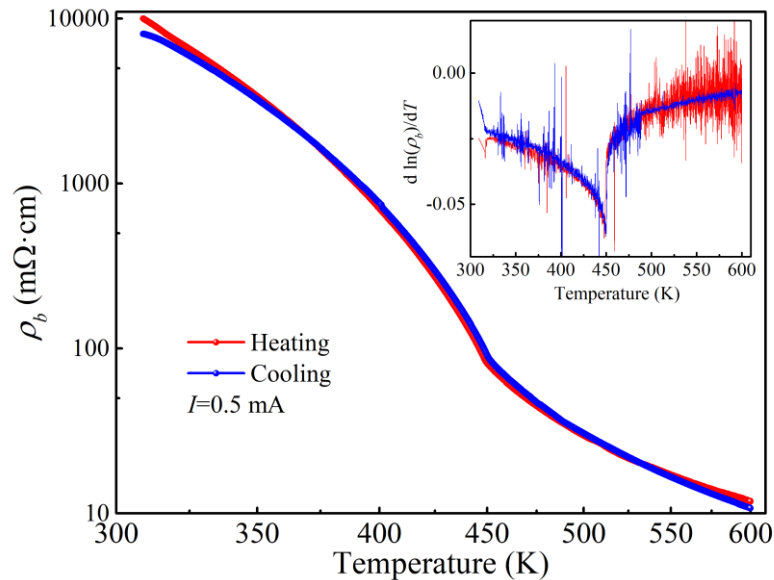


Figure 4.4 Temperature dependence of the resistivity (ρ_b). Insert: the derivative of $\ln(\rho_b)$. The resistivity changes its behavior near 450 K, which also supports the scenario of a first-order transition. The measuring current is along the b -axis. Noting this material is highly conductive (although it is not a metal) with a very small experimental band gap (e.g. 0.178

eV or 0.13 eV)^[156, 157], it is technically challenging to directly measure its small polarization ($\sim 0.1 \mu\text{C}/\text{cm}^2$) hysteresis loop, i.e. to demonstrate the switching of polarization. Noting that the anomaly of resistivity occurs at a little higher temperature than T_{C2} of DSC ($\sim 417\text{-}425 \text{ K}$) for the following possible reasons. First, usually thermometers for different experiments are not well relatively-calibrated, especially for the high-temperature range. Second, maybe for such a first order transition, resistivity always changes at a little higher temperature, according to the previous SHG result^[159].

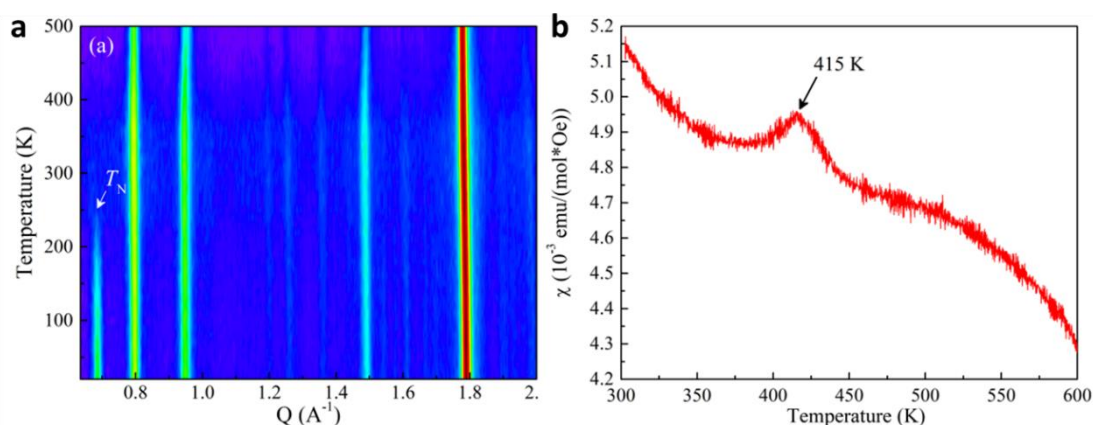


Figure 4.5 Macroscopic physical properties. (a) Contour plot of the neutron powder diffraction spectrum, collected on the high-intensity powder diffractometer WOMBAT at the Australian Nuclear Science and Technology Organisation (ANSTO) with $\lambda = 2.41 \text{ \AA}$, between 10 K and 500 K. The magnetic peak at $Q = 0.7 \text{ \AA}^{-1}$ for block-type antiferromagnetism appears below $\sim 250 \text{ K}$, in agreement with literature. No other long-range magnetic order is observed in the whole spectrum from $Q = 0.63\text{-}4.75 \text{ \AA}^{-1}$. (b) Magnetic susceptibility peaked at $\sim 415 \text{ K}$, measured under 1 T field. Neutron powder diffraction confirms the appearance of long range magnetic ordering below $\sim 250 \text{ K}$, in agreement with previous report of ($\sim 255 \text{ K}$)^[156, 157] and ($\sim 256 \text{ K}$)^[154]. Thus, the peak of the magnetic susceptibility at $\sim 415 \text{ K}$ (appearing only under strong magnetic field, e.g. $\sim 1 \text{ T}$) should be a side effect of a polar structural transition, instead of a magnetic phase transition.

Using a spherical aberration-corrected scanning transmission electron microscope (Cs-STEM), we were able to determine the subtle structure evolution of the 1D Fe chains as well as the associated Se's. Then the structure of BaFe_2Se_3 can be directly measured atom column by atom column, which reveals an unexpected irreducible ferrielectricity going beyond

the theoretical expectations. The STEM image of BaFe_2Se_3 along b -axis and c -axis was shown in Fig. 4.6. The STEM results at room temperature are summarized in Fig. 4.7.

Interestingly the structural tetramerization already exists at room temperature and, unexpectedly, the intensities for ladders A and B are not equivalent, creating a strong ladder and a weak ladder within a unit cell. The inequivalent features in strong ladders and weak ladders are embodied in magnitude of displacements, as shown schematically in Fig. 4.7a and in the high-angle annular dark-field scanning transmission electron microscopy (HAADF-STEM) images along the b (Fig. 4.7b) and c axis (Fig. 4.7c). The line profiles along these two ladders are shown in Fig. 4.8. A displacement vector-mapping algorithm was implemented on the cross-sectional HAADF-STEM images to measure the local displacement of the atoms. Based on the statistics of about 300 data for each length, the Fe atoms displacement in the strong ladders are stronger than that in the weak ladders (see Fig. 4.8 for an example). Considering that the Fe-block tetramerization could induce Se ions displacement along the a -axis^[93] (as clearly indicated in Fig. 4.7b and 4.7d), such inequivalence of Fe displacements will lead to a residual polarization along the a -axis (P_a), which is larger than the expected P_c . The arrow is added to make it more visible. The uncovered zoom-in images (raw data) have been shown in Fig. 4.7(b-c). Therefore, BaFe_2Se_3 is a room temperature ferroelectric with polarization mainly along the a -axis, rather than the expected low temperature ferroelectric with polarization along the c -axis^[93].

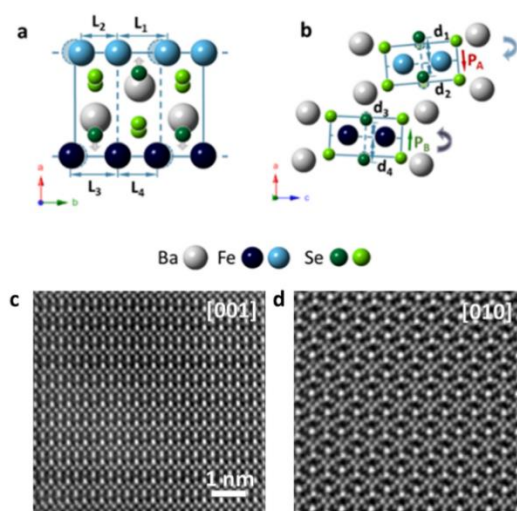


Figure 4.6 STEM images and sketches of BaFe_2Se_3 along (a) and (c) the $[001]$ direction, (b)

and (d) [010] direction. BaFe_2Se_3 , having an orthorhombic crystal structure, was analyzed with different temperature and external bias. Samples were cut into lamellas with the widest faces perpendicular to the crystal principal axis ([010] and [001]) by Focused Ion Beam for the observation in the electron microscope. Since the BaFe_2Se_3 is easily dissociated along the [100] plane which could be observed easily, it is convenient to judge orientation and perform further analysis of the accurate crystal structure on the basis of HAADF images along a target direction.

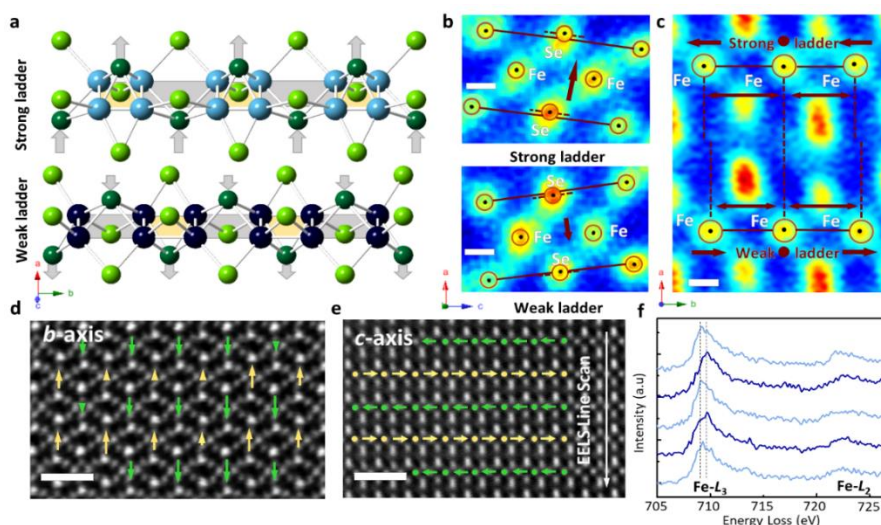
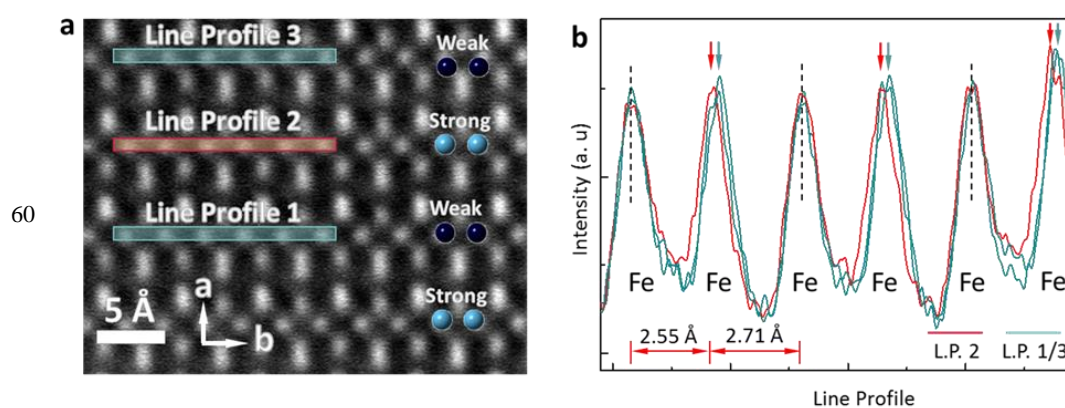


Figure 4.7 Atomic displacements in the ladders. a, Schematic displacements of Fe and Se ions indicated by arrows and amplified in magnitude. Light blue: strong ladder with larger polar bias of Se ions; Dark blue: weak ladder. b and c, Color-enhanced HAADF-STEM images of BaFe_2Se_3 along b -axis and c -axis. The strong and weak ladders are distributed in an alternating order. d and e, Superposition of the HAADF image and the polar map of Se atoms along b -axis and Fe atoms along c -axis. The yellow and green arrows there represent the atoms displacements in strong and weak ladders respectively. f, The EELS line scan is across the white line in (e). EELS measurements indicate the charge ordering pattern. The averaged Fe $L_{2,3}$ edge spectrum from neighboring Fe chains is presented. A Fe- L_3 peak shift of approximately 0.4 eV between neighboring Fe chain is observed.



60

Figure 4.8 STEM image of BaFe_2Se_3 along the c -axis and corresponding line profiles. (a) HAADF-STEM images along the c -axis. (b) Corresponding line profiles which are extracted from the red and cyan boxes in (a), which represent weak and strong ladders respectively. The difference between the bond length of strong and weak ladders is clearly observed.

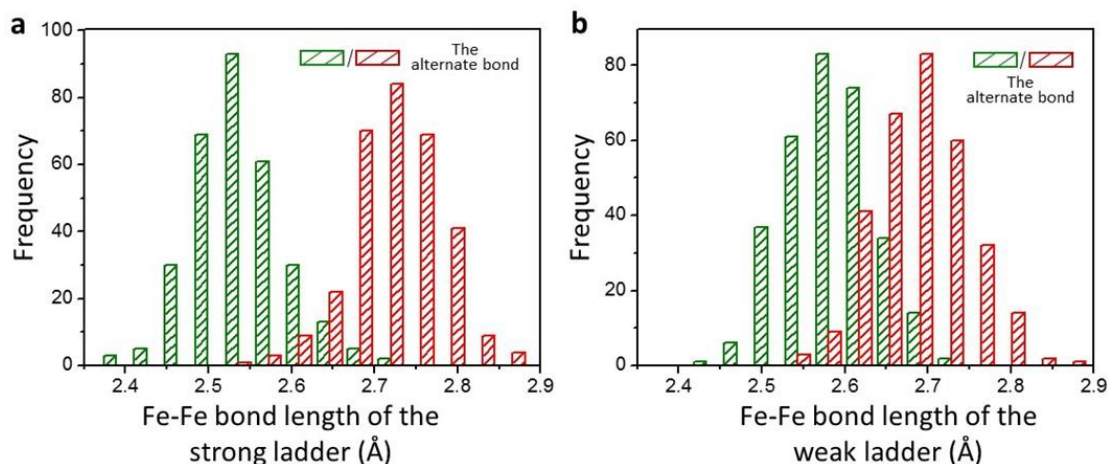


Figure 4.9 Measurement of the displacements. Based on the statistics of about 300 data, Fe-Fe bond lengths of the (a) strong ladder and (b) weak ladder are shown. According to the most probable values of distributions, the alternate Fe-Fe bond lengths in strong ladders are 2.55 ± 0.04 Å and 2.71 ± 0.04 Å respectively, in which the displacement of Fe atoms are stronger than that in the weak ladders where the Fe-Fe bond lengths reach 2.69 ± 0.04 Å and 2.57 ± 0.03 Å respectively. Strickly speaking, there are eight kinds of the Fe-Fe distance in the leg direction, since in the $Pmn2_1$ space group the Fe-Fe rectangles are already slightly distorted to be trapezoidal. However, these trapezoidal distortion is very weak (~ 0.013 Å according to recent report^[159]), while the tetramerization distortion is in the range of 0.05-0.25 Å according to our STEM data. Due to the resolution limit of STEM, these eight kinds of the Fe-Fe distance degenerate as four kinds, by neglecting the tiny trapezoidal distortion.

To explore the origin of this unbalanced ladders, monochromated electron energy loss spectra (mono-EELS) were acquired to demonstrate the underlying charge modulation as shown in Fig. 4.7f. Using the monochromator we reach an energy resolution of 0.3 eV, which is enough to detect subtle changes in the fine structure of the EELS excitation edges. The averaged Fe- L_3 edges in strong chains and in weak chains show significant differences in

their ELNES. Comparing with Fe reference spectra^[160], the valence states of the strong and the weak chains in BaFe₂Se₃ are different, and the Fe-L₃ peak shift between them is approximately 0.4 eV (shown as the distance between two dashed line in Fig. 4.7f). Note that the EELS have an ability to reflect a valance change, but the absolute valance identification is still challenging, since the absolute energy position always has several hundred meV uncertainty. Such charge disproportion is not unusual in correlated electron systems, especially in Fe-based oxides and fluorides, e.g. Fe₃O₄ and LiFe₂F₆^[161, 162], although it has not been reported in selenides before. Nominally, the valences of Fe can become +(2+ δ) and +(2- δ) for the two sublattices, and a proper δ (around 0.15 according to our fitting results) can lead to the structural tetramerization following the idea of Peierls transition^[93]. It should be noted that the non-integer valences are possible in iron selenides, e.g. in KFe₂Se₃ and KFe₂Se₂^[154, 163]. Therefore, charge-ordering, i.e. difference of local electron density, can be the key ingredient for the unbalanced structural tetramerization and affiliated polarization, which needs deeper investigation in future.

4.4 The in-situ study on structural evolution of BaFe₂Se₃ with rising temperature

Then it is interesting to know its ferrielectric T_C . To characterize the structural tetramerization, the difference (δ) of nearest-neighbor Fe-Fe bond length (d) along the ladder direction is measured as a function of temperature (Fig. 4.10a). An in-situ heating experiment was performed using a DENSSolutions SH30 system to be able to measure over a wide temperature range. A lamella of BaFe₂Se₃ was transferred onto specialized chips using a probe-assistance method (Fig. 4.3), then the sample was heated to the set temperature by resistance heating. The displacement vector-mapping algorithm was implemented on the STEM images, and each δ is obtained by averaging around 300 measurements. The difference of Fe-Fe bond length as well as the tilting angle between the ladders at high temperature vanishes \sim 600 K, and the in-ladder tetramerization almost drops to zero, implying a high symmetric nonpolar phase (in agreement with the DSC curve shown in Fig. 4.1e and the X-ray data^[155]). The discrepancy between strong and weak ladders disappears in this high

symmetric phase, as also demonstrated by above SAED result (Fig. 4.1d). With decreasing temperature (e.g. at 473 K), unexpectedly, tetramerization emerges in one sublattice of ladders but not in the other, which is a unique characteristic of irreducible ferrielectricity, leading to an emergence of P_a (Fig. 4.10b) [calculated by density functional theory (DFT)]^[152]. Meanwhile, the ladders become tilting (Fig. 4.10c). With further decreasing temperature (e.g. at 423 K), tetramerization emerges in both ladders with different intensities and slopes, implying that the first-order transition occurring at ~ 420 K corresponds to the starting of tetramerization of the weak ladders. At ~ 373 K, the intensities of tetramerization are close to identical between both ladders, resulting in an (almost) canceled P_a , i.e. the unique compensation point (T_0) of irreducible ferrielectricity. Below T_0 , the difference between the two ladders increases with decreasing temperature, leading to a reentrance of P_a . It is worth to emphasize that the direction of polarization (i.e. the roles of strong and weak ladders) may be probably reversed across T_0 according the tendency (see the last panel of Fig. 4.1a), although our variable temperature measurements can not continuously track the evolution of individual ladder over so large temperature range. If so, the strong ladder A (weak ladder B) becomes the weak ladder A (strong ladder B) when temperature crossing T_0 . More color-enhanced HAADF-STEM images acquired at different temperatures along the c -axis are shown in Fig. 4.11.

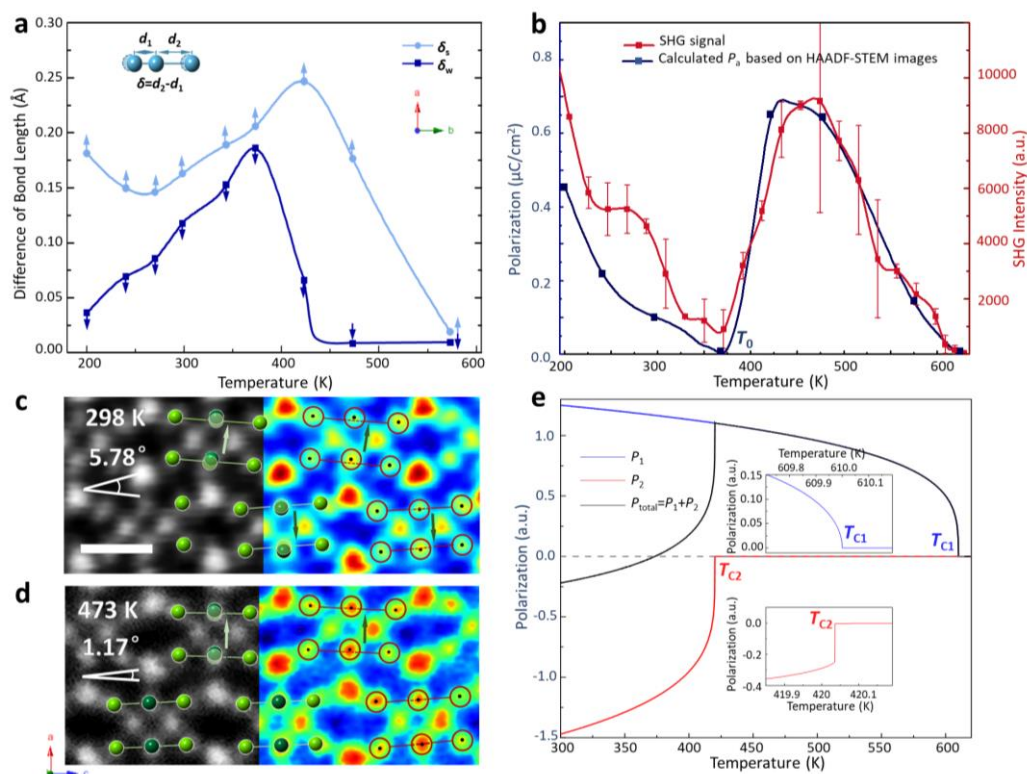


Figure 4.10 Temperature-dependent evolution of BaFe₂Se₃. a, The measured structural tetramerization. The light blue and dark blue lines correspond to the strong and weak ladders respectively. The affiliated arrows denote the corresponding dipoles. b, Left axis: the polarization along the *a*-axis (DFT calculated using the STEM structural data). Right axis: the SHG signal, which mainly reflects the evolution of P_a . The overall evolutions of the polarization and SHG signal qualitatively match. More SHG data and explanation can be found in Fig. 5.12. c and d, Color-enhanced HAADF-STEM images acquired at 298 K and 473 K along the *b*-axis. The Se atoms displacement in the strong chain is larger than that in the weak chain at 298 K; this is consistent with the difference of the Fe chain evolution magnitude at 298 K. Also, the tilt angle between ladders varies from 5.78° to 1.17° at high temperature. e, Simulated evolution of order parameters with a most simplified Landau-type free energy formula. Inserts: the magnified views near the phase transitions, which indicate a second-order transition at T_{C1} and a first-order transition at T_{C2} .

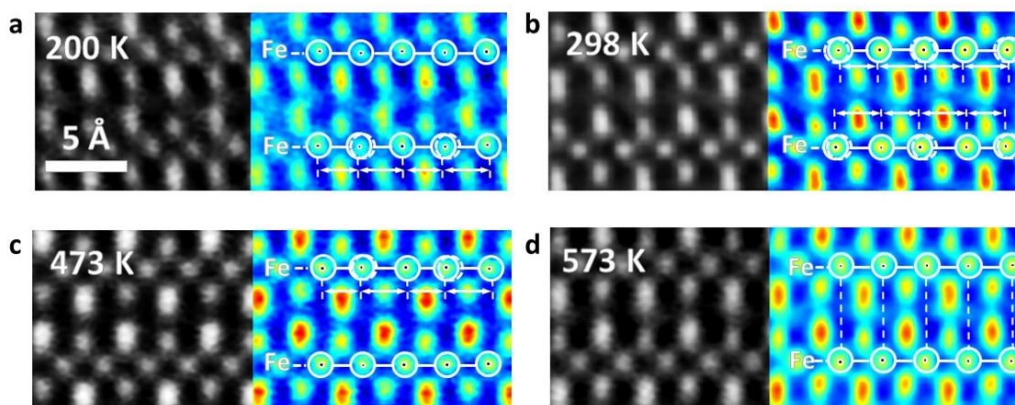


Figure 4.11 Color-enhanced HAADF-STEM images acquired at different temperatures along the c -axis. The strong ladder shows distinct tetramerization at (a) 200 K, (b) 298 K, and (c) 473 K, and the weak ladder reveals tetramerization at (b) 298 K. The difference of Fe-Fe bond length at high temperature (d) 573 K vanishes in both ladders indicating that in-ladder tetramerization almost drops to zero.

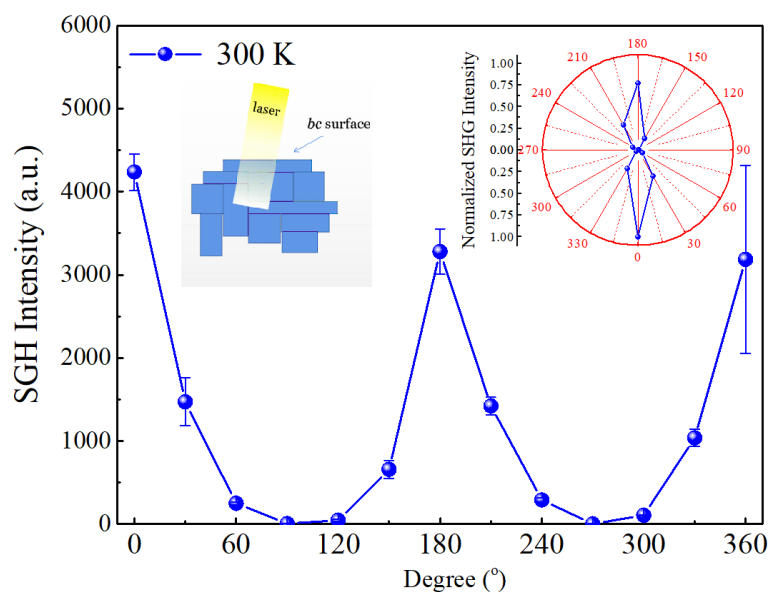


Figure 4.12 In-plane rotation of the polarization direction of the incident laser. The initial polarization (i.e. electric field component E) of the incident laser is along the c -axis. Insert (right): a polar diagram. A single axis behavior, i.e. 180° as a period, is evidenced. We repeated such rotation in several temperatures, and the 180° symmetry did not change. When $E \parallel b$, the signal is almost zero, which can exclude the surface contribution. Although our crystal only own large cleavage surface of bc plane [see Fig. 5.2], the laser of 800 nm wavelength used in SHG measurement can penetrate into the crystals partially and reflects some “inner” information beyond the surface (see Insert left). In fact, the SHG measurements

can even create small burning holes by light spots. Then the P_a contribution from inner twin crystals are very possible to be detected by SHG. Considering the much larger amplitude of P_a than P_c (in most cases $P_a \sim 10-100P_c$), a little concentration of P_a domain can dominant the SHG signal, over the P_c 's signal. Another source of P_a 's signal is the canting angle of incident laser. If the incident angle is not exactly perpendicular to the bc surface, the electric field component along the a -axis will be available.

Since the ferrielectric polarization can not be directly measured using electrical methods (and even pizeoelectric force microscopy) in the current stage due to the high leakage of the samples (considering the very small band gap $\sim 0.13-0.178$ eV^[156, 157], an optical second harmonic generation (SHG) experiment is employed to characterize the polarity of the materials (see Methods for experimental details). Our SHG signal (Fig. 4.10b) demonstrates its polarity below ~ 600 K. Most importantly, the non-monotonic evolution of the SHG signal unambiguously matches the DFT calculated polarization, including the possible compensation point at $\sim 380-400$ K, which provides a very strong evidence to support our STEM data.

The irreducible ferrielectricity of BaFe_2Se_3 can be qualitatively described by Landau theory with a coupling between two ladders (P_A & P_B). The most simplified free energy formula can be written as:

$$F = \alpha_A(T - T_A)P_A^2 + \beta_A P_A^4 + \gamma_A P_A^6 + \alpha_B(T - T_B)P_B^2 + \beta_B P_B^4 + \gamma_B P_B^6 + \alpha_{AB}P_A \cdot P_B,$$

where the first to six items are the standard Landau-Ginzburg-Devonshire type energy expression up to the sixth power for sub-lattices A and B, while the last item is the antiferroelectric coupling between two sub-lattices. All coefficients except β_2 are positive and the small canting angle between P_A and P_B is neglected. Without fine tuning of the coefficients (see Methods for details), the simulated evolution of the polarization (Fig. 4.10e) is qualitatively reproducing the non-monotonic experimental behavior, implying the correct main physics captured in the model. Consistent with the DSC data, the high temperature transition is a second-order one, while the low temperature transition is a first-order one due to the negative β_2 .

4.5 The in-situ study on structural evolution of BaFe_2Se_3 under external bias

As a polar material, electric field tuning of the polarization is a fundamental function. However a direct measurement of the electric hysteresis loop is technically challenging in the current stage due to serious leakage, but we have successfully developed an inspiring in-situ technique to manipulate the polar structure at an atomic scale by applying an electric field. An electrical bias was applied between a tungsten tip, which acts as a mobile electrode, and the lamella of BaFe_2Se_3 , which is connected to ground. To capture the changing of atoms positions, the real-time crystal structure with atomic-scale spatial resolution was characterized in STEM mode; the access to dynamic structural information provide a clear picture of the evolution under an external electric field. As shown in Fig. 4.13b-c and Fig. 4.14, the tetramerization is significantly enhanced by applying an electric field along the a -axis. This implies a significant enhancement of polarization under the electric field. However, the reversal of P_a has not been achieved, implying a large coercive field.

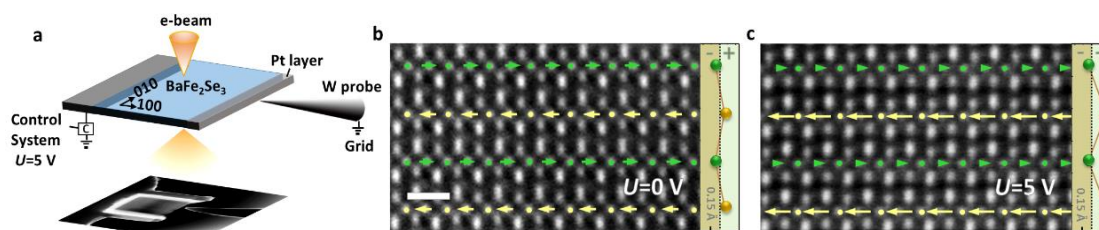


Figure 4.13 Manipulation of the ferroelectric polarization in BaFe_2Se_3 . a, Schematic diagram of the electric field experiment. The in-situ biasing experiment was performed with an input voltage $V_{\text{DC}}=5$ V. To capture the structural changes, a real-time analysis is performed in STEM mode. b and c, Comparison of the local dipoles with/without applied voltage. The arrows denote the displacements of 50% of the Fe ions, while the rest of the Fe ions are treated as reference points. The difference between the strong/weak ladders is further enhanced by the electric field. Arrows are added to make the displacements more visible.

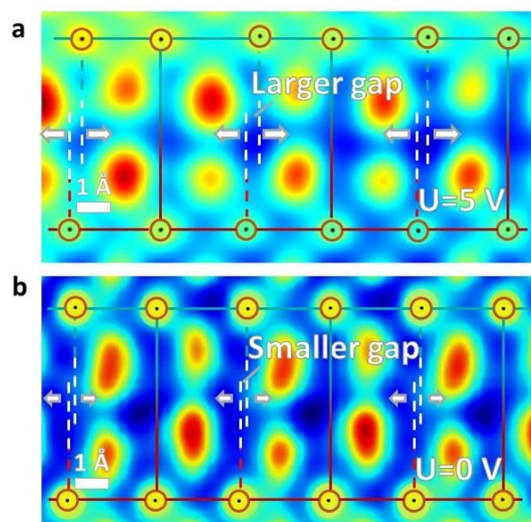


Figure 4.14 Color-enhanced HAADF-STEM images of the difference of Fe atoms displacement in the in-situ bias experiment. The neighboring Fe-Fe bond length in the weak chain under bias is equal while an enhanced tetramerization of the Fe-block is observed on the strong chain. The difference between weak and strong chain evolution is much smaller without bias. The enhanced tetramerization here indicates a corresponding enhanced polarization along the a -axis.

Previous experiments reported the space group $Pnma$ for $BaFe_2Se_3$ at room temperature^[154-156], which is nonpolar and does not allow the tetramerization. A recent work reported the space group $Pmn2_1$ (a subgroup of $Pnma$) at room temperature, allowing the tetramerization and polarization^[159]. Another recent X-ray diffraction work reported the space group $Pmn2_1$ at 300 K but Pm (a subgroup of $Pmn2_1$ allowing the inequivalent ladders) at 150 K^[164]. In fact, the patterns of NPD (or X-ray) are very subtle among these space groups, which thus can not distinguish these structures precisely. Instead, our STEM technique is more suitable to monitor these subtle distortions of inner coordinates. According to our studies, below T_{C1} the accurate space group should already be Pm , allowing the asymmetry between two ladders. The transition from $Bbmm$ to Pm at T_{C1} is a second-order one while the first-order transition at T_{C2} does not change the symmetry. Other high-resolution technique, such as synchrotron X-ray diffraction, may be helpful to verify our STEM results in future.

4.6 Conclusions

Finally, it should be noted that the irreducible ferrielectrics is not limited to BaFe_2Se_3 but with broader interests. For example, as an important branch of multiferroics, TbMn_2O_5 and other 125-type manganites showed strange “ferroelectric” behavior of polarization as a function of temperature or magnetic field^[165, 166], including the compensation point of polarization. The real mechanism is that the ferroelectric contributions in TbMn_2O_5 are from three out-of-sync sources according to the SHG measurement^[166].

Even though, our current work on BaFe_2Se_3 is not a marginal extension of TbMn_2O_5 . The polarity in TbMn_2O_5 is magnetism-driven, i.e. it is a so-called type-II multiferroic material, instead of a proper ferroelectric material. It is not rare for a magnetic system to have sequential magnetic phase transitions. In this sense, the nontrivial evolution of polarization in TbMn_2O_5 is just a secondary effect of magnetic evolution, which occurs at very low temperature (<40 K) and gives a very weak signal of polarization ($\sim <0.04 \mu\text{C}/\text{cm}^2$ and $\sim <0.15 \mu\text{C}/\text{cm}^2$)^[165, 166]. In our case, the ferrielectricity is not magnetism-driven but a primary polar property, which occurs above room-temperature (15 times of TbMn_2O_5) and with a much larger polarization (5-15 times of TbMn_2O_5). In addition, limited by its very weak polarization signal, the experimental measurements of TbMn_2O_5 can only rely on the pyroelectric method, which can lead to a net polarization but the microscopic facts of different contributions were mostly by suspecting or indirect derivation from SHG signals. Instead, our current work, powered by the advanced in-situ STEM techniques and thanks to the strong signal of BaFe_2Se_3 , the microscopic evolution of two contributions can be visualized directly, leading to a more decisive conclusion. In fact, although the nontrivial polarization of TbMn_2O_5 has been known for decades, it is more likely to be recognized as a type-II multiferroics with strange ferroelectric behavior. Our work will lead to a re-look at the irreducible ferrielectricity, including that in TbMn_2O_5 .

The irreducible ferrielectricity combines both characteristics of ferroelectricity and antiferroelectricity, making these systems having more degrees of freedom to be controlled. For example, by tuning the amplitudes of sub-lattice polarizations near the compensation

point, the macroscopic polarization can be easily switched, without the reversal process of dipole moments as required in ferroelectric cases. Moreover, complex ferroelectric+antiferroelectric domain structures may be expected in ferroelectrics, which deserve further studies.

In summary, employing spherical aberration-corrected STEM with sub-angstrom resolution, the structural evolution of BaFe_2Se_3 has been characterized in detail. Highly interesting phenomena, beyond previous experimental observations and theoretical predictions, have been detected and analyzed. First, BaFe_2Se_3 is a room temperature polar material. Second, combined with EELS analysis, the origin of its structural tetramerization is demonstrated to be driven by the local electron density, not the previously expected block-type antiferromagnetism. Third, most importantly, the evolution of the two ladders in BaFe_2Se_3 does not behave synchronously, leading to irreducible ferroelectricity. The compensation point, a unique fingerprint of irreducible ferroelectricity, is observed. The irreducible ferroelectricity reported here is conceptually different from previously reported reducible ferroelectricity which is actually equal to ferroelectricity. The irreducible ferroelectricity in BaFe_2Se_3 acts as the primary effect, leading to a stronger impact to the community to re-investigate this independent branch of polarity. More functionalities are promisingly expected in future based on irreducible ferroelectricity, e.g. the magnetic-field-tunable polarization as demonstrated in TbMn_2O_5 .

Summary

Strongly correlated electronic systems have been a hot topic in the field of condensed matter physics in recent years. The mutual coupling and interaction among some orders, such as charge, spin, orbit, have produced a series of novel physical phenomena. As an important part of this system, ferroelectric materials have attracted widespread attention due to their rich physical properties and broad application prospects. On the one hand, if the topological structure formed in ferroelectric materials can be controlled and observed in real time through applying external field regulation, it is expected to promote the application of topological structure materials. On the other hand, there are still deficiencies in the ferroelectric material family: there is a one-to-one correspondence between the charge and spin, but a true ferrielectrics has not yet been found. In this thesis, we demonstrated a self-developed in-situ electrical/thermodynamic method, employing a spherical aberration corrected scanning transmission electron microscope with sub-angstrom resolution, we combine high-angle annular dark field imaging (HAADF-STEM), electron energy loss spectroscopy (EELS) and integrated differential phase contrast imaging (iDPC), and we successfully achieved atomic-level manipulation and real-time observation of the microstructure of ferroelectric topological materials, we also found the irreducible ferrielectrics. The main research content and results of this paper are as follows:

(1) We choose the PTO/STO multilayer film as the research object, use DyScO₃ as the substrate and conduct the pulse laser deposition method to control the layer thickness of PTO to gradually increase from 1 uc to 21 uc. According to the experimental results, when the PTO layer thickness is less than 4 uc, the topological structure is a/c domain; when the thickness is 5 uc-9 uc, it is a steady-state wave domain; when the thickness is about 11 uc, it is a typical vortex domain; when the thickness is further increased to more than 15 uc, the ferroelectric polarization with the smooth rotation will gradually evolve into the ferroelectric polarization with the horizontal and vertical directions, and finally a flux closure domain formed by a 90° domain will be formed near 21 uc. GPA results shows that this domain

structure is closely related to the spatial distribution and strength of stress. We applied a voltage from 0 V to 5 V and successfully found that the typical vortex domain (0 V) was transformed into a steady-state wave domain (2 V) under an applied electric field and finally transformed into a polar down domain (5 V). The results of the electron energy loss spectra of Ti elements with various topologies show that the vortex domain core, wave domain core, and positive polarization surface of polar down are all enriched with Ti^{3+} . In the single domain region of polar down, the oxygen vacancies on the negative polarization surface and the Ti^{3+} on the positive polarization surface jointly complete the screening of the ferroelectric polarization. The analysis of lattice distortion shows that this change in electronic structure does not come from oxygen octahedral tilt or distortion, but from electron enrichment. These enriched electrons may affect the topological structure transformation under the action of an external electric field.

(2) The HAADF-STEM image at room temperature points out that there are strong and weak chains with different degrees of tetramerization inside BaFe_2Se_3 , and this leads to different displacements of Se atoms, which in turn leads to BaFe_2Se_3 becoming polar solids at room temperature. Further analysis based on the electron energy loss spectrum show that there are charge density waves between the adjacent strong and weak chains of BaFe_2Se_3 , and the valence state of the iron element presents periodic fluctuations. The real-time observations of BaFe_2Se_3 with the variable temperature at the atomic level show that the two iron chains of BaFe_2Se_3 have independent characteristic behaviors at different temperature, thus the net ferroelectric polarization is induced to continuously evolve with temperature changing. The in-situ electric field control of BaFe_2Se_3 shows that the polarization of BaFe_2Se_3 can be controlled by an external field.

There are still some scientific issues related to this thesis that are worthy of further study. For example, it has been verified by EELS that the core of vortex has a large amount of negative charge. Could it be confirmed that similar vortex cores are conductive channels by using macro-electrical tests; could BaFe_2Se_3 ferroelectric hysteresis loop be acquired at the atomic level by setting different applied voltages to measure the corresponding residual

polarization; for the PTO/STO multilayer, it contains rich topological structure with different layer thickness, can we observe and compare the behavior of different domain structures under the same stress conditions through external stress field; it is reported that there is phase transform from vortex domain into a paraelectric phase at high temperatures, could we measure the critical transition temperature and whether there is an intermediate phase. With the continuous excavation of the perovskite material system and the progress of the characterization methods, it is believed that these problems will be solved in the future, which will promote the wide application of ferroelectric materials in the field of microelectronic devices, especially in the field of next generation of memory.

Samenvatting

Sterk gecorreleerde elektronische systemen zijn de laatste jaren een hot topic op het gebied van de fysica van gecondenseerde materie. De onderlinge koppeling en interactie tussen sommige ordes, zoals lading, spin, baan, hebben een reeks nieuwe fysische verschijnselen voortgebracht. Als belangrijk onderdeel van dit systeem hebben ferro-elektrische materialen brede aandacht getrokken vanwege hun rijke fysische eigenschappen en brede toepassingsmogelijkheden. Enerzijds, als de topologische structuur gevormd in ferro-elektrische materialen kan worden gecontroleerd en geobserveerd in real time door toepassing van externe veldregulatie, wordt verwacht dat deze de toepassing van topologische structuurmaterialen bevordert. Aan de andere kant zijn er nog steeds tekortkomingen in de ferro-elektrische materiaalfamilie: er is een één-op-één overeenkomst tussen de lading en de spin, maar een echte ferro-elektrische stof is nog niet gevonden. In dit proefschrift hebben we een zelfontwikkelde in-situ elektrische / thermodynamische methode gedemonstreerd, waarbij we gebruik maken van een sferische aberratie gecorrigeerde scanning transmissie-elektronenmicroscoop met sub-ångström resolutie. We combineren ringvormige donkerveldbeeldvorming met hoge hoek verlies spectroscopie (EELS) en geïntegreerde differentiële fasecontrastbeeldvorming (iDPC), en we met succes atomaire-niveau manipulatie en real-time observatie van de microstructuur van ferro-elektrische topologische materialen bereikten, vonden we ook de onherleidbare ferri-elektrische systemen. De belangrijkste onderzoeksinhoud en resultaten van dit artikel zijn als volgt:

(1) We kiezen de PTO / STO-meerlagige film als onderzoeksobject, gebruiken DyScO₃ als het substraat en voeren de pulslaserafzettingmethode uit om de laagdikte van PTO geleidelijk te laten toenemen van 1 uc tot 21 uc. Volgens de experimentele resultaten, wanneer de PTO-laagdikte minder is dan 4 uc, is de topologische structuur een a / c-domein; wanneer de dikte 5 uc-9 uc is, is het een stabiel golfdomein; wanneer de dikte ongeveer 11 uc is, is het een typisch vortexdomein; wanneer de dikte verder wordt vergroot tot meer dan 15

uc, zal de ferro-elektrische polarisatie met de soepele rotatie geleidelijk evolueren naar de ferro-elektrische polarisatie met de horizontale en verticale richtingen, en uiteindelijk zal een fluxafsluitingsdomein gevormd door een 90° -domein worden gevormd nabij 21 uc. GPA-resultaten laten zien dat deze domeinstructuur nauw verband houdt met de ruimtelijke verdeling en sterkte van spanning. We hebben een spanning van 0 V tot 5 V toegepast en met succes ontdekt dat het typische vortex-domein (0 V) werd getransformeerd in een stationair golfdomein (2 V) onder een aangelegd elektrisch veld en uiteindelijk werd getransformeerd in een polair domein omlaag (5 V). De resultaten van de elektronen-energieverlies-spectra van Ti-elementen met verschillende topologieën laten zien dat de vortex-domeinkern, golfdomeinkern en positieve polarisatie-oppervlak van polair omlaag allemaal verrijkt zijn met Ti^{3+} . In het enkeldomeingebied van polair omlaag, voltooiën de zuurstofvacatures op het negatieve polarisatieoppervlak en de Ti^{3+} op het positieve polarisatieoppervlak samen de afscherming van de ferro-elektrische polarisatie. De analyse van roostervorming laat zien dat deze verandering in elektronische structuur niet het gevolg is van octaëdrische kanteling of vervorming van zuurstof, maar van elektronenverrijking. Deze verrijkte elektronen kunnen de topologische structuurtransformatie onder invloed van een extern elektrisch veld beïnvloeden.

(2) Het HAADF-STEM-beeld bij kamertemperatuur wijst erop dat er sterke en zwakke ketens zijn met verschillende graden van tetramerisatie binnen $BaFe_2Se_3$, en dit leidt tot verschillende verplaatsingen van Se-atomen, wat er op zijn beurt toe leidt dat $BaFe_2Se_3$ polaire vaste stoffen wordt bij kamertemperatuur. Verdere analyse op basis van het elektronen energieverlies spectrum laat zien dat er ladingsdichtheidsgolven zijn tussen de aangrenzende sterke en zwakke ketens van $BaFe_2Se_3$, en de valentie toestand van het ijzerelement vertoont periodieke fluctuaties. De real-time waarnemingen van $BaFe_2Se_3$ met de variabele temperatuur op atomair niveau tonen aan dat de twee ijzeren ketens van $BaFe_2Se_3$ onafhankelijk karakteristiek gedrag vertonen bij verschillende temperaturen, dus de netto ferro-elektrische polarisatie wordt geïnduceerd om continu te evolueren met temperatuurveranderingen. De in-situ elektrische veldcontrole van $BaFe_2Se_3$ laat zien dat de polarisatie van $BaFe_2Se_3$ kan worden gecontroleerd.

Er zijn nog enkele wetenschappelijke kwesties met betrekking tot dit proefschrift die verder onderzoek waard zijn. Het is bijvoorbeeld geverifieerd door EELS dat de kern van vortex een grote hoeveelheid negatieve lading heeft. Zou het kunnen worden bevestigd dat soortgelijke vortexkernen geleidende kanalen zijn door macro-elektrische tests te gebruiken; kan de ferro-elektrische hystereselus van BaFe_2Se_3 op atomair niveau worden verkregen door verschillende toegepaste spanningen in te stellen om de overeenkomstige restpolarisatie te meten; voor de PTO / STO multilayer, het bevat een rijke topologische structuur met verschillende laagdiktes, kunnen we het gedrag van verschillende domeinstructuren onder dezelfde spanningsomstandigheden observeren en vergelijken via extern spanningsveld; Er wordt gemeld dat er een faseovergang plaatsvindt van vortexdomein naar een para-elektrische fase bij hoge temperaturen, kunnen we de kritische overgangstemperatuur meten en of er een tussenfase is. Met de voortdurende uitgraving van het perovskiet-materiaalsysteem en de voortgang van de karakteriseringsmethoden, wordt aangenomen dat deze problemen in de toekomst zullen worden opgelost, wat de brede toepassing van ferro-elektrische materialen op het gebied van micro-elektronische apparaten zal bevorderen, vooral in het veld van de volgende generatie geheugen.

References

- [1] Salamon, M. B.; Jaime, M., The Physics of Manganites: Structure and Transport. *Review of Modern Physics* 2001, 73 (3), 583-628.
- [2] Mott; Neveill, S., Metal-insulator transitions. *Physics Today* 1978, 31 (11), 42-47.
- [3] Dagotto, E., Correlated Electrons in High Temperature Superconductors. *Review of Modern Physics* 1993, 66 (3), 763-840.
- [4] Dawber, M.; Rabe, K. M.; Scott, J. F., Physics of thin-film ferroelectric oxides. *Reviews of Modern Physics*, 2005, 77 (4): 1083-1130.
- [5] Ramesh, R.; Spaldin, N. A., Multiferroics: progress and prospects in thin films. *Nature Materials*, 2007, 6 (1): 21-29.
- [6] Cheong, S. W.; Mostovoy, M., Multiferroics: a magnetic twist for ferroelectricity. *Nature Materials* 2007, 6 (1), 13-20.
- [7] Fiebig, M., Revival of the Magnetoelectric Effect. *Cheminform* 2005, 36 (33), R123-R152.
- [8] Yu, X.; Marks, T. J.; Facchetti, A., Metal oxides for optoelectronic applications. *Nature Materials*, 2016, 15 (4): 383-396.
- [9] Fan, L.; Zhu, B.; Chen, M.; Wang, C.; Raza, R.; Qin, H.; Wang, X.; Wang, X.; Ma, Y., High performance transition metal oxide composite cathode for low temperature solid oxide fuel cells. *Journal of Power Sources*, 2012, 203 (Apr.1): 65-71.
- [10] Sawada, H.; Hosokawa, F.; Kaneyama, T.; Ishizawa, T.; Terao, M.; Kawazoe, M.; Sannomiya, T.; Tomita, T.; Kondo, Y.; Tanaka, T., Achieving 63 pm Resolution in Scanning Transmission Electron Microscope with Spherical Aberration Corrector. *Japanese Journal of Applied Physics* 2007, 46 (20-24), 568-570.
- [11] Bibes, M.; Barthélémy, A., Multiferroics: towards a magnetoelectric memory. *Nature Materials* 2008, 7 (6), 425-6.
- [12] Witzak-Krempa, W.; Chen, G.; Kim, Y. B.; Balents, L., Correlated quantum phenomena in the strong spin-orbit regime. *Annual Review of Condensed Matter Physics* 2013, 5 (1), 57-82.
- [13] Keimer, B.; Kivelson, S. A.; Norman, M. R.; Uchida, S.; Zaanen, J., From quantum matter to high-temperature superconductivity in copper oxides. *Nature* 2015, 518 (7538), 179-86.
- [14] Bibes, M.; Villegas, J. E.; Barthelemy, A., Ultrathin oxide films and interfaces for electronics and spintronics. *Advances in Physics* 2011, 60 (1), 5-84.
- [15] Schlom, D. G.; Mannhart, J., Oxide electronics: Interface takes charge over Si. *Nature Materials* 2011, 10 (3), 168-9.
- [16] Mannhart, J.; Schlom, D. G., Oxide interfaces--an opportunity for electronics. *Science* 2010, 327 (5973), 1607-1611.
- [17] Cen, C.; Thiel, S.; Mannhart, J.; Levy, J., Oxide Nanoelectronics on Demand. *Science* 2009, 323 (5917), 1026-1030.
- [18] Moore, G. E., Cramming More Components Onto Integrated Circuits. *Proceedings of the IEEE* 1998, 86 (1), 82-85.
- [19] Johansson, M.; Lemmens, P., Perovskites and thin films—crystallography and chemistry. *Journal of Physics-Condensed Matter* 2008, 20 (26), 264001.

- [20] Davies, P. K.; Wu, H.; Borisevich, A. Y.; Molodetsky, I. E.; Farber, L., Crystal Chemistry of Complex Perovskites: New Cation-Ordered Dielectric Oxides. *Annual Review of Materials Research* 2008, 38, 369-401.
- [21] Pea, M. A.; Fierro, J. L., Chemical structures and performance of perovskite oxides. *Chemical Reviews* 2001, 101 (7), 1981-2017.
- [22] Bhalla, A. S.; Guo, R.; Roy, R., The perovskite structure- a review of its role in ceramic science and technology. *Materials Research Innovations* 2000, 4 (1), 3-26.
- [23] Ohtomo, A.; Muller, D. A.; Grazul, J. L.; Hwang, H. Y., Artificial charge-modulation in atomic-scale perovskite titanate superlattices. *Nature* 2002, 419 (6905), 378-380.
- [24] Junquera, J.; Ghosez, P., Critical thickness for ferroelectricity in perovskite ultrathin films. *Nature* 2003, 422 (6931), 506-509.
- [25] Wang, J.; Neaton, J. B.; Zheng, H.; Nagarajan, V.; Ogale, S. B.; Liu, B.; Viehland, D.; Vaithyanathan, V.; Schlom, D. G.; Waghmare, U. V., Epitaxial BiFeO multiferroic thin film heterostructures. *Cheminform*, 2003, 34 (24): 1719-1722.
- [26] Smadici, S.; Abbamonte, P.; Bhattacharya, A.; Zhai, X.; Zuo, J. M., Electronic Reconstruction at SrMnO₃-LaMnO₃ Superlattice Interfaces. *Physical Review Letters*, 2007, 99 (19): 196404.
- [27] Yamada, H. O., Y.; Ishii, Y.; Sato, H.; Kawasaki, M.; Akoh, H.; Tokura, Y., Engineered Interface of Magnetic Oxides. *Science*, 2004, 305 (5684): 646-648.
- [28] Ueda, K. T., H.; Kawai, T., Ferromagnetism in LaFeO₃-LaCrO₃ Superlattices. *Science* 1998, 280 (5366), 1064-1066.
- [29] Ohtomo, A.; Hwang, H. Y., A high-mobility electron gas at the LaAlO₃/SrTiO₃ heterointerface. *Nature* 2004, 427 (6973), 423.
- [30] Benckiser, E.; Haverkort, M. W.; Brück, S.; Goering, E.; Macke, S.; Franó, A.; Yang, X.; Andersen, O. K.; Cristiani, G.; Habermeier, H. U., Orbital reflectometry of oxide heterostructures. *Nature Materials*, 2011, 10 (3): 189.
- [31] Reyren, N.; Thiel, S.; Caviglia, A. D.; Kourkoutis, L. F.; Hammerl, G.; Richter, C.; Schneider, C. W.; Kopp, T.; Ruetschi, A. S.; Jaccard, D.; Gabay, M.; Muller, D. A.; Triscone, J. M.; Mannhart, J., Superconducting Interfaces Between Insulating Oxides. *Science*, 2007, 317(5842): 1196-1199.
- [32] Erni, R.; Rossell, M. D.; Kisielowski, C.; Dahmen, U., Atomic-resolution imaging with a sub-50-pm electron probe. *Physical Review Letters* 2009, 102 (9), 096101.
- [33] Muller, D. A.; Kourkoutis, L. F.; Murfitt, M.; Song, J. H.; Hwang, H. Y.; Silcox, J.; Dellby, N.; Krivanek, O. L., Atomic-scale chemical imaging of composition and bonding by aberration-corrected microscopy. *Science*, 2008, 319 (5866): 1073-1076.
- [34] Essers, E.; Benner, G.; Mandler, T.; Meyer, S.; Hschemen, R., Energy resolution of an Omega-type monochromator and imaging properties of the MANDOLINE filter. *Ultramicroscopy* 2010, 110 (8), 971-980.
- [35] Rose, H. H., Historical aspects of aberration correction. *Journal of Electron Microscopy* 2009, 58 (3), 77.
- [36] Lazić, I.; Bosch, E. G. T.; Lazar, S.; Wirix, M.; Yücelen, E., Integrated Differential Phase Contrast (iDPC)-Direct Phase Imaging in STEM for Thin Samples. *Microscopy and Microanalysis* 2016, 22, 36-37.
- [37] Bosch, E. G. T.; Ivan, L.; Sorin, L., Integrated Differential Phase Contrast (iDPC) STEM: A New Atomic Resolution STEM Technique To Image All Elements Across the Periodic Table. *Microscopy &*

- Microanalysis 2016, 22 (S3), 306-307.
- [38] Cohen; Ronald, E., Origin of ferroelectricity in perovskite oxides. *Nature* 1992, 358 (6382), 136-138.
- [39] Gao, P.; Nelson, C. T.; Jokisaari, J. R.; Zhang, Y.; Baek, S. H.; Bark, C. W.; Wang, E.; Liu, Y.; Li, J.; Eom, C. B., Direct Observations of Retention Failure in Ferroelectric Memories. *Advanced Materials Interfaces*, 2012, 24 (8): 1106-1110.
- [40] Hoffman, J.; Pan, X.; Reiner, J. W.; Walker, F. J.; Han, J. P.; Ahn, C. H.; Ma, T. P., Ferroelectric Field Effect Transistors for Memory Applications. *Advanced Materials*, 2010, 22 (26-27): 2957-2961.
- [41] Shigeki, S.; Mitsue, T., Recent Progress of Ferroelectric-Gate Field-Effect Transistors and Applications to Nonvolatile Logic and FeNAND Flash Memory. *Materials* 2010, 3 (11), 4950-4964.
- [42] Wen, Z.; Li, C.; Wu, D.; Li, A.; Ming, N., Ferroelectric-field-effect-enhanced electroresistance in metal/ferroelectric/semiconductor tunnel junctions. *Nature Materials*, 2005, 4 (24): 246802.
- [43] Cho, Y.; Fujimoto, K.; Hiranaga, Y.; Wagatsuma, Y.; Kitamura, K., Tbit/inch² ferroelectric data storage based on scanning nonlinear dielectric microscopy. *Applied Physics Letters* 2002, 81 (23), 4401-4403.
- [44] Kalinin, S. V.; Morozovska, A. N.; Chen, L.Q.; Rodriguez, B. J, Local polarization dynamics in ferroelectric materials. *Reports on Progress in Physics*, 2010, 73(5): 56502.
- [45] J., V., Piezo-Electric and Allied Phenomena in Rochelle Salt. *Physical Review* 1920, 17 (4), 475-481.
- [46] Kornev, I.; Fu, H.; Bellaiche, L., Ultrathin Films of Ferroelectric Solid Solutions under a Residual Depolarizing Field. *Physical Review Letters* 2004, 93 (19), 196104.
- [47] Fong, D. D.; Stephenson, G. B.; Streiffer, S. K.; Eastman, J. A.; Auciello, O.; Fuoss, P. H.; Thompson, C., Ferroelectricity in ultrathin perovskite films. *Physical Review B* 2004, 72 (2), 1650.
- [48] Junquera, J.; Ghosez, P., Critical thickness for ferroelectricity in perovskite ultrathin films. *Nature* 2003, 422 (6931), 506-9.
- [49] Tybell, T.; Ahn, C. H.; Triscone, J. M., Ferroelectricity in thin perovskite films. *Applied Physics Letters* 1999, 75 (6), 856-858.
- [50] Peter, F.; Szot, K.; Waser, R.; Reichenberg, B.; Tiedke, S.; Szade, J., Piezoresponse in the light of surface adsorbates: Relevance of defined surface conditions for perovskite materials. *Applied Physics Letters* 2004, 85 (14), 2896-2898.
- [51] Kalinin, S. V.; Johnson, C. Y.; Bonnell, D. A., Domain polarity and temperature induced potential inversion on the BaTiO₃(100) surface. *Journal of Applied Physics* 2002, 91 (6), 3816-3823.
- [52] Kalinin, S. V.; Bonnell, D. A., Local potential and polarization screening on ferroelectric surfaces. *Physical Review B* 2001, 63 (12), 125411.
- [53] Damjanovic, D., Ferroelectric, dielectric and piezoelectric properties of ferroelectric thin films and ceramics. *Reports on Progress in Physics* 1999, 61 (9), 1267-1324.
- [54] Maksymovych, P.; Balke, N.; Jesse, S.; Huijben, M.; Ramesh, R.; Baddorf, A. P.; Kalinin, S. V., Defect-induced asymmetry of local hysteresis loops on BiFeO₃ surfaces. *Journal of Materials Science* 2009, 44, 5095-5101.
- [55] Canedy, C. L.; Li, H.; Alpay, S. P.; Salamanca-Riba, L.; Ramesh, R., Dielectric properties in heteroepitaxial Ba_{0.6}Sr_{0.4}TiO₃ thin films: Effect of internal stresses and dislocation-type defects. *Applied Physics Letters*, 2000, 77 (11): 1695-1697.
- [56] Balzar, D.; Ramakrishnan, P. A.; Hermann, A. M., Defect-related lattice strain and the transition temperature in ferroelectric thin films. *Physical Review B* 2004, 70 (9), 092103.
- [57] Mermin, N. D., The topological theory of defects in ordered media. *Review of Modern Physics* 1979, 51

- (3), 591.
- [58] Shinjo, T., Okuno, T., Hassdorf, R., Shigeto, K. & Ono, T. , Magnetic Vortex Core Observation in Circular Dots of Permalloy. *Science* 2000, 289, 930-932.
- [59] Nagaosa, N.; Tokura, Y., Topological properties and dynamics of magnetic skyrmions. *Nature Nanotechnology* 2013, 8 (12), 899-911.
- [60] Romming, N.; Hanneken, C.; Menzel, M.; Bickel, J. E.; Wolter, B.; Bergmann, K. V.; Kubetzka, A.; Wiesendanger, R., Writing and Deleting Single Magnetic Skyrmions. *Science* 2013, 341 (6146), 636-639.
- [61] Hertel, R.; Fruchart, O.; Cherifi, S.; Jubert, P. O.; Heun, S.; Locatelli, A.; Kirschner, J., Three-dimensional magnetic-flux-closure patterns in mesoscopic Fe islands. *Physical Review B*, 2005, 72: 214409.
- [62] Raabe, J.; Quitmann, C.; Back, C. H.; Nolting, F.; Johnson, S.; Buehler, C., Quantitative Analysis of Magnetic Excitations in Landau Flux-Closure Structures Using Synchrotron-Radiation Microscopy. *Physical Review Letters*, 2005, 94 (21): 217204.
- [63] Naumov, I. I.; Fu, H., Cooperative Response of Pb(ZrTi)O₃ Nanoparticles To Curled Electric Fields. *Physical Review Letters*, 2008, 101 (19): 280-283.
- [64] Naumov, I. I.; Bellaiche, L.; Fu, H., Unusual phase transitions in ferroelectric nanodisks and nanorods. *Cheminform* 2004, 432 (7018), 737-40.
- [65] Pilania, G.; Ramprasad, R., Complex polarization ordering in PbTiO₃ nanowires: A first-principles computational study. *Physical Review B* 2010, 82 (15), 155442.
- [66] Mangeri, J.; Espinal, Y.; Jokisaari, A.; Pamir Alpaly, S.; Nakhmanson, S.; Heinonen, O., Topological phase transformations and intrinsic size effects in ferroelectric nanoparticles. *Nanoscale*, 2017, 9(4).
- [67] Schilling, A.; Byrne, D.; Catalan, G.; Webber, K. G.; Genenko, Y. A.; Wu, G. S.; Scott, J. F.; Gregg, J. M., Domains in Ferroelectric Nanodots. *Nano Letters*, 2009, 9 (9): 3359-3364.
- [68] Rodriguez, B. J.; Gao, X. S.; Liu, L. F.; Lee, W.; Naumov, I. I.; Bratkovsky, A. M.; Hesse, D.; Alexe, M., Vortex polarization states in nanoscale ferroelectric arrays. *Nano Letters*, 2009, 9 (3): 1127.
- [69] Jia, C. L.; Urban, K. W.; Alexe, M.; Hesse, D.; Vrejoiu, I., Direct observation of continuous electric dipole rotation in flux-closure domains in ferroelectric Pb(Zr,Ti)O₃. *Science*, 2011, 331 (6023): 1420.
- [70] Tang, Y. L.; Zhu, Y. L.; Ma, X. L.; Borisevich, A. Y.; Morozovska, A. N.; Eliseev, E. A.; Wang, W. Y.; Wang, Y. J.; Xu, Y. B.; Zhang, Z. D., Observation of a periodic array of flux-closure quadrants in strained ferroelectric PbTiO₃ films. *Science*, 2015, 348 (6234): 547-551.
- [71] Liu, Y.; Zhu, Y.; Tang, Y.; Wang, Y.; Jiang, Y.; Xu, Y.; Zhang, B.; Ma, X., Local Enhancement of Polarization at PbTiO₃/BiFeO₃ Interfaces Mediated by Charge Transfer. *Nano Letters* 2017, 17 (6), 3619.
- [72] Ramesh, R., Observation of Polar Vortices in Oxide Superlattices. *Nature* 2016, 530 (S3), 198-201.
- [73] Das, S.; Tang, Y. L.; Hong, Z.; Goncalves, M. A. P.; McCarter, M. R.; Klewe, C.; Nguyen, K. X.; Gomez-Ortiz, F.; Shafer, P.; Arenholz, E.; Stoica, V. A.; Hsu, S. L.; Wang, B.; Ophus, C.; Liu, J. F.; Nelson, C. T.; Saremi, S.; Prasad, B.; Mei, A. B.; Schlom, D. G.; Iniguez, J.; Garcia-Fernandez, P.; Muller, D. A.; Chen, L. Q.; Junquera, J.; Martin, L. W.; Ramesh, R., Observation of room-temperature polar skyrmions. *Nature*, 2019, 568 (7752): 368-372.
- [74] Balke, N.; Winchester, B.; Ren, W.; Chu, Y. H.; Morozovska, A. N.; Eliseev, E. A.; Huijben, M.; Vasudevan, R. K.; Maksymovych, P.; Britson, J., Enhanced electric conductivity at ferroelectric vortex cores in BiFeO₃. *Nature Physics*, 2012, 8 (1): 81-88.

- [75] Lu, L.; Nahas, Y.; Liu, M.; Du, H.; Jiang, Z.; Ren, S.; Wang, D.; Jin, L.; Prokhorenko, S.; Jia, C. L., Topological Defects with Distinct Dipole Configurations in $\text{PbTiO}_3/\text{SrTiO}_3$ Multilayer Films. *Physical Review Letters*, 2018, 120 (17): 177601.
- [76] Hong, Z.; Chen, L.-Q., Blowing polar skyrmion bubbles in oxide superlattices. *Acta Materialia* 2018, 152, 155-161.
- [77] Hong, Z.; Damodaran, A. R.; Xue, F.; Hsu, S. L.; Britson, J.; Yadav, A. K.; Nelson, C. T.; Wang, J. J.; Scott, J. F.; Martin, L. W., Stability of Polar Vortex Lattice in Ferroelectric Superlattices. *Nano Letters*, 2017, 17 (4): 2246.
- [78] Du, K.; Zhang, M.; Dai, C.; Zhou, Z. N.; Xie, Y. W.; Ren, Z. H.; Tian, H.; Chen, L. Q.; Van Tendeloo, G.; Zhang, Z., Manipulating topological transformations of polar structures through real-time observation of the dynamic polarization evolution. *Nature Communications*, 2019, 10 (1): 4864.
- [79] Damodaran, A. R.; Clarkson, J. D.; Hong, Z.; Liu, H.; Yadav, A. K.; Nelson, C. T.; Hsu, S. L.; Mccarter, M. R.; Park, K. D.; Kravtsov, V., Phase coexistence and electric-field control of toroidal order in oxide superlattices. *Nature Materials*, 2017, 16, 1003.
- [80] Chen, P.; Zhong, X.; Zorn, J. A.; Li, M.; Sun, Y.; Abid, A. Y.; Ren, C.; Li, Y.; Li, X.; Ma, X.; Wang, J.; Liu, K.; Xu, Z.; Tan, C.; Chen, L.; Gao, P.; Bai, X., Atomic imaging of mechanically induced topological transition of ferroelectric vortices. *Nature Communications*, 2020, 11 (1): 1840.
- [81] Li, X.; Tan, C.; Liu, C.; Gao, P.; Sun, Y.; Chen, P.; Li, M.; Liao, L.; Zhu, R.; Wang, J.; Zhao, Y.; Wang, L.; Xu, Z.; Liu, K.; Zhong, X.; Wang, J.; Bai, X., Atomic-scale observations of electrical and mechanical manipulation of topological polar flux closure. *Proceedings of the National Academy of Sciences*, 2020, 117 (32): 18954.
- [82] Yuan, S.; Chen, W. J.; Liu, J.; Liu, Y.; Zheng, Y., Torsion-induced vortex switching and skyrmion-like state in ferroelectric nanodisks. *Journal of Physics: Condensed Matter* 2018, 30.
- [83] Pulvari, C. F., Ferrielectricity. *Physical Review* 1960, 120 (5), 1670-1673.
- [84] Miller, R. C.; Wood, E. A.; Remeika, J. P.; Savage, A., $\text{Na}(\text{Nb}_{1-x}\text{V}_x)\text{O}_3$ System and "Ferrielectricity". *Journal of Applied Physics*, 1962, 33 (5): 1623-1630.
- [85] Scott, J. F.; Morrison, F. D.; Slawin, A. M. Z.; Lightfoot, P.; Clulow, R.; Gherson, A. S. A.; Bumstead, A. M.; Gardner, J.; Capelli, S. C.; Probert, M. R., Ferrielectricity in the metal-organic ferroelectric tris-sarcosine calcium chloride. *Physical Review B*, 2017, 95 (9).
- [86] Maisonneuve, V.; Cajipe, V. B.; Simon, A.; Muhll, R. V. D.; Ravez, J., Ferrielectric ordering in lamellar CuInP_2S_6 . *Physical Review B* 1997, 56 (56), 10860-10868.
- [87] Liu, F.; Lu, Y.; Seyler, K. L.; Li, X.; Peng, Y.; Lin, J.; Wang, X.; Zhou, J.; Hong, W.; He, H., Room-temperature ferroelectricity in CuInP_2S_6 ultrathin flakes. *Nature Communications*, 2016, 7: 12357.
- [88] Gou, G.; Rondinelli, J. M., Piezoelectricity Across a Strain-Induced Isosymmetric Ferri-to-Ferroelectric Transition. *Advanced Materials Interfaces* 2015, 1 (5), 311-316.
- [89] Pitcher, M. J.; Mandal, P.; Dyer, M. S.; Alaria, J.; Borisov, P.; Niu, H.; Claridge, J. B.; Rosseinsky, M. J., Magnetic materials. Tilt engineering of spontaneous polarization and magnetization above 300 K in a bulk layered perovskite. *Science*, 2015, 347 (6220): 420-424.
- [90] Orlandi, F.; Righi, L.; Cabassi, R.; Delmonte, D.; Pernechele, C.; Bolzoni, F.; Mezzadri, F.; Solzi, M.; Merlini, M.; Calestani, G., Structural and Electric Evidence of Ferrielectric State in Pb_2MnWO_6 Double Perovskite System. *Cheminform*, 2015, 45 (49): 10283-90.

- [91] Dai, P.; Hu, J.; Dagotto, E., Magnetism and its microscopic origin in iron-based high-temperature superconductors. *Nature Physics*, 2012, 8: 709.
- [92] Ying, J.; Lei, H.; Petrovic, C.; Xiao, Y.; Struzhkin, V. V., Interplay of magnetism and superconductivity in the compressed Fe-ladder compound BaFe_2Se_3 . *Physical Review B*, 2017, 95 (24).
- [93] Dong, S.; Liu, J.; Dagotto, E., BaFe_2Se_3 : A high TC magnetic multiferroic with large ferrielectric polarization. *Physical Review Letters*, 2014, 113 (18):187204.
- [94] Svitlyk, V.; Chernyshov, D.; Pomjakushina, E.; Krztonmaziopa, A.; Conder, K.; Pomjakushin, V.; Dmitriev, V., Crystal structure of BaFe_2Se_3 as a function of temperature and pressure: phase transition phenomena and high-order expansion of Landau potential. *Journal of Physics Condensed Matter An Institute of Physics Journal*, 2013, 25 (31): 315403.
- [95] Columns."[Online].Available:http://en.wikipedia.org/wiki/Transmission_electron_microscopy.
- [96] Browning, N.; James, E.; Kishida, K.; Arslan, I.; Buban, J.; Zaborac, J.; Pennycook, S.; Xin, Y.; Duscher, G., Scanning transmission electron microscopy: an experimental tool for atomic scale interface science. *Reviews on Advanced Materials Science(Russia)*, 2000, 1 (1): 1-26.
- [97] Muller, D. A., Structure and bonding at the atomic scale by scanning transmission electron microscopy. *Nature Materials* 2009, 8 (4), 263-270.
- [98] Pennycook, S. J.; Jesson, D. E., High-resolution incoherent imaging of crystals. *Physical Review Letters* 1990, 64 (8), 938-941.
- [99] Urban, K. W., Studying Atomic Structures by Aberration-Corrected Transmission Electron Microscopy. *Science* 2008, 321 (5888), 506-510.
- [100] Rose, H., Elektronenoptische Aplanate. *Optik* 1971, 34, 285-311.
- [101] Haider, M.; Rose, H.; Uhlemann, S.; Schwan, E.; Urban, K., A spherical-aberration-corrected 200kV transmission electron microscope. *Ultramicroscopy* 1998, 75 (1), 53-60.
- [102] Haider, M.; Uhlemann, S.; Schwan, E.; Rose, H.; Urban, K., Electron microscopy image enhanced. *Nature* 1998, 392 (6678), 768.
- [103] Williams, D. B.; Carter, C. B., *Transmission Electron Microscopy: A Textbook for Materials Science*. 2009; Vol. 1–4.
- [104] Leapman, R. D.; Hunt, J. A., Comparison of detection limits for EELS and EDXS. *Microscopy Microanalysis Microstructures* 1991, 2 (2-3), 231-244.
- [105] Li, S.; Zhu, Y. L.; Wang, Y. J.; Tang, Y. L.; Liu, Y.; Zhang, S. R.; Ma, J. Y.; Ma, X. L., Periodic arrays of flux-closure domains in ferroelectric thin films with oxide electrodes. *Applied Physics Letters* 2017, 111 (5), 052901.
- [106] Wang, W. Y.; Zhu, Y. L.; Tang, Y. L.; Xu, Y. B.; Liu, Y.; Li, S.; Zhang, S. R.; Wang, Y. J.; Ma, X. L., Large scale arrays of four-state vortex domains in BiFeO_3 thin film. *Applied Physics Letters* 2016, 109 (20), 591.
- [107] Chen, W. J.; Zheng, Y.; Wang, B., Vortex domain structure in ferroelectric nanoplatelets and control of its transformation by mechanical load. *Sci Rep* 2012, 2 (1978), 796.
- [108] Damodaran, A. R.; Clarkson, J. D.; Hong, Z.; Liu, H.; Yadav, A. K.; Nelson, C. T.; Hsu, S. L.; McCarter, M. R.; Park, K. D.; Kravtsov, V.; Farhan, A.; Dong, Y.; Cai, Z.; Zhou, H.; Aguado-Puente, P.; García-Fernández, P.; Íñiguez, J.; Junquera, J.; Scholl, A.; Raschke, M. B.; Chen, L. Q.; Fong, D. D.; Ramesh, R.; Martin, L. W., Phase coexistence and electric-field control of toroidal order in oxide superlattices. *Nature Materials* 2017, 16, 1003.

- [109] Kézsmárki, I.; Bordács, S.; Milde, P.; Neuber, E.; Eng, L. M.; White, J. S.; Rønnow, H. M.; Dewhurst, C. D.; Mochizuki, M.; Yanai, K., Neel-type skyrmion lattice with confined orientation in the polar magnetic semiconductor GaV_4S_8 . *Nature Materials* 2015, 14 (11).
- [110] Mühlbauer, S.; Binz, B.; Jonietz, F.; Pfleiderer, C.; Rosch, A.; Neubauer, A.; Georgii, R.; Böni, P., Skyrmion lattice in a chiral magnet. *Science* 2009, 323 (5916), 915-919.
- [111] Yu, X. Z.; Onose, Y.; Kanazawa, N.; Park, J. H.; Han, J. H.; Matsui, Y.; Nagaosa, N.; Tokura, Y., Real-space observation of a two-dimensional skyrmion crystal. *Nature* 2010, 465 (7300), 901-904.
- [112] Pan, X.; Gao, P.; Nelson, C.; Jokisaari, J.; Baek, S. H.; Bark, C. W.; Eom, C. B.; Schlom, D., Domain dynamics during ferroelectric switching. *Science* 2011, 334 (6058), 968-71.
- [113] Gao, P.; Nelson, C. T.; Jokisaari, J. R.; Baek, S. H.; Bark, C. W.; Zhang, Y.; Wang, E.; Schlom, D. G.; Eom, C. B.; Pan, X., Revealing the role of defects in ferroelectric switching with atomic resolution. *Nature Communications* 2011, 2 (6), 591.
- [114] Kleibeuker, J. E.; Koster, G.; Siemons, W.; Dubbink, D.; Kuiper, B.; Blok, J. L.; Yang, C. H.; Ravichandran, J.; Ramesh, R.; Ten Elshof, J. E., Atomically Defined Rare-Earth Scandate Crystal Surfaces. *Advanced Functional Materials* 2010, 20 (20), 3490-3496.
- [115] Chen, L. Q., Phase field Method of Phase Transitions/Domain Structures in Ferroelectric Thin Films: A Review. *Journal of the American Ceramic Society* 2008, 91 (6), 1835-1844.
- [116] Xue, F.; Wang, J. J.; Sheng, G.; Huang, E.; Cao, Y.; Huang, H. H.; Munroe, P.; Mahjoub, R.; Li, Y. L.; Nagarajan, V., Phase field simulations of ferroelectrics domain structures in $\text{PbZr}_x\text{Ti}_{1-x}\text{O}_3$ bilayers. *Acta Materialia* 2013, 61 (8), 2909-2918.
- [117] Wang, J. J.; Ma, X. Q.; Li, Q.; Britson, J.; Chen, L. Q., Phase transitions and domain structures of ferroelectric nanoparticles: Phase field model incorporating strong elastic and dielectric inhomogeneity. *Acta Materialia* 2013, 61 (20), 7591-7603.
- [118] Li, Y. L.; Hu, S. Y.; Liu, Z. K.; Chen, L. Q., Effect of Electrical Boundary Conditions on Ferroelectric Domain Structures in Thin Films. *Applied Physics Letters* 2002, 81 (3), 427-429.
- [119] Li, Y. L.; Hu, S., Y.; Liu Z., K.; Chen, L., Q., Effect of substrate constraint on the stability and evolution of ferroelectric domain structures in thin films. *Acta Materialia* 2002, 50 (2), 395-411.
- [120] Chen, L. Q.; Shen, J., Applications of semi-implicit Fourier-spectral method to phase field equations. *Computer Physics Communications* 1998, 108 (2-3), 147-158.
- [121] Uecker, R.; Velickov, B.; Klimm, D.; Bertram, R.; Bernhagen, M.; Rabe, M.; Albrecht, M.; Fornari, R.; Schlom, D. G., Properties of rare-earth scandate single crystals (Re=NdDy). *Journal of Crystal Growth* 2008, 310 (10), 2649-2658.
- [122] Haun, M. J.; Furman, E.; Jang, S. J.; Mckinstry, H. A.; Cross, L. E., Thermodynamic theory of PbTiO_3 . *Journal of Applied Physics* 1987, 62 (8), 3331-3338.
- [123] Chen, Z. H.; Damodaran, A. R.; Xu, R.; Lee, S.; Martin, L. W., Effect of symmetry mismatch on the domain structure of rhombohedral BiFeO_3 thin films. *Applied Physics Letters* 2014, 104 (18), 051606.
- [124] Zhang, Q.; Jin, C. H.; Xu, H. T.; Zhang, L. Y.; Ren, X. B.; Ouyang, Y.; Wang, X. J.; Yue, X. J.; Lin, F., Multiple-ellipse fitting method to precisely measure the positions of atomic columns in a transmission electron microscope image. *Micron* 2018, 113, 99-104.
- [125] Zhang, Q.; Zhang, L. Y.; Jin, C. H.; Wang, Y. M.; Lin, F., CalAtom: A software for quantitatively analysing atomic columns in a transmission electron microscope image. *Ultramicroscopy* 2019, 202, 114-120.

- [126] Kim, K.-E.; Jeong, S.; Chu, K.; Lee, J. H.; Kim, G.-Y.; Xue, F.; Koo, T. Y.; Chen, L.-Q.; Choi, S.-Y.; Ramesh, R.; Yang, C.-H., Configurable topological textures in strain graded ferroelectric nanoplates. *Nature Communications* 2018, 9 (1), 403.
- [127] Li, Y.; Jin, Y.; Lu, X.; Yang, J.-C.; Chu, Y.-H.; Huang, F.; Zhu, J.; Cheong, S.-W., Rewritable ferroelectric vortex pairs in BiFeO₃. *npj Quantum Materials* 2017, 2 (1), 43.
- [128] Gauquelin, N.; Bos, K. H. W. V. D.; B  ch  , A.; Krause, F. F.; Lobato, I.; Lazar, S.; Rosenauer, A.; Aert, S. V.; Verbeeck, J., Determining oxygen relaxations at an interface: A comparative study between transmission electron microscopy techniques. *Ultramicroscopy* 2017, 181, 178.
- [129] Liu, Y.; Wang, Y.; Zhu, Y.; Lei, C.; Tang, Y.; Li, S.; Zhang, S.; Li, J. Y.; Ma, X., Large Scale 2D Flux-Closure Domain Arrays in Oxide Multilayers and Their Controlled Growth. *Nano Letters* 2017, 17.
- [130] Kim, Y. M.; Morozovska, A.; Eliseev, E.; Oxley, M. P.; Mishra, R.; Selbach, S. M.; Grande, T.; Pantelides, S. T.; Kalinin, S. V.; Borisevich, A. Y., Direct observation of ferroelectric field effect and vacancy-controlled screening at the BiFeO₃/La_xSr_{1-x}MnO₃ interface. *Nature Materials* 2014, 13 (11), 1019.
- [131] Ren, Z.; Zhao, R.; Chen, X.; Li, M.; Li, X.; Tian, H.; Zhang, Z.; Han, G., Mesopores induced zero thermal expansion in single-crystal ferroelectrics. *Nature Communications* 2018, 9 (1).
- [132] Rojac, T.; Bencan, A.; Drazic, G.; Sakamoto, N.; Ursic, H.; Jancar, B.; Tavcar, G.; Makarovic, M.; Walker, J.; Malic, B., Domain-wall conduction in ferroelectric BiFeO₃ controlled by accumulation of charged defects. *Nature Materials* 2017, 16, 322-327.
- [133] Verbeeck, J.; Van, A. S., Model based quantification of EELS spectra. *Ultramicroscopy* 2004, 101 (2-4), 207-224.
- [134] Eberg, E.; Van Helvoort, A. T. J.; Takahashi, R.; Gass, M.; Mendis, B.; Bleloch, A.; Holmestad, R.; Tybell, T., Electron energy loss spectroscopy investigation of Pb and Ti hybridization with O at the PbTiO₃/SrTiO₃ interface. *Journal of Applied Physics* 2011, 109 (3), 119.
- [135] Zubko, P.; Jecklin, N.; Torrespardo, A.; Aguadopuente, P.; Gloter, A.; Lichtensteiger, C.; Junquera, J.; St  phan, O.; Triscone, J. M., Electrostatic Coupling and Local Structural Distortions at Interfaces in Ferroelectric/Paraelectric Superlattices. *Nano Letters* 2012, 12 (6), 2846-2851.
- [136] Torrespardo, A.; Gloter, A.; Zubko, P.; Jecklin, N.; Lichtensteiger, C.; Colliex, C.; Triscone, J. M.; Stephan, O., Spectroscopic mapping of local structural distortions in ferroelectric PbTiO₃/SrTiO₃ superlattices at the unit-cell scale. *Physical Review B* 2011, 84 (22).
- [137] Jang, H. W.; Felker, D. A.; Bark, C. W.; Wang, Y.; Niranjana, M. K.; Nelson, C. T.; Zhang, Y.; Su, D.; Folkman, C. M.; Baek, S. H., Metallic and insulating oxide interfaces controlled by electronic correlations. *Science* 2011, 331 (6019), 886-889.
- [138] Egoavil, R.; Tan, H.; Verbeeck, J.; Bals, S.; Smith, B.; Kuiper, B.; Rijnders, G.; Koster, G.; Tendeloo, G. V., Atomic scale investigation of a PbTiO₃/SrRuO₃/DyScO₃ heterostructure. *Applied Physics Letters* 2013, 102 (22), 223106-223106-5.
- [139] Sefat, A. S.; Amow, G.; Wu, M. Y.; Botton, G. A.; Greedan, J. E., High-resolution EELS study of the vacancy-doped metal/insulator system, Nd_{1-x}TiO₃, x=0 to 0.33. *Journal of Solid State Chemistry* 2005, 178 (4), 1008-1016.
- [140] Fu, L. F.; Welz, S. J.; Browning, N. D.; Kurasawa, M.; McIntyre, P. C., Z-contrast and electron energy loss spectroscopy study of passive layer formation at ferroelectric PbTiO₃/Pt interfaces. *Applied Physics Letters* 2005, 87 (26), 119.

-
- [141] Ryu, J.; Han, G.; Song, T. K.; Welsh, A.; Trolier-Mckinstry, S.; Choi, H.; Lee, J. P.; Kim, J. W.; Yoon, W. H.; Choi, J. J., Upshift of phase transition temperature in nanostructured PbTiO_3 thick film for high temperature applications. *ACS Applied Materials & Interfaces* 2014, 6 (15), 11980.
- [142] Ivanchik; I., I., Spontaneous polarization screening in a single domain ferroelectric. *Ferroelectrics* 1993, 145 (1), 149-161.
- [143] Wang, R. V.; Fong, D. D.; Jiang, F.; Highland, M. J.; Fuoss, P. H.; Carol, T.; Kolpak, A. M.; Eastman, J. A.; Streiffer, S. K.; Rappe, A. M., Reversible chemical switching of a ferroelectric film. *Physical Review Letters*, 2009, 102 (4): 047601.
- [144] Ren, Z.; Zhao, R.; Chen, X.; Li, M.; Li, X.; Tian, H.; Zhang, Z.; Han, G., Mesopores induced zero thermal expansion in single-crystal ferroelectrics. *Nature Communications*, 2018, 9 (1): 1638.
- [145] Baudry, L.; Sené, A.; Luk'Yanchuk, I. A.; Lahoche, L.; Scott, J. F., Polarization vortex domains induced by switching electric field in ferroelectric films with circular electrodes. *Physical Review B* 2014, 90 (2).
- [146] Padgett, M.; Bowman, R., Tweezers with a twist. *Nature Photonics* 2011, 5 (6), 343-348.
- [147] Paterson, L.; Macdonald, M.; Arlt, J.; Sibbett, W.; Bryant, P.; Dholakia, K., Controlled Rotation of Optically Trapped Microscopic Particles. *Science (New York, N.Y.)* 2001, 292, 912-4.
- [148] Pitcher, M. J.; Mandal, P.; Dyer, M. S.; Alaria, J.; Borisov, P.; Niu, H.; Claridge, J. B.; Rosseinsky, M. J., Magnetic materials. Tilt engineering of spontaneous polarization and magnetization above 300 K in a bulk layered perovskite. *Science*, 2015, 347 (6220): 420-424.
- [149] Spaldin, N. A.; Fiebig, M.; Mostovoy, M., The toroidal moment in condensed-matter physics and its relation to the magnetoelectric effect. *Journal of Physics Condensed Matter* 2008, 20 (43), 2709-2713.
- [150] Oh, Y. S.; Luo, X.; Huang, F. T.; Wang, Y.; Cheong, S. W., Experimental demonstration of hybrid improper ferroelectricity and the presence of abundant charged walls in $(\text{Ca,Sr})_3\text{Ti}_2\text{O}_7$ crystals. *Nature Materials* 2015, 14 (4), 407-413.
- [151] Kresse, G.; Furthmüller, J., Efficient iterative schemes for ab initio total-energy calculations using a plane-wave basis set. *Phys Review B* 1996, 54 (16), 11169-11186.
- [152] King-Smith, R. D.; Vanderbilt, D., Theory of polarization of crystalline solids. *Physical Review B* 1993, 47 (3), 1651-1654.
- [153] Zhang, Y.; Lin, L. F.; Zhang, J. J.; Dagotto, E.; Dong, S., Sequential structural and antiferromagnetic transitions in BaFe_2Se_3 under pressure. *Physical Review B* 2018, 97 (4).
- [154] Caron, J. M.; Neilson, J. R.; Miller, D. C.; Llobet, A.; Mcqueen, T. M., Iron displacements and magnetoelastic coupling in the antiferromagnetic spin-ladder compound BaFe_2Se_3 . *Physical Review B* 2012, 84 (18), 5109-5112.
- [155] Svitlyk, V.; Chernyshov, D.; Pomjakushina, E.; Krztonmaziopa, A.; Conder, K.; Pomjakushin, V.; Dmitriev, V., Crystal structure of BaFe_2Se_3 as a function of temperature and pressure: phase transition phenomena and high-order expansion of Landau potential. *Journal of Physics Condensed Matter An Institute of Physics Journal* 2013, 25 (31), 315403.
- [156] Nambu, Y.; Ohgushi, K.; Suzuki, S.; Du, F.; Avdeev, M.; Uwatoko, Y.; Munakata, K.; Fukazawa, H.; Chi, S.; Ueda, Y., Block magnetism coupled with local distortion in the iron-based spin-ladder compound BaFe_2Se_3 . *Physics* 2012, 85 (6), 872-878.
- [157] Lei, H.; Ryu, H.; Frenkel, A.; Petrovic, C., Anisotropy in BaFe_2Se_3 single crystals with double chains of FeSe tetrahedra. *Physical Review B* 2011, 84 (21), 214511.
- [158] Krzton-Maziopa, A.; Pomjakushina, E.; Pomjakushin, V.; Sheptyakov, D.; Chernyshov, D.; Svitlyk, V.;

- Conder, K., The synthesis, and crystal and magnetic structure of the iron selenide BaFe₂Se₃ with possible superconductivity at T_c = 11 K. *Journal of Physics Condensed Matter* 2011, 23 (40), 402201.
- [159] Aoyama, T.; Imaizumi, S.; Togashi, T.; Sato, Y.; Hashizume, K.; Nambu, Y.; Hirata, Y.; Matsubara, M.; Ohgushi, K., Polar State induced by Block-type Lattice Distortions in BaFe₂Se₃ with Quasi-One-Dimensional Ladder Structure. *Physical Review*, 2019, 99 (24): 241109.1-241109.5.
- [160] Tian, H.; Verbeeck, J.; Paul, M.; Kufer, D.; Sing, M.; Claessen, R.; Tendeloo, G. V., Interface-induced modulation of charge and polarization in thin film Fe₍₃₎O₍₄₎. *Advanced Materials* 2014, 26 (3), 461.
- [161] Coey, M., Condensed-matter physics: charge-ordering in oxides. *Nature* 2004, 430 (6996), 155.
- [162] Lin, L.-F.; Xu, Q.-R.; Zhang, Y.; Zhang, J.; Liang, Y.-P.; Dong, S., Ferroelectric Ferrimagnetic LiFe₂F₆: Charge Ordering Mediated Magnetoelectricity. *Physical Review Materials* 2017, 1, 071401(R).
- [163] Zhang, Y.; Zhang, H.; Weng, Y.; Lin, L.; Yao, X.; Dong, S., Block antiferromagnetism and possible ferroelectricity in KFe₂Se₂. *physica status solidi (RRL)* 2016, 10 (10), 757-761.
- [164] Zheng, W.; Balédent, V.; Lepetit, M. B.; Retailleau, P.; Foury-Leylekian, P., Room temperature polar structure and multiferroicity in BaFe₂Se₃. *Physical Review B* 2020.
- [165] Hur, N.; Park, S.; Sharma, P. A.; Ahn, J. S.; Guha, S.; Cheong, S. W., Electric polarization reversal and memory in a multiferroic material induced by magnetic fields. *Nature* 2004, 429 (6990), 392.
- [166] Leo, N.; Meier, D.; Pisarev, R. V.; Lee, N.; Cheong, S. W.; Fiebig, M., Independent ferroelectric contributions and rare-earth-induced polarization reversal in multiferroic TbMn₂O₅. *Physical Review B* 2012, 85 (9), 1092-1097.

List of publications

First Author/Co-first Author :

- [1] **K. Du***, M. Zhang*, C. Dai*, Z.N. Zhou, Y.W. Xie, Z.H. Ren, H. Tian, L.Q. Chen, G. Van Tendeloo & Z. Zhang. Manipulating topological transformations of polar structures through real-time observation of the dynamic polarization evolution. *Nature Communications* 10, 4864 (2019)
- [2] **K. Du***, L. Guo*, J. Peng*, X. Chen, Z.N. Zhou, Y. Zhang, T. Zheng, Y.P. Liang, J.P. Lu, Z. H. Ni, S.S. Wang, G. Van Tendeloo, Z. Zhang, S. Dong & H. Tian. Direct Visualization of Irreducible Ferrielectricity in Crystals. *npj Quantum Materials* 5, 49 (2020)
- [3] **K. Du***, P. R. Tong*, T. Altantzis, I. Lobato, Y.T. Sun, M. Zhang, Y. W. Xie, S. Bals, H. Tian, G. Van Tendeloo, R. Ramesh, Z. Zhang. Revealing the Chirality of Polar Vortices in Real-space Direct Visualization of Irreducible Ferrielectricity in Crystals. *Prepared* (2021)
- [4] M. Zhang*, **K. Du***, T.S. Ren, H. Tian, Z. Zhang, H. Y. Hwang & Y.W. Xie. A termination-insensitive and robust electron gas at the heterointerface of two complex oxides. *Nature Communications* 10, 4026 (2019)
- [5] Yang Liu*, Jieyuan Cui*, **K. Du*** et al. Efficient blue light-emitting diodes based on quantum-confined bromide perovskite nanostructures. *Nature Photonics* 13, 760-764 (2019)

Co-Author :

- [6] H. Li, **K. Du**, C.S. Xiang, P.F. An, X.X. Shu, Y.R. Dang, C.S. Wu, J. Wang, W. Du, J.t. Zhang, S.G. Li, H. Tian, S.Y. Wang & H.B. Xia. Controlled chelation between tannic acid and Fe precursors to obtain N, S co-doped carbon with high density Fe-single

atom-nanoclusters for highly efficient oxygen reduction reaction in Zn–air batteries. *J. Mater. Chem. A*, 8,17136 (2020)

[7] J.X. Jiao, **K. Du**, Y.T. Wang, P.P. Sun, H.H. Zhao, P.J. Tang, Q. Fan, H. Tian, Q. Li, Q.Y. Xua. N plasma treatment on graphene oxide-MoS₂ composites for improved performance in lithium ion batteries. *Mater. Chem. Phys.*, 240, 122169 (2020)

[8] J. Meng, X.Q. Fu, **K. Du**, X. Chen, Q.Y. Lin, X. Wei, J.X. Li & Z. Zhang. BaZrO₃ hollow nanostructure with Fe (III) doping for photocatalytic hydrogen evolution under visible light. *Int. J. Hydrogen Energy*, 43, 9224-9232 (2018)

[9] J.J. Si*, Y. Liu*, Z.F. He, H. Du, **K. Du**, D. Chen, J. Li, M.M. Xu, H.Tian, H.P. He, D.W. Di, C.Q. Lin, Y.C. Cheng, J.P. Wang & Y.Z. Jin. Efficient and High-Color-Purity Light-Emitting Diodes Based on In Situ Grown Films of CsPbX₃ (X = Br, I) Nanoplates with Controlled Thicknesses. *Acs Nano*, 11, 11100-11107 (2017)

[10] Y. Cao, N.N. Wang, H. Tian, J.S. Guo, Y.Q. Wei, H. Chen, Y.Y. Miao, W. Zou, K. Pan, Y.R. He, H. Cao, Y. Ke, M.M. Xu, Y. Wang, M. Yang, **K. Du**, Z.W. Fu, D.C. Kong, D.X. Dai, Y.Z. Jin, G.Q. Li, H. Li, Q.M. Peng, J.P. Wang & W. Huang. Perovskite light-emitting diodes based on spontaneously formed submicrometre-scale Structures. *Nature*, 7726, 249-253 (2018)

Acknowledgements

As the last part of my thesis, I would like to say thanks to all the people that helped me and encouraged me over my PhD study.

First and foremost, I would like to give my sincere gratitude to my promoter, Prof. Dr. Gustaaf Van Tendeloo, Prof. Dr. He Tian and Prof. Dr Sara Bals, for their untiring guidance, sensible advices and kind encouragement and patience throughout the PhD study. Without their guide and support I could not accomplish my thesis. It is my best fortune to have them as my PhD promoter.

I would like to give my great thanks to Prof. Dr. Altantzis Thomas, for helping me solving many practical problems on Tomo, providing good ideas for my scientific research.

I am grateful to all EMATers that your help and discussions helped me reach a better understanding of microscopy and you made my PhD life more colourful: Shanshan, Yang, Lipeng, Pei, Chen, Da, Qiongyang, Zezhong, Nicolass, Ivan, Sowmya, Thais, Annick, Marnik, Lydia, Miek, Stijn, Koen, Ece.

I would like to acknowledge the help of ZJUers, my scientific study was started there and the major part of my PhD study was accomplished there: Prof. Dr. Jixue Li, Prof. Dr. Chuanhong Jin, Prof. Dr. Yong Wang, Prof. Dr. Qian Yu, Prof. Dr. Jiangwei Wang, Prof. Dr. Xiao Wei. My special thanks given to all of these professors for providing me all the materials and holders I used and for all the discussions we had for the study, the article and the thesis. Thanks to Dr. Zhenju Shen, Dr. Ronguang Zeng, Dr. Tulai Sun, Dr. Xing Chen, Qi Zhu, Shiyuan Chen, Ke Fang, Zijiao Zhang, Jie Meng, Peiran Tong and all others for accompanying with me during my staying in ZJU.

Finally, with all my heart I give my greatest thanks to my beloved parents. Without their firm support and encouragement I could never finish my PhD study. They deserve my deepest and most admirable thanks and I hope from this thesis they can share the happiness and achievement with me.